UNIVERSITÀ DEGLI STUDI DI PARMA

Dottorato di ricerca in Scienze Chimiche

Ciclo XXVIII (2013-2015)

Stabilization of APIs and nutraceuticals through cocrystallization and molecular confinement

Coordinatore:

Chiar.mo Prof. Roberto Cammi

Tutor:

Chiar.ma Prof.ssa Alessia Bacchi

Dottorando: Davide Capucci

2016

CONTENTS

PREFACE

Liquid compounds tend to be essentially less stable than solid forms, therefore many drugs are formulated as solid dosage. Most pharmaceutical active ingredients (APIs) and nutraceutical compounds are manufactured and distributed as crystalline materials and their action involves the delivery of the active molecule by a solubilization process either in the body or on the environment. Poor solubility of APIs, for instance, is a common problem in their formulation since this phenomenon limits the bioavailability of the ingredient. Despite this, some important molecules for human health occur as liquid at room temperature.

Cocrystallization of the molecule of interest could be a smart and dainty way to tune solubility properties of solid phases leaving the molecule chemically unchanged, hence it is widely investigated by companies and by solid state scientists. Despite of this extremely high interest towards cocrystallization no particular emphasis has been paid to using it as a means to stabilize liquid molecules. In this work we define a benchmark of relevant molecules for human health that have been combined with suitable partners according to crystal engineering methods in order to obtain cocrystals. Solubility properties in different solvents of cocrystals new solid phases have been tested and compared to the properties of the drugs.

A further approach to deal with volatile compounds is molecular confinement inside molecular scaffold. Nowadays metal organic frameworks (MOFs) are studied in many fields ranging from catalysis to trapping or storage of gases, such as hydrogen, methane, CO_2 thanks to their extremely high porosity. Our goal is to confine liquid guests of biological relevance inside MOF pores, monitoring via X-ray diffraction, spectroscopy and thermal analysis the stabilization of the molecule of interest inside the cavities.

1. INTRODUCTION

1.1 A matter of nomenclature

It is often the case in scientific community to accept and adopt a new term and not few times ambiguity or elusiveness may confuse and mislead. As G. R. Desiraju reports: "problems with nomenclature are necessary evils in the development of a new subject" and, indeed, names and labels could easily change into whims. Protagonist of such a controversial debate is the term cocrystal (or co-crystal) which represents one of the most widespread word in the field of crystal engineering. It is important to refer to Kitaigorodsky's book *Mixed Crystals* as one of the early serious attempt to identify and clarify crystals composed of different molecules[1]. Many definitions have been reported nowadays: some refers to cocrystals as structures made up of components that are themselves crystalline solids at room temperature[2], others prefer the term "molecular complex"[3]or "multi-component molecular crystal" [4].

1.2 Cocrystals and the supramolecular synthon

We agree that is convenient to adopt the term cocrystal as a proper definition of a crystalline complex of two or more neutral molecules bound together through non covalent interaction. A schematic and simple way to treat supramolecular complexes lays on the definition of supramolecular synthons which, according with G. R. Desiraju *et al.*[5], are "the smallest structural units within which is encoded all the information inherent in the mutual recognition of molecules". Such a striking definition essentially identifies supramolecular synthons as basic bricks that play a key role in designing crystal architectures. Usually synthons involve strongly directional interactions such as hydrogen bonds[6], halogen bonds[78]. A minor but in any case relevant role is played by aromatic π-π interactions such as sandwich, edge-to-face, T-shaped, parallel-displaced stackings [9], and by van der Waals forces which concur in stabilizing the whole crystal structure.

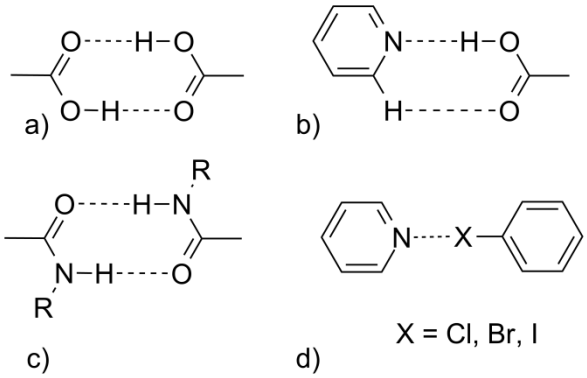

Fig. 1 Examples of supramolecular synthons: a) homosynthon between carboxylic acid groups, b) heterosynthon pyridinic ring – carboxylic acid, c) homosynthon between amidic groups, d) halogen bonding heterosynthon.

M. C. Etter showed in her works[10]a rational approach to consider hydrogen bonds and presented empirical rules necessary for the determination of preferred modes of hydrogen bonding. In recent works Zaworotko *et al.*[1112]have underlined the hierarchy of hydrogen bonds to the pyridine moiety thanks to CSD analyses and cocrystallization experiments. All of these efforts pursue a reasonable and consistent way to face the complexity of interactions among molecules in crystal forms.

1.3 Halogen bond as a powerful tool

Halogen bond is an electrostatically-driven interaction between a halogen X in a molecule R-X and a negative site B (e.g. a Lewis base lone pair or π-electrons of an unsaturated system).The concept of halogen bonding may seem to be contradictory because covalently bonded halogen atoms are typically viewed as being negative in character but it is extremely important to keep in mind that the concept of atoms in a molecule commonly treated as being entirely positive or negative is deceptive and sometimes cious[13].Halogen bond is highly directional and shows specific tendencies in close packed structure depending on whether the interacting species is an electrophile or a nucleophile. Interactions with nucleophiles have been observed to follow a precise geometry with a angles between 90° and 120° respect to the R-X bond axis while interactions with nucleophiles tend to align

along the same axis of the R-X bond (180°). It is therefore possible to study the electrostatic potential V(*r*) that the nuclei and electrons of a molecule create at any point *r* in the surrounding space. This is a real property of a system and can be evaluated by diffraction techniques [14] and computational methods and has proved out to be effective in analyzing and predicting non covalent interactions[15]. In 1992, while examining the computed V(*r*) of some alkyl halides, Brinck et al. made a surprising discovery[16]: in H_3C-Br, CBr_4 and CCl_4 , the halogen atoms have areas of positive electrostatic potential on the outer portions of their surfaces. Each such area includes a V_{max} , centered on the extension of the C-X bond. The lateral sides of these halogens have negative V(*r*), as expected. In H_3C-F, H_3C-Cl and CF_4, on the other hand, the halogen surfaces are entirely negative. These observations explain why covalently-bonded halogen atoms may interact with both nucleophiles and electrophiles. It has been observed empirically that three principal factors concur in modulating the magnitude of superficial V(*r*) and maximum and minimum values of the electrostatic potential: the polarizability of the halogen atom, its electronegativity, the electron-withdrawing power of the remainder R of the R-X molecule. For this reason, superficial $V(r)_{max}$ follows a precise order: F < Cl < Br < I.

A parallelism between hydrogen bonding and halogen bonding has been noted and discussed in detail by Legon[17]. If we consider a system such as R-Br interacting with a nucleophile B-R', it is easily noticeable that R-Br is characterized by a positive region similar to the one of the proton in a hydrogen bonded donor system. What effectively does differ is that the positive region of the bromine is narrowly focused along the extension of the R-Br bond resulting in a strongly directional R-Br ··· B-R' interaction while hydrogen positive region is nearly hemispherical.

The nature of the halogen bond is strictly connected to the atomic orbitals of the system and has been reported by Shields *et al.*[18].If we consider a free halogen atom X, each valence p orbital contains 5/3 electrons. When X interacts along a specific direction (let's say along the *z*-axis) to form a covalent bond in a molecule R-X, it assumes a valence state electronic configuration approximating $s^2p_x^2p_y^2p_z^1$. In this case V(*r*) is still positive at all radial distances along the *z*-axis corresponding to the half-filled p_z orbital but along *x*-axis and *y*-axis it is positive only nearby the nucleus and negative as radial distance increases, reflecting the full-occupied p_x and p_y orbitals. This partic-

ular behavior generates a sort of ring of electrostatic potential that surrounds the halogen atom with a hole, where electrostatic potential is positive, along the *z*-axis, which is called σ-hole. The potential of halogen bonding has recently received particular attention in the field of crystal engineering[19] and, in particular, in the process of drug design through cocrystallization.

1.4 Cocrystals vs salts

In the case of cocrystals based on hydrogen: if proton transfer has occurred, a crystalline acid-base complex can be considered a salt while it is a cocrystal in case the proton remains on the acid. Reaction of an acid with a base will be expected to form a salt if the difference of pK_a between the two species is greater than 2 or 3 [20]. Values of ΔpK_a greater than 3 will lead to salt formation while values smaller than 0 will result in cocrystal formation as reported by Nangia[21] and that parameter is considered inappropriate for accurately predicting salt formation in the solid state when values of ΔpK_a are between 0 and 3[22].Apart from the mere definition, it is of utmost importance to discern the differences between salts and cocrystals. Salts are ionic compounds which differ from their corresponding neutral molecule: chemical-physical properties may be altered. Active pharmaceutical ingredients (APIs), for example, are usually administered in the solid state because that form provides a convenient and reliable compact format to store a drug and typical ways to change their properties include the formulation of salts, solvates and polymorphs[23 24]. Converting a drug into a salt through this process can increase its chemical stability, render the complex easier to administer and allow manipulation of the pharmacokinetic profile. Salt selection is a widespread operation usually performed with small molecules during drug development, and in many cases the drug salts display preferential properties as compared with the parent molecule. As a consequence, there has been a rapid increase in the number of drugs produced in salt form, so that today almost half of the clinically used drugs are salts. Despite of this classical approach, the design of cocrystals have recently received particular attention in the pharmaceutical field for many reasons[25]. Cocrystals may enhance pharmaceutical properties by modification of chemical stability, bioavailability, mechanical behavior, dissolution rate or solubility for non-ionizable

compounds. In addition, the inclusion of a proper coformer, which is able to self-assemble with the API molecule, may lead to an exotic and particular formulation of a specific drug, altering the physico-chemical properties while keeping the molecular structure and composition of the individual components constant. Cocrystallizations have also been used for chiral resolution, separation and purification[26]. Last but not least, cocrystals are patentable solid forms useful to expand IP portfolios, hence of paramount importance for industries.

1.5 Cocrystallization as a tool for stabilizing molecules

Molecules with different functionalities can be brought together relying on a wide weak intermolecular interaction landscape, ranging from 5 to 20 kJ mol^{-1}. A singular approach that completely differs from the classical covalent bonding chemistry, mostly for functionality which plays a key role in designing specific supramolecular moieties able to self-organize. Cocrystallization of volatile compounds, however, is an intriguing challenge, above all if the molecule of interest is of any industrial or pharmaceutical interest. Chemical cocrystallization of two chemical entities has already proved out to be a valid alternative to physical condensation for the storage of gaseous compounds such as acetylene[27 28 29] as well as novel techniques of in situ cocrystallization of gases and liquids has been reported in literature[30]. Aakeröy *et. al* have reported the stabilization of volatile iodoperfluoroalkanes, that are generally recognized as persistent potential pollutants (POPs), or even explosives, through cocrystallization in recent works[31]. Stabilization of liquid APIs is of enormous interest for pharmaceutical industries especially if we consider the purpose of stabilizing the pharmaceutical ingredients for storage, transportation and handling and most drugs are formulated as solid dosage because they tend to be reproducible and amenable to purification.

Formation of solid cocrystal can be schematized using the phase diagrams as reported in figure 2. Starting from a liquid compound A (melting point below T_{room}) and a solid compound B (melting point above T_{room}) two principal cases could be observed. If no particular favorable interactions are established between the two species, a simple mixture of the two components is formed, characterized by the progressive decrease in melting point. On the

other hand, if cocrystal forms, a new phase appear with new and specific physico-chemical properties including melting point. It is important to specify that the phase diagram reported is only valid at constant pressure and in the case the two solids components are immiscible and the two liquid components are completely miscible. Hence it is desirable to aim for the synthesis of cocrystal phases with melting points above room temperature and in particular, if possible, next to or above 100°C, which is considered a target temperature of stability from an industrial point of view.

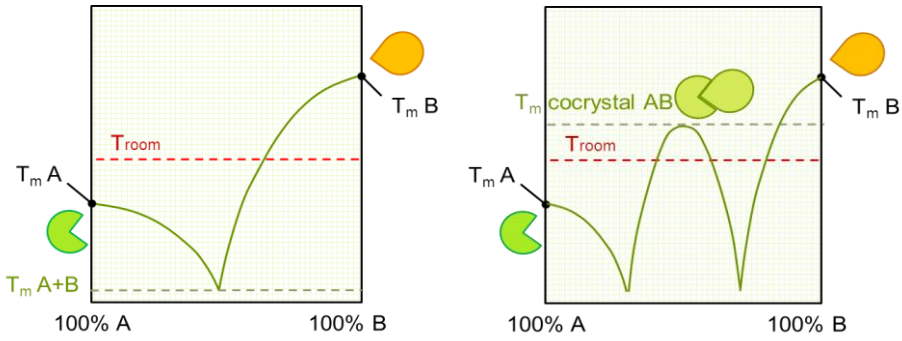

Fig. 2 Phase diagrams reporting solid mixture of liquid component A plus solid component B (on the left) and formation of a new solid cocrystal phase made up of liquid A combined with solid B (on the right).

1.6 MOFs: the entrapment approach for stabilizing liquids

Coordination polymers are coordination compounds with repetitive units extending in one, two or three dimensions. Metal organic frameworks (MOFs) are a subclass of the coordination polymer broad family. MOFs are an interesting and novel class of porous materials consisting of metal ions or clusters coordinated to organic ligands with peculiar three-dimensional architectures. The MOF field have recently received particular interest as attested by the constant increase of publications, citations and research efforts (as shown in fig. 3).

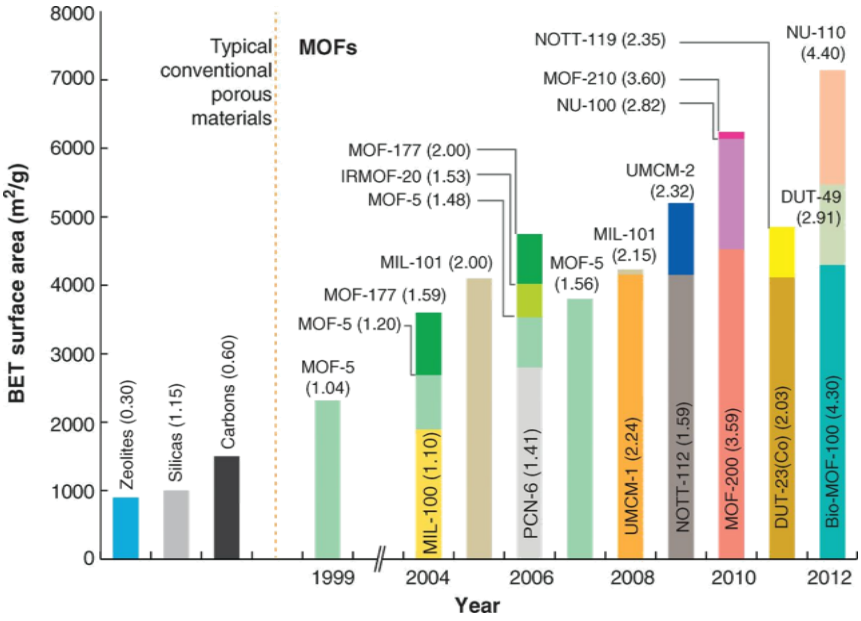

Fig. 3 Progress in the synthesis of ultrahigh porosity MOFs. Brunauer-Emmett-Teller (BET) surface areas of MOFs are reported vs year of publication. Pore volumes (cm^3/g) are reported in parentheses [32].

One of their most appealing characteristic is flexibility, which represents a key advantage compared to their organic (carbons) and inorganic (zeolites, silica) counterparts: both metal structural building units (SBUs) and organic linkers can be varied, leading to thousands of different compounds. Structural variation is of extreme importance if we consider the cavities of the frameworks: thanks to the capacity of designing ligands and coordination nodes it is possible to control the size and shape of the cavity and purposefully build a cage for a particular application. Most common use of MOFs are adsorption and storage of gas[33,34,35], separation[36], environmental conservation[37,38], heterogeneous catalysis[39,40], luminescent materials[41].Introduction of reticular synthesis by Yaghi and O'Keeffe's groups [42,43]and post-synthetic modifications (PSMs) [44,45]opened new paths to properly design new kind of MOFs.

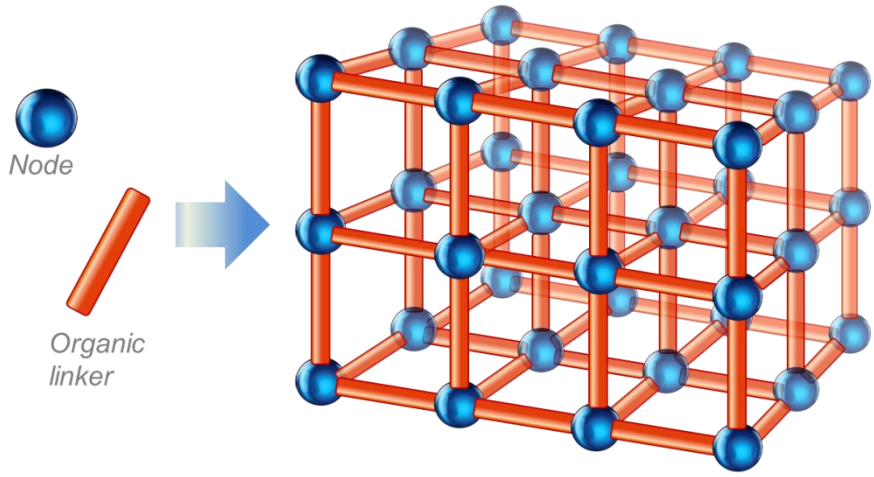

Fig. 4 Scheme of a metal organic framework structure.

The molecular storage-release capabilities of MOFs combined with their high and regular porosity allow these materials to be exploited as novel delivery systems for active species (e.g. drugs, vaccines, genes, etc.) in the fields of medicine, pharmaceutics and cosmetics. For instance, Rosi et al. demonstrated controlled drug release (*procainamide* HCl) of Zinc-adeninate metal organic framework [46]; biodegradable porous iron(III) polycarboxylates MOFs with high loadings of antitumoral or antiretroviral drugs have been recently developed [47]; experimental and computational systematic explorations of the driving forces related to the encapsulation of caffeine were performed using various MOFs by Serre *et al.*[48].

One of the most striking result was obtained by Fujita *et al.*[49] using networked porous materials as 'crystalline sponges' for guests inclusions. Thanks to the high molecular recognition ability of the pores, the crystalline sponges can absorb a large variety of target sample molecules from solution, rendering these guest molecules ordered in the crystal. This approach may overcome the SC-XRD analysis intrinsic limitation which lies on the requirement of having single crystals: crystallographic analysis determined the absorbed guest structures along with the host frameworks working with just trace amounts of samples (<0.1 μg).

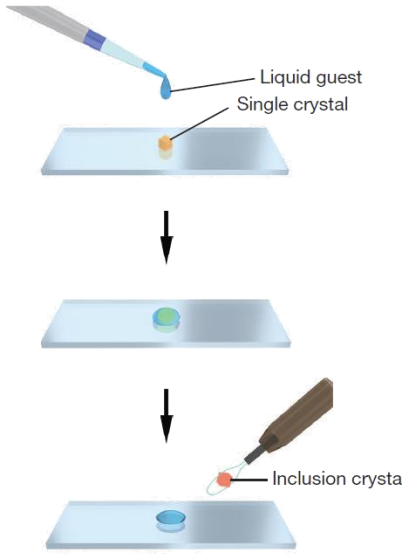

Fig. 5 Experimental preparation of a guest included network complex: a single crystal of the MOF was soaked in liquid guest for 2 days and eventually analyzed with SC-XRD.

1.7 Cocrystal synthesis

Cocrystals can be prepared from two (or more) molecules of any shape and size able to interact through proper functional groups. Many parameters concur in cocrystal formation, such as API - coformer ratio, temperature, solvents, pressure, making experimental screening for cocrystals not trivial. Synthesis of cocrystals can be accomplished via a number of methods, including slow solvent evaporation crystallization from solution, slurrying, solvent-free methods (grinding, kneading, direct mixing) melt, vapor diffusion crystallizations.

1.7.1 Evaporation from solution

This is the simplest technique for air stable samples. A near saturated solution of the partners is prepared in a suitable solvent, usually left in a sample vial that has a perforated cap. The size of the perforations is an experimental variable that depends to some extent on the volatility of the sample. It is desirable to incline the tube so that some of the crystals grow on the side of the tube. This facilitates easier removal of delicate crystals without damage. Other variations on this method are to transfer some of the solution to a crystallization dish and cover with perforated aluminium foil, or to trap some of the solvent between microscope slides. Evaporation of the solvent increase the concentration of the solute in the solvent up to its solubility limit and induce nucleation and consecutive growth.

1.7.2 Vapor diffusion crystallization

A solution of the sample contained in a small sample tube is placed in a larger tube containing a second less efficient solvent (antisolvent) and this tube then sealed. The method works best if the solution solvent is the less volatile and thus predominately the second solvent diffuses into the sample solution. Slow diffusion allows for gentle and gradual changes in concentration of solute which aid in the growth of a large crystal suitable for SC-XRD analysis.

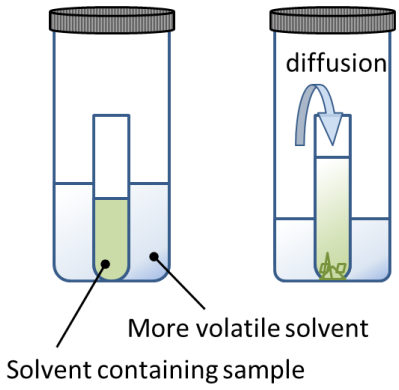

Fig. 6 Setup for the vapor diffusion experiment.

1.7.3 Mechanochemical methods

Thanks to combination of mechanical and chemical phenomenon a molecular scale it is possible to synthesize chemical products. Mechanochemistry has been used for a long time for inorganic materials and, more recently, has been applied in the synthesis of organic molecules[5051]. Current applications of mechanochemistry can be seen in almost all kinds of organic transformations such as cocrystal formation and classic organic syntheses. Not only mechanosynthesis is a green process, but has many other attractive aspects as well. For example, yield values are usually higher than 90% and generally>99%, and the selectivity reduces the formation of by products and eliminates purification steps for pharmaceutical ingredients and medicines.

E. Boldyreva has recently rationalized and summarized the mechanochemical approach[52]:for all reactions involving more than one phase bringing reagents into contact and removing the product becomes very important. Reactions occur at the interfaces between the phases. As soon as a reaction starts, phenomena can be related not only to the generation of mechanical strain, but also to local heating, to redistribution of electrons and holes at a contact between two solids, to changes in concentration of point defects, to formation of interactions (e. g. hydrogen bonds) at the interface. Reactions can be affected by improvement of diffusion, structural, electronic and ionic defects, increase of localized pressure and temperature.

A small amount of liquid can be specifically added to a mixture of two or more solids. This is what is called as “kneading” or “liquid assisted grinding”. Solvent is usually not present in the final product of the synthesis, but its presence in the starting mixture, or as a vapor in contact with the solid sample, is necessary to make the synthesis possible. In this case the mechanism of the reaction and the role of the liquid are not well understood. Some hypothesis that reagents are locally dissolved at the contact with the solvent and that reaction always take place in solution [53] was not confirmed by later experiments[54]. One possible explanation could be related to the existence of hydrothermal conditions in a mill, implying combination of high temperature, pressure and concentration of solvent [55]. Eventually, examples are known in which adding different solvents or exposing the solid mixture to different vapors results in the formation of different products[56].

1.8 Thermal analysis

Calorimetry is a primary technique for measuring the thermal properties of materials to establish a connection between temperature and specific physical properties of substances. It is widely used in the pharmaceutical field and in material sciences and is the only method for direct determination of the enthalpy associated with the process of interest. DSC is a thermal analysis apparatus measuring how physical properties of a sample change, along with temperature against time[57]. In other words, the device is a thermal analysis instrument that determines the temperature and heat flow associated with material transitions as a function of time and temperature[58]. During a change in temperature, DSC measures a heat quantity, which is radiated or absorbed excessively by the sample on the basis of a temperature difference between the sample and the reference material. In a heat flux DSC, the sample material, enclosed in a pan, and an empty reference pan are placed on a thermoelectric disk surrounded by a furnace. The furnace is heated at a linear heating rate, and the heat is transferred to the sample and reference pan through the thermoelectric disk. However, owing to the heat capacity of the sample, there would be a temperature difference between the sample and reference pans, which is measured by area thermocouples, and the consequent heat flow is determined by the thermal equivalent of Ohm's law:

$$q = \Delta T/R$$

where q is “sample heat flow”, ΔT is “temperature difference between sample and reference”, and R is “resistance of thermoelectric disk”[59].

Hot stage microscopy (HSM), is the combination of microscopy and thermal analysis to enable the study of materials as a function of temperature and time. Besides obtaining information about particle size and particle morphology, the visual examination gives valuable information about the compound with regard to melting point and other transformations during heating. This technique gives a unique opportunity to visually follow thermal changes such as monitoring melting range (which depends on the purity), crystal nucleation and crystal growth.

The material under investigation is placed onto the microscope stage. A color camera is attached to the microscope for observation of the visual

changes. A high resolution color video camera is especially used when the pharmaceutical substances exhibit multiple transitions in small temperature ranges. The hot stage controller which is attached to the system monitors the temperature program as well as transmits the thermal analysis data to a computer for processing and analysis.

1.9 Ternary phase diagrams

Ternary phase diagrams are plotted as equilateral triangles with the three components which define the system, placed at their apices. At the apex there exists 100% of that component and 0% of the others. Moving away from the apex, the proportion of the component at the apex decrease as the proportion of the two other components increase. There are two main practical and simple methods for the determination of the composition of a point within the diagram: the use of a grid (as shown in fig. 7) and the two lines method (fig. 8).

In the method of the triangular grid the proportion of any point (e.g. composition at point Q) within the triangle can be represented by grid lines drawn through the point of interest, parallel to each side of the triangle. Percentages of components A, B and C increase moving toward the respective angle.

A second method is based on two lines which are drawn through point Q parallel to any two sides of the triangle (AB and AC). The intersection of these two lines with the third side (BC) divides this side into three line segments. The lengths of the individual segments are proportional to the relative amounts of the three components A, B and C.

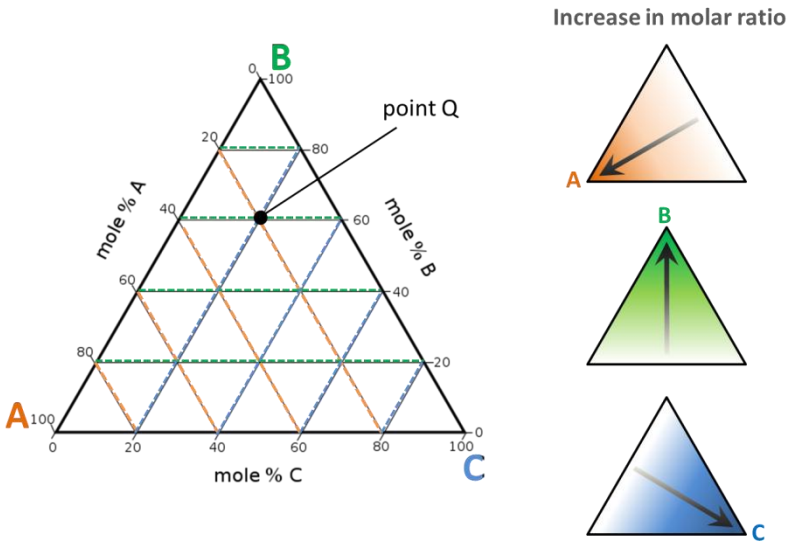

Fig. 7 Method of the triangular grid. Composition of point Q is: A 20%, B 60%, C 20%.

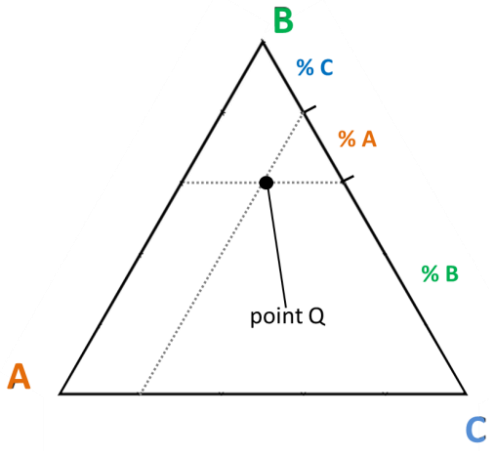

Fig. 8 Two lines method.

1.10 Cocrystals phase diagrams

Ternary isotherm between two solutes (e.g. drug and coformer which co-crystallize giving a stoichiometric compound) and a solvent, could be represented using equilateral triangles diagrams as reported in various works[606162]. Triangular diagrams are isobaric and isothermal slices for prismatic diagrams where the z-axis represents temperature. An example of a classic 3 phases diagram for API, coformer and solvent is reported in figure 9 as well as its distinctive zones.

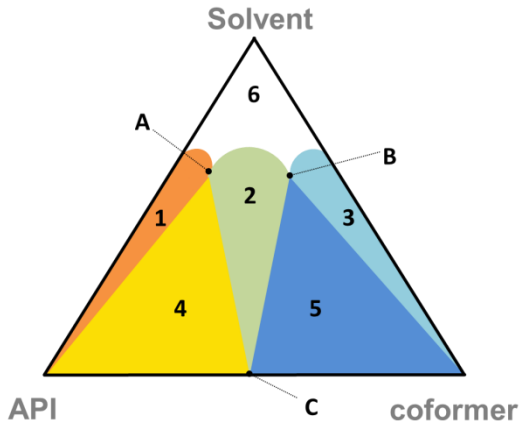

Fig. 9 Typical ternary phase diagram for a solid API - solid coformer-solvent system.

In order to understand the construction of the diagram, it is useful to consider the Gibbs rule of phases.

$$f = c - p + 2$$

f = intensive degree of freedom or variance

c = number of independent components

p = number of phases

2 stands for the external parameters: temperature and pressure

Considering a typical system in isothermal and isobaric conditions (such as the one in fig.9) it is possible to ignore 2 degrees of freedom, so external parameters lower to zero.

Gibbs rule of phases for the analyzed system results, therefore:

$$f_T = 3 - p$$

It is noticeable how variance (f_T) simply relies on the number of phases of the system, so that every characteristic point of the diagram has a specific variance. Eutectic points (A, B), for instance, are distinguished for a variance value of 0 and they are so called "invariants"; this means there are no intensive variables that can be changed independently without disturbing the phases in equilibrium at the eutectic point. Focusing on the curved lines (situated between zones 1-6, 2-6 and 3-6), they are all characterized by variance values of 1, hence the system is forced to rely on a curve with only one degree of freedom. Eventually zone 6 possesses two degrees of freedom and is geometrically represented as a surface. A detailed description of each phase of the ternary phase diagram of fig. 9 is reported in table 1.

Table 1

Variance f_T	Phases	Description
2	1	Zone 6: pure solvent as a homogeneous liquid phase whose composition varies in the area.
1	2	Zone 1: pure API in equilibrium with liquid (solvent containing API whose composition changes along the curve between zone 1 and 6).
		Zone 2: pure solid cocrystal in equilibrium with liquid (solvent containing API and coformer in a variable composition that changes along the curve between zone 2 and 6).
		Zone 3: pure coformer in equilibrium with liquid (solvent containing coformer whose composition changes along the curve between zone 3 and 6).
0	3	Zone 4: pure solid cocrystal and pure API are in equilibrium with a fixed liquid composition (eutectic point A). Any point in zone 4 is a heteroge-

	neous mix of the 2 solids and the fixed liquid. Zone 5: pure solid cocrystal and pure solid coformer in equilibrium with a fixed liquid composition (eutectic point B).Any point in zone 5 is a heterogeneous mix of the 2 solids and the fixed liquid.

1.11 Solubility measurements

The most important methods to evaluate cocrystal solubility are based on thermodynamic and kinetic approaches. Thermodynamic equilibrium experiments provide a measure of cocrystal solubility processes, while kinetic studies provide observation of the time scale and concentration fluctuations during cocrystal dissolution. An important property of cocrystals is that their solubility is highly dependent on the activities or concentrations of cocrystal components in the solution phase. Cocrystals dissociate into their individual components and the equilibrium is described by a solubility product equivalent to the one used for ionic systems. Hence, a small excess of coformer in the solid cocrystal phase may significantly decrease the equilibrium solubility if one is relying on the analytical concentration of drug as the only measure of cocrystal solubility. It is necessary to measure the concentrations of all cocrystal components in the solution phase at equilibrium as reported in literature[63] in order to correctly evaluate the characteristics of the system. Calculation of the cocrystal solubility product (K_{sp}) is therefore necessary and clearly useful. Cocrystal solubility and stability domains can be readily characterized by evaluating the eutectic point at the three-phase equilibrium between *cocrystal-drug-solution phase* and *cocrystal-coformer-solution phase* (points A and B in fig. 9). This is crucial when characterizing metastable cocrystals which convert to drug or to coformer solid phases when exposed to solution. Since at the eutectic point the solution is saturated with two solid phases, their concentrations ($[drug]_{eu}$ and $[coformer]_{eu}$) are independent of the ratio of the phases. Comparing eutectic concentrations with the cocrystal stoichiometry provides extremely important information about the solubility of the system. If we consider, for instance, a 1:1

ratio cocrystal and experimental turned out to be: $[coformer]_{eu} > [drug]_{eu}$, then cocrystal solubility is greater than drug solubility. Accordingly, eutectic points represent important indicators of cocrystal solubility.

1.12 Solubility product of cocrystals

Equilibrium of an API (A) and a coformer (B) which give a cocrystal, may be represented by the following reaction:

(1) $$A_aB_{b\,(s)} \rightleftharpoons aA_{(aq)} + bB_{(aq)}$$

This constant is analogous to the solubility constant of a salt, defined by the product of ions concentrations. Consequently, the equilibrium constant for this reaction is given by the thermodynamic activity product of the cocrystal components:

(2) $$K_{eq} = \frac{a_A^a a_B^b}{a_{AB}}$$

The solubility product (or solubility costant), K_{sp}, is the equilibrium constant for a solid compound dissolving in aqueous solution and can be expressed, by approssimating activity to molar concentration, as follows:

(3) $$K_{sp} \simeq [A]^a [B]^b$$

K_{sp} reflects the strength of cocrystal solid state interactions of drug and coformerrelative to interactions with the solvent. Cocrystal solubility is also a function of the solubility product as reported in eq. 5. The mass balance for each component in solution, considering a 1:1 stoichiometry cocrystal that dissolves in a solvent into its components, could be expressed by the molar solubility S. If [A] = S and [B] = S, and substituting these in eq. 3, gives:

(4) $$K_{sp} = S^2 \quad \text{and} \quad S = K_{sp}^{1/2}$$

Therefore, more generally:

(5) $$S_{A_a B_b} = \sqrt[a+b]{\frac{K_{sp}}{a^a b^b}}$$

Eventually it is possible to plot a phase solubility diagram (as shown in fig. 10) with molar concentration of component A (or drug) against molar concentration of component B (or coformer) using the calculated K_{sp}. It is necessary to consider that the diagram is valid only if no complexation nor ionization of the components occur and that solubility of the drug is independent of the concentration of coformer in solution.

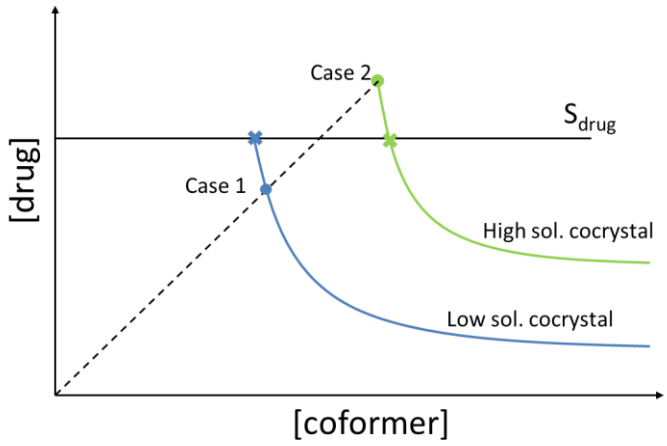

Fig. 10 Example of phase solubility diagram showing two different kind of cocrystals: case 1 (stable cocrystal), case 2 (metastable cocrystal).

Both blue and green curves in fig. 10 are calculated using K_{sp}. X marks represents the transition concentrations (invariant points) where the cocrystal curves cross the line of the intrinsic solubility of the drug. This is the point where both drug and cocrystal are in equilibrium with a solution containing drug and coformer at a certain concentration which is called transition concentration ($[A]_{tr}$ and $[B]_{tr}$)[64 65]. Colored dots on the curves represent the solubility of cocrystals in pure solvent and are located at the crossing point of stoichiometric concentration of the cocrystal (dashed line) and cocrystal solubility curves. For congruently saturating cocrystals (case 1) the drug concentration is lower than the pure drug at the crossing dots. Solubility of con-

gruently saturating cocrystals can be readily measured from solid cocrystal dissolved and equilibrated with the solution. In the case of a metastable cocrystal (case 2), the crossing dot is upon the intrinsic solubility line (the horizontal line in fig. 10) of the pure drug. Therefore, the drug concentration associated with the cocrystal solubility is greater than the solubility of the stable drug form. Thanks to this characteristic, as the cocrystal dissolves along the stoichiometric line, the drug released in solution can crystallize because the saturation limit has been exceeded and, most important fact, the solubility of a metastable system is not a typical measurable equilibrium.

1.13 Chemical library

1.13.1 APIs, nutraceuticals and other molecules of interest

Propofol (2,6 - diisopropylphenol) is marketed as DIPRIVAN® which is a sterile, nonpyrogenic emulsion containing 10 mg/mL of propofol suitable for intravenous administration [66]. It is commonly used for induction and maintenance of general anesthesia and sedation and appears on the WHO Model List of Essential Medicines, the most important medications needed in a health system[67].

Nicotine [Pyridine, 3-(1-methyl-2-pyrrolidinyl)-, (S)-] is a liquid toxic alkaloid found in the leaves of the tobacco plants *Nicotianatabacum* and *Nicotianarustica* of the family *Solanaceae*[68] and it is known for being a nootropic stimulant drug. Because of its properties, nicotine has been of commercial interest and employed for widely differing kinds such as therapeutic use in treating nicotine dependence or as an insecticide[69]. Nicotine can act as Lewis base and is capable of forming monocationic and dicationic species (pK_{a1} = 3.13, pK_{a2} = 8.24[70]) as long as various salt: hydroiodide[71], salicylate[72], 3-carboxy-4-hydroxybenzenesulfonate[73]. An intriguing aspect of nicotine lies in the facts that no crystal structure of the molecule itself has never been reported in literature and this peculiarity may be ascribed to the liquid-glass transition that occurs when nicotine is supercooled under its melting point (-79°C). The difficulty in freezing nicotine as a pure compound in crystal form along with keeping its properties unchanged may be overcome with cocrystallization. Only one cocrystal of nicotine has been reported in literature[74]

but no real stress has ever been given to the importance of stabilizing that compound through this methodology.

The area of research on nutraceuticals is in constant expansion, not only due to the potential health benefits associated with this class of compounds, but also because of their perceived therapeutic effect in multiple areas of medicine such as pain killers, cold and cough, sleeping disorders, digestion, and prevention of certain cancers[75].

Thymol and carvacrol are isomeric natural compounds derivatives of *p*-cymene which can be found in oregano and oil of thyme. They are part of a naturally occurring class known as biocides which possess strong antimicrobial attributes. For example, Carvacrol prevents the growth of several bacteria strains, e.g. *Escherichia coli*[76] and *Bacillus cereus*. Its low toxicity together with its pleasant taste and smell suggests its use as a food additive to prevent bacterial contamination[77]. In *Pseudomonas aeruginosa* bacteria it causes damages to the cell membrane and inhibits their proliferation[78]. Research demonstrates that thymol and carvacrol reduce bacterial resistance to antibiotics through a synergistic effect[79], and thymol has been shown to have antioxidant properties[80] and anti-inflammatory properties in vivo and vitro[81]. Only the crystal structure of thymol (ref. code IPMEPL) and inclusion compounds are deposited in the Cambridge Structural Database (CSD).

Eucalyptol (EU) is another natural compound found in many plants, it is a cyclic ether with a melting point of 1.5°C. It is used as an ingredient in many brands of mouthwash and cough suppressant and as an insecticide and insect repellent[82]. Thanks to its oxygen atom, eucalyptol is able to accept hydrogen bond interaction and it is suitable for cocrystallization experiments. Only one cocrystal structure containing eucalyptol is present in the CSD[83].

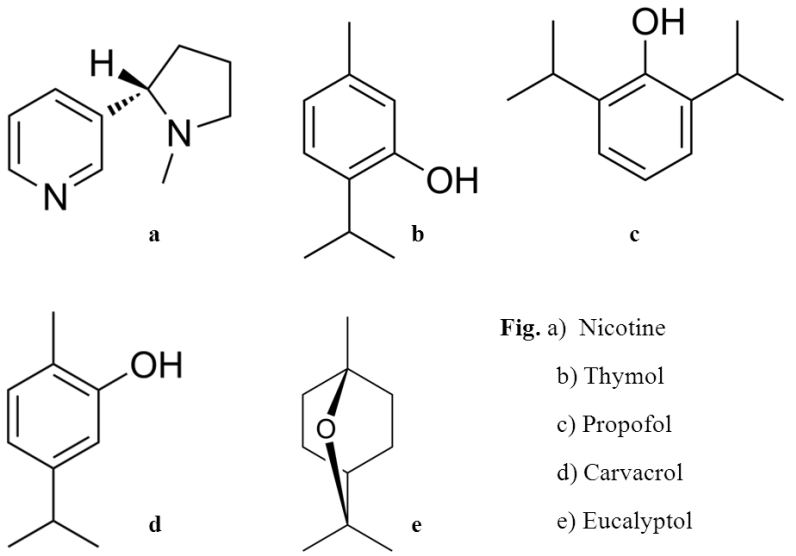

Fig.11 List of reagents.

Table 2 Melting points of molecules of interest.

	Propofol	**Nicotine**	**Thymol**	**Carvacrol**	**Eucalyptol**
Melting point (°C)	18	-79	50	1	1.5

1.13.2 Valid coformers

Propofol, thymol and carvacrol are capable of forming hydrogen bond interactions thanks to the hydroxyl group. Since O-H···N is one of the most robust and well-studied synthons in crystal engineering, the choice of proper hydrogen bond acceptors was focused on selecting specific molecules containing nitrogen atoms of aromatic rings. Among these selected partners particular attention was paid to 4,4'-bipyridine and phenazine because they proved out to be valid cocrystallization partners in previous works[84]. Since the Seventies phenazine (PH1) and its derivatives have been employed as immune regulatory agents capable of altering the immune response in mammals[85], thanks to their antimicrobial activity[86] or for the treatment of autoimmune and inflammatory diseases[87]. Many previous works report the efficiency of phenazine in giving cocrystal structures[88]. 4,4'-bipyridine (B1)

has been used in many previous works as a valid coformer to obtain cocrystals thanks to its pyridinic nitrogen atoms, which represent suitable hydrogen bond acceptors, and its planarity along with the capacity to interact through π-π stacking motifs[89].

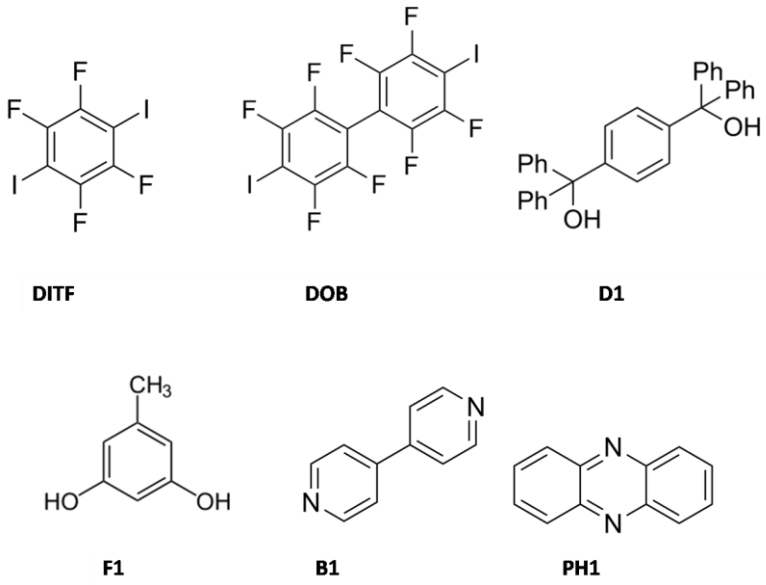

Fig. 12 List of coformers.

The choice of coformers for nicotine was limited to small organic molecules able to interact through suitable functional groups. Promising synthons have been selected considering both hydrogen bond interactions and halogen bond interactions: halogenated benzene derivatives, in particular diiodoperfluorurate aromatic derivatives (DITF and DOB), have been described as great halogen bond donors (electron acceptors)[90], while diole aromatic derivatives have been chosen for their ability to interact, as hydrogen bond donors, with both pyridinic and pyrrolidinic nitrogen atoms. Previous works reported in literature show how effective 4,4'-*bis*(diphenylhydroxymethyl) derivatives could be in forming valid hydrogen bond interactions[91]. The possibility to design spacers of different length may lead to a wide landscape of arrangements which is a key point and an extremely powerful tool in crystal engineering. 4,4'-*bis*(diphenylhydroxymethyl)benzene (D1 in fig. 12) and 4,4'-*bis*(diphenylhydroxymethyl)biphenyl are wheel and axle molecules which have been used efficiently for enclathrating guest molecules such as

amides and 1,4-dioxane through hydrogen bonds[8]a-c. It is due to this successful result that we aimed to design cocrystals of 4,4'-*bis*(diphenylhydroxymethyl)benzene and nicotine.

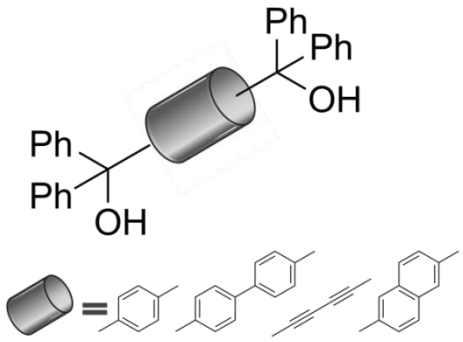

Fig. 13 Design capability of the aromatic spacer.

A large number of phenol derivatives (orcinol, resorcinol, *m*-cresol, *p*-cresol, phloroglucinol, 3,5-xylenol) were taken into account with the purpose to find a proper partner for eucalyptol. Hydroxyl groups could bond to the oxygen atom of EU through hydrogen bonds and the aromatic ring of the phenol derivative may interact through π-π stacking or CH-π interactions. Among all of these phenol derivatives, orcinol resulted in the most promising, least expensive and non-toxic coformer. Orcinol is a naturally occurring compound found in many species of lichen whose derivatives are widely used as antiseptics for skin diseases. Its polymorphic forms have been studied and reported in literature[92].

2. EXPERIMENTAL SECTION

2.1 Materials for cocrystallizations

2,6-diisopropylphenol (97%), phenazine, 4,4'-bipyridine, **(-)-**Nicotine (99%), 1,4-diiodotetrafluorobenzene (98%), thymol (98%), carvacrol (98%), eucalyptol (99%) and all the solvents for crystallization were purchased from Sigma Aldrich Chemical Co. and used as such in all crystallization experiments. 4,4'-diiodooctafluorobiphenyl has been synthesized starting from commercial precursor 4,4'-dibromooctafluorobiphenyl (98%) from Sigma Aldrich Chemical Co., following the reaction reported in literature[93]. 4,4'-*bis*(diphenylhydroxymethyl)benzene has been synthesized from commercial precursor dimethyl terephthalate (99%) from Sigma Aldrich Chemical Co.

2.1.1 Synthesis of D1

Preparation of Grignard reactive: Mg turnings (41 mmol, 0.996 g) were introduced in a 100 ml flask along with THF dry (15 ml) under N_2 flux. Bromobenzene (27.1 mmol, 2.8 ml) in THF dry (10 ml) was slowly added to the round bottom flask. A tiny small amount of I_2 might be added to initiate the reaction. The mixture was stirred for 2 hours at room temperature. Grignard reaction: G. reactive was added dropwise to a 100 ml flask containing dimethyl terephthalate (5.15 mmol, 1g) previously dissolved in THF dry (15 ml) under N_2 flux. Solution was stirred overnight at room temperature and eventually quenched by inserting 5ml of a water solution of NaOH (1M).

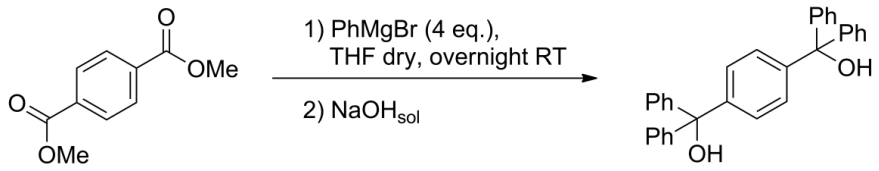

Crude reaction product was extracted with H_2O/dichloromethane in a separating funnel and organic phase was dried (Na_2SO_4) and concentrated under

vacuum. Pure D1 was then separated from the solid mixture through a chromatographic column (mobile phase: cyclohexane 9 : 1 ethyl acetate) with a yield of 59%. Final product was checked with ^{1}H NMR, ^{13}C NMR spectroscopy and mass spectrometry (MS EI-Direct exposure probe). ^{1}H NMR (300 MHz, $CDCl_3$) δ_H 7.31 (br m, 24 H), 3.02 (br s, 2 H). ^{13}C NMR (100 MHz, $CDCl_3$) δ_C81.9 (s C<u>O</u>H), 128.8, 128.0, 127.9, 127.6, 127.3, 127.2 (s, C aromatic), 146.7, 145.8 (s, <u>C</u>-C sp2).

2.2 Cocrystallization

Cocrystallization which lead to the formation of cocrystals of propofol-B1 and propofol-PH1 were attempted by slow evaporation from various organic solvents: methanol, ethyl acetate, dichloromethane. Cocrystals of propofol-B1 and propofol-PH1 were also prepared by *direct mixing method:* liquid API and solid coformer were added in 2:1 ratio into a ceramic mortar and ground for 1 hour until a sludgy solid was obtained and put into the fridge to facilitate nucleation. After 1 day a dry yellowish powder was formed and XRPD experimental pattern matched that simulated from the single crystal structure obtained from solution crystallization.

Cocrystallization which lead to the formation of cocrystals of **(-)-**Nicotine and related coformers (DITF, DOB and D1) were attempted in various organic solvents: ethyl acetate, tetrahydrofuran, methanol. Saturated solutions containing **(-)-**Nicotine and the proper coformer with 1:1, 1:2, 2:1 molar ratios were left to slowly evaporate at room temperature until tiny single crystals suitable for SC-XRD analysis formed.

Further cocrystallization experiments were performed using phenazine and thymol and phenazine and carvacrol obtaining interesting results. TH-PH1α crystals were obtained by slow evaporation of a 1:1 thymol : phenazine solution in ethyl acetate. TH-PH1α crystallized in form of yellow plates that melt at 90°C approximately, whereas thymol melts between 48 and 51°C and phenazine between 173 and 176°C, suggesting a cocrystal might have formed. TH-PH1β crystals were obtained by grinding and by slow evaporation of a thymol-phenazine 1:1 solution in acetone, methanol and THF. Similarly to TH-PH1α, TH-PH1β crystallized in form of thin yellow plates that melt

at 90°C approximately, suggesting the same cocrystal might have been obtained.

Sometimes the previous speculations about the choice of a proper coformer are not enough to predict the formation of a cocrystal. The most effective way to get to interesting results is the screening test. For this reason we performed many crystallization trials, testing an extremely vast landscape of conditions. The role of the solvent, for example, is crucial for two main reasons. First of all, the interactions established by solvent molecules and solute may affect the formation of critical nuclei, thus the crystallization. Last but not least, the volatility of the solvent is fundamental because it rules the velocity at which saturation is reached and affects crystallization as well.

One of the most difficult parameter to control is temperature. Working on various crystallization trials at the same time, results in the impossibility to keep the temperature under strict control in an large area, such as the one of the laboratory. Nevertheless, the temperature in the laboratory is influenced by environmental conditions, varying from 15°C during some winter days up to 30°C during summer period. Some crystallization trials were difficult to reproduce and in some cases they resulted in the precipitation of separated API and coformer (e.g. Nicotine and D1). All the cocrystallization trials performed are reported in the proper tables in the appendix.

2.3 Thermal analysis (DSC and HSM)

Most of the novel cocrystals (nicotine-DITF, nicotine-DOB, propofol-PH1, propofol-B1, EU-F1) were analyzed with differential scanning calorimetry technique in order to obtain specific information in relation with temperature. Hot stage microscopy was used only for nicotine-DITF and propofol-B1 cocrystal samples using a small amount of crystals (<1mg) placed on a flat microscope slide and a flat glass slit. The scanning temperature used was the same of the DSC analysis in order to reproduce a similar thermal experiment.

Differential scanning calorimetry analysis on cocrystals powder samples were performed with a PerkinElmer Diamond equipped with a model ULSP 90 ultra-cooler. Heating was carried out in open Al-pans at 5°C/min in the

temperature range from -25°C to 80°C. Thermomicroscopy (hot stage microscopy) studies were performed on a HSF 91 apparatus, Linkam Scientific Instruments, Tadworth, UK, and Labophot II polarizing microscope, Nikon, Tokyo, Japan. The enthalpy of the endothermic or exothermic event is determined by the integration of the area under the DSC peak, which is reported in J/g.

2.4 Slurry experiments

Thanks to the precious collaboration with the research group of prof. N. Rodriguez-Hornedo of the College of Pharmacy, Ann Arbor (MI), we were able to perform specific tests focused on solubility measurements in order to achieve important results about cocrystal in relation with a solvent.

Powder samples of cocrystal propofol-B1 were used to prepare slurries in pure distilled water. Different slurry conditions have been established in order to analyze different zones of the diagram thus different critical points:

- *Slu1*: slurry of cocrystal (89 mg) in H_2O (4ml).
- *Slu2*: slurry of cocrystal (89 mg) plus B1 excess (5 mg) added in H_2O (4 ml).
- *Slu3*: slurry of cocrystal (89 mg) plus propofol excess (5 µl) added in H_2O (4 ml).
- *Slu4*: slurry of B1 in H_2O.
- *Slu5*: slurry of B1 in propofol.

Slurries have been left sealed in glass vials (5 ml volume) with plastic caps, in constant agitation at room temperature for more than 2 weeks in order to reach the thermodynamic equilibrium. Samples of water solution were collected, filtrated in order to remove any solid in suspension and properly diluted for HPLC analysis.

2.5 Analytical measurements

The HPLC system used for the analysis is a DIONEX Ultimate 3000 Systems (Thermo Scientific) with a ACC-3000 autosampler, a high-pressure HPLC pump LPG-3400SD and UV–vis detector DAD-3000.

Calibration curves for propofol ($y = 25021x + 0.919$, $R^2 = 0.998$, ranging from $1{,}00 \cdot 10^{-5}$ M to $1{,}00 \cdot 10^{-4}$ M) and B1 ($y = 35723x$, $R^2 = 0.999$, ranging from $1{,}00 \cdot 10^{-6}$ M to $4{,}00 \cdot 10^{-5}$ M) dissolved in water were built before starting the analysis. The HPLC method used for propofol and B1 in H_2O consists in a Kinetex column 2.6u C18, 100A, 100x2.10 mm; isocratic mobile phase acetonitrile/H_2O (40:60); constant flux of 0.200 ml/min; total run length of 30 min.

Calculation of the water content in propofol, for the determination of point A in the ternary phase diagram, was performed with Karl-Fischer titration method using a Karl Fischer TitroMatic KF 1S.

2.6 SC-XRD and XRPD analysis on cocrystals

Single crystal x-ray diffraction analysis was performed on single crystal samples at room temperature (293 K) on a SMART APEX2 diffractometer using Mo Kα radiation (λ = 0.71073Å) for nicotine-DITF, propofol-B1, AMα, AMβ, carvacrol-PH1. Lorentz polarization and absorption correction were applied. Propofol-PH1, nicotine-DOB and nicotine-D1 were collected at 100 K under nitrogen flux at *Elettra Sincrotrone* (Trieste, Italy) on beamline XRD1 with synchrotron radiation. The source used for the analysis was a NdBFe Multipole Wiggler (Hybrid linear), 4.27 keV with a power of 8.6 kW, a source size FWHM of 2.0 x 0.37 mm (0.7 x 0.2 mm FWHM beam size at sample) and photon flux 10^{12}-10^{13} ph/sec. Structures were solved by direct methods using SHELXS[94] and refined by full-matrix least-squares on all F^2 using SHELXL implemented in Olex2 [95]. For all the structures, anisotropic displacement parameters were refined except for hydrogen atoms.

X-ray powder diffraction analysis was performed on a Thermo Scientific ARL XTRA powder diffractometer (Cu Kα, 1.540598 Å) in order to rapidly check most of the new formed powder samples obtained by grinding. XRPD data

were collected for both 1:1 and 2:1 thymol-phenazine ground powders in order to assess the specific molar ratio of the new species.

2.7 Inclusion in MOFs: materials

The molecules of interest that have been chosen for the inclusion experiments are nicotine and propofol. Two different kind of MOFs have been chosen for this specific purpose: H-KUST and PCN6'. These are already known MOFs whose synthesis are reported in literature[96] that are quite easy to synthesize, cheap and reproducible and, above all, reflect the characteristics of an ideal molecular cage where it is possible to entrap the chosen molecules. H-KUST is a microporous MOF with cavities of 9 Å diameter, made up of a *paddle-wheel* dimer of Cu^{2+} coordinated, in the equatorial sites, by carboxylate groups of the ligand, the trimesic acid. The axial sites are coordinated by water molecules that complete the octahedral coordination of the metal ion.

PCN6' is isostructural to H-KUST but presents internal cavities of 30 Å diameter and channel cavities of 21.4 Å, hence it is classified as mesoporous. Its *paddle-wheel* is similar to the one of the H-KUST but the ligand used in this case is the 4,4',4''-s-Triazine-2,4,6-triyl-tribenzoic acid (TATB), a larger molecule that leads to a final greater structure. The synthesis of PCN6' reported in literature[97] involves the use of a templating agent (oxalic acid) in order to avoid the formation of an interpenetrated species known as PCN6 (fig. 14), with the same metric of the PCN6'. However, following the synthetic path reported in literature and narrowly varying it many times, the formation of the second phase (PCN6) was unavoidable, as checked with XRD analysis. In every synthesis, the final product was always a mix of the two phases and the crystals are completely identical from a macroscopic point of view and it is impossible to distinguish them just using the microscope. It is therefore appropriate the use of the term PCNmix, indicating the presence of both the phases.

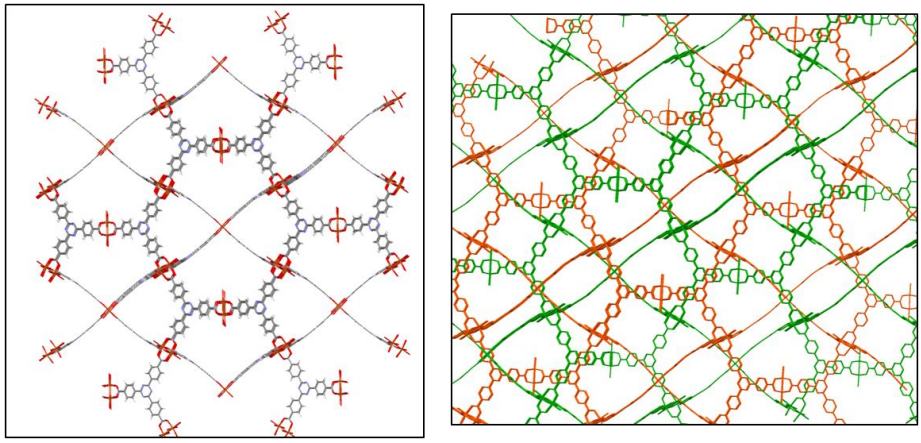

Fig. 14 PCN6' (on the left) and PCN6 (on the right) structures.

2.7.1 Synthesis of H-KUST

$Cu(NO_3)_2 \cdot 3H_2O$ 0.742 g (3.1 mmol) were added to a rotaflow with DMF (3 ml), EtOH (3 ml), H_2O (3 ml), following, 0.424 g (2.0 mmol) of trimesic acid (ligand) were added. The reactor was sealed using a Teflon cap and inserted in a oil bath at a controlled temperature of 85°C for 24h. Once the reaction was ended, the system was left to slowly reach room temperature by simply removing it from the oil bath. H-KUST was then filtrated using a Buchner filter, eventually obtaining a solid light blue crystalline material (1.095 g, 1.41 mmol, 47.2% yield).

2.7.2 Synthesis of PCN6mix

$Cu(NO_3)_2 \cdot 3H_2O$ 0.204 g (0.845 mmol) were added to a 20 ml screw neck test tube and dissolved with 4 ml of DMF. After that, TATB (previously synthesized) was inserted in the tube (0.080 g, 0.181 mmol) and then sonicated for 2 minutes in order to facilitate the fragmentation of large particles and their dissolution. Finally, 0.016 g (0.127 mmol) of oxalic acid (templating agent) were added and the system was put inside a oil bath at 85°C for 48h. Once the reaction is complete, tiny light blue crystal with octahedral shape were visible. It was extremely difficult to evaluate the amount of pure product synthesized (and also the yield) because secondary products were present in

the solid product material. It was impossible to remove those undesired products in any fast and practical way without losing the desired product.

2.7.3 Activation of the MOF

Activation of the solid material is necessary in order to remove the solvent trapped within the cavities, making the porous material accessible to the molecules for later experiments.

H-KUST crystalline material has been activated in a proper oven at 120°C for 24h. Thermal activation is efficient and particularly easy to monitor, considering that the MOF changes its color from light blue (when it retains solvent) to deep blue (once it is activated). The visible change of color (fig. 15) is due to the loss of water molecules that coordinates the copper atom of the *paddle-wheel*, this lead to a modification of the extent of the splitting in the d-d transition.

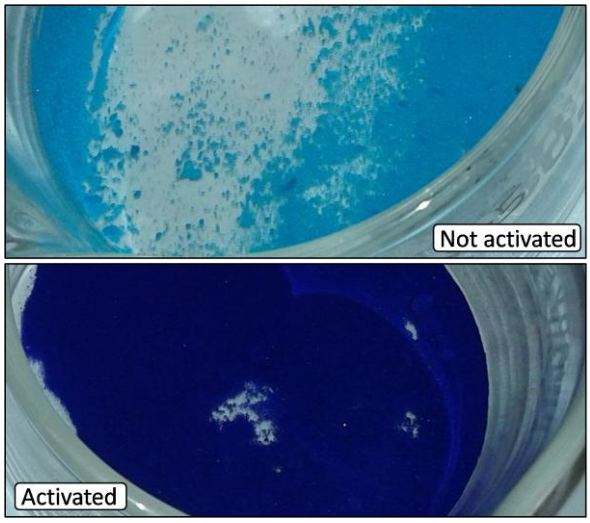

Fig. 15 Color differences between not activated and activated H-KUST crystals.

PCN6mix crystalline material has been activated through consecutive solvent exchange because a standard thermal activation in oven would lead to an evident deterioration of crystals' shape and quality. First of all the crystals were washed with dimethylformamide (DMF): 10 ml of solvent were put

in the reactor and this was agitated in order to leave in suspension the white subproduct (copper oxalate) and letting the crystals of the MOF deposit on the bottom of the vial. The suspension was then removed using a Pasteur pipette and redone three times. Subsequently, the DMF was exchanged by removing the most of it and adding 10 ml of methanol. This action was repeated many times, crystals should never be left in contact with air (in order to avoid the possibility of inclusion of water molecules), until the solvent left in the vial was MeOH. The system was left at rest for 24 hours at room temperature. Last solvent exchange involved dichloromethane (DCM) and was performed with the same steps described for the MeOH exchange. After 24 hours in DCM, the crystals were dried using vacuum pump ($P = 10^{-3}$ Torr) for one night. Different solvents lead to different crystal colors as shown in fig. 16 and the final activated and dried crystals were dark blue.

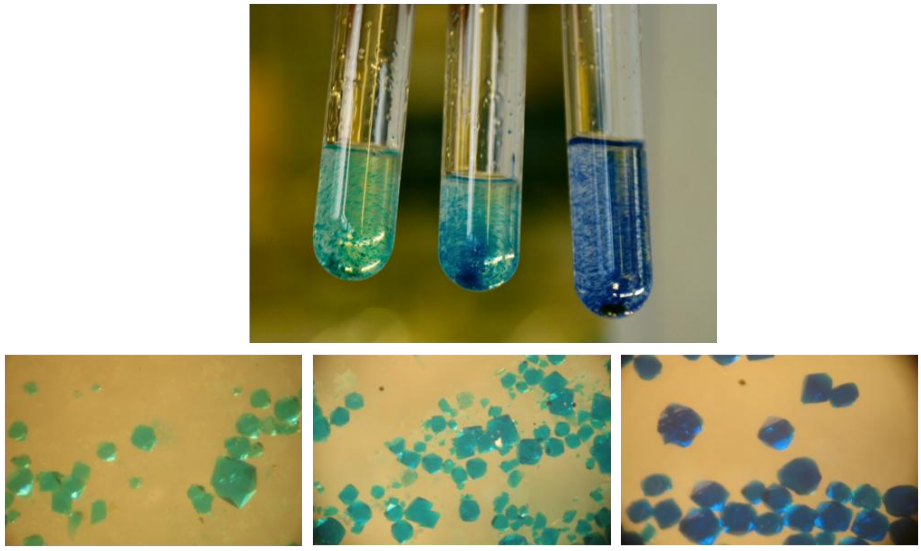

Fig. 16 Color differences between PCN6mix crystals in DMF (left), MeOH (middle) and DCM (right).

2.7.4 Inclusion experiments

Crystalline samples of both H-KUST and PCN6mix for the SC-XRD analysis were prepared by soaking the previously activated crystals in pure nicotine or pure propofol. The system was then left in a sealed vial for nearly 3 weeks at room temperature. Once in contact with the liquid guest, the color of the crystals change from the dark blue characteristic of the activated one to light green, if soaked in nicotine, and dark green, if soaked in propofol (as reported in fig. 17).

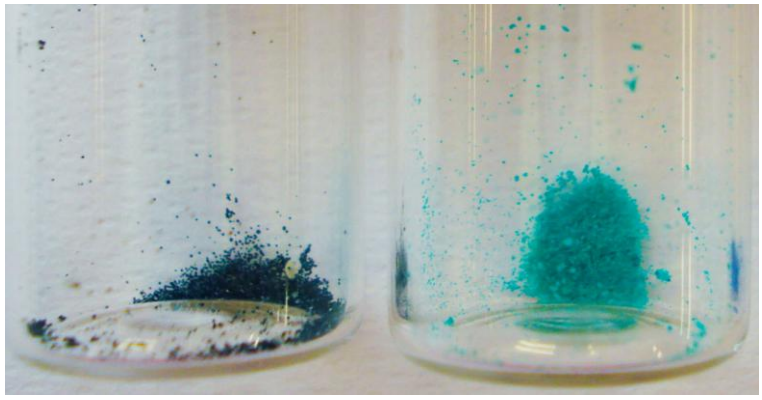

Fig. 17 PCN6mix crystals loaded with guests: propofol (left) and nicotine (right).

After the loading procedure a cleansing step was performed, using DCM, in order to remove potential molecules of the guest adsorbed on the surface of the crystals. This was extremely important for the samples that were used for TGA and mass spectroscopy analysis, in order to properly evaluate the quantity of guest included.

2.7.5 TGA and mass spectrometry analysis on PCN6mix

One of the primary purpose was to confirm the inclusion of the guest in the cavities of the MOF samples. For this reason, mass spectra were collected using electron impact technique and a direct insertion probe (DIP/EI MS). The mass spectrometer used is a Thermo DSQ II with single quadrupole. All the spectra were collected with a ionizing voltage of 70eV.

A rough estimate of the quantity of guest entrapped in the porous material can be calculated performing a thermogravimetric analysis. TGA was performed on PCN6mix@nicotine with a scan rate of 10°C/min from room temperature (25°C) to 400°C, using a TGA 7 Perkin Elmer analyzer.

2.7.6 UV monitoring

In order to have a further evidence of the inclusion of the guest, a monitoring experiment was prepared using the UV-vis spectrophotometer. A solution of the guest with a known molar concentration was kept in contact with a known amount of MOF material. Various aliquots were taken and checked through UV absorbance spectroscopy in order to evaluate the variation in terms of concentration as the time pass by. A specific calibration curve for both nicotine and propofol was built by preparing standard solutions at known concentration of the guest in DCM. Three different experiments were performed and described as follows:

- H-KUST@nicotine in DCM: an initial solution ($2.5 \cdot 10^{-2}$M) of nicotine in anhydrous DCM (50 ml) was prepared and inserted in a flask containing 425 mg (0.7 mmol) of HKUST under N_2 flux. Aliquots of 50 µl of the solution in contact with the MOF have been taken, starting from t_0 (beginning of the experiment) up to t_{10} (after 2 days). The solution samples have been properly diluted 1/100 in order to enter in the range of the calibration curve and UV spectra were collected for each sample.
- H-KUST@propofol in DCM: an initial solution ($2.16 \cdot 10^{-2}$M) of propofol in anhydrous DCM (50 ml) was prepared and inserted in a flask containing 425 mg (0.7 mmol) of HKUST under N_2 flux. Aliquots of 50 µl of the solution in contact with the MOF have been taken, starting from t_0 (beginning of the experiment) up to t_{10} (after 2 days). The solution samples have been properly diluted 1/100 in order to enter in the range of the calibration curve and UV spectra were collected for each sample.
- PCN6mix@nicotine in DCM: an initial solution ($4.98 \cdot 10^{-3}$M) of nicotine in anhydrous DCM (5 ml) was prepared and inserted in a flask along with 6.7 mg () of PCN6mix. Aliquots of 50 µl of the solution in

contact with the MOF have been taken, starting from t_0 (beginning of the experiment) up to t_6 (after 11 days). The solution samples have been properly diluted 1/100 in order to enter in the range of the calibration curve and UV spectra were collected for each sample.

All the UV spectra were collected on a UV-visible Bio Evolution Thermo scientific 260 spectrophotometer and all the concentrations were calculated using the maximum value of absorbance characteristic for every species (nicotine λ_{max} = 263 nm, propofol λ_{max} = 272 nm).

2.7.7 SC-XRD analysis on PCN6mix

Single crystal x-ray diffraction analysis is probably the most powerful tool that we can use to demonstrate the presence, the topological disposition and the amount of a guest inside the cavities of the MOF. Due to the small dimensions of the PCN6mix crystals a standard data collection using a standard sealed tube, with a molybdenum target, x-ray source would not lead to results of sufficiently acceptable quality. For this reason PCN6mix@nicotine and PCN6mix@propofol crystals were analyzed using synchrotron radiation. The experiments were performed at *Elettra Sincrotrone* (Trieste, Italy) on beamline XRD1 at 100 K under nitrogen flux. The source used for the analysis was a NdBFe Multipole Wiggler (Hybrid linear), 4.27 keV with a power of 8.6 kW, a source size FWHM of 2.0 x 0.37 mm (0.7 x 0.2 mm FWHM beam size at sample) and photon flux 10^{12}-10^{13} ph/sec.

3. RESULTS and DISCUSSION: COCRYSTALS

3.1 Thermal analysis on cocrystals

DSC and HSM analysis show interesting results and basic information about the thermal properties of the novel compounds synthesized. Melting points of the cocrystals have been evaluated in order to make a clear and precise comparison with the molecule of interest (APIs or nutraceuticals) generally characterized by low temperature melting points and are summarized in table 3.

Table 3

Cocrystal	Melting point (°C)
Propofol - B1	98
Propofol - PH1	50
AMα	90
AMβ	90
Carvacrol - PH1	40
Nicotine - DOB	68
Nicotine - DITF	54
Nicotine - D1	99
Eu - F1	106

In some specific cases impurities were detected as well as peculiar thermal behaviors.

3.1.1 Nicotine-DITF

Differential scanning calorimetry on nicotine-DITF sample shows a neat peak during first heating run with a maximum at 53.93°C (ΔH = 48.8544 J/g, fig. 18). This endothermic peak is generated by the melting of the cocrystal sample and it has been clearly monitored with HSM analysis (fig. 20). Pic-

tures show the starting sample at room temperature, closed within a glass slide (support) and a covering glass slit, slightly melting as temperature exceeds 50°C and, eventually, reaching complete fusion above 55°C. During the cooling scan neither exothermic nor endothermic peaks appear, as shown in figure 18; and the same absence of interesting phenomena has been inspected with HSM as well. During the cooling phase the melt highly increases its viscosity, above all, below 0°C. As a consequence of this, a broad band in the second heating run of the DSC (fig. 19) is noticeable starting from -22°C up to -16°C and ascribable to a glass transition. Here, the system is characterized by high viscosity and it is not organized in a precise and characteristic crystal form, thus an amorphous phase. A second broad peak, in this case exothermic, with a minimum at 25.73°C (ΔH = 33.1470 J/g) represents the re-crystallization of the cocrystal. In this particular case, HSM and DSC seem to differ on the behavior of the system during the second heating phase. In this particular case, HSM and DSC seem to differ on the behavior of the system during the second heating phase. Pictures collected with HSM technique show a partial re-crystallization of the melt, which leads to the formation of tiny needles crystals (fig. 21). This is probably due to the precipitation of the coformer during the second heating run and this may happen because the system crosses a metastable curve in the 2 phase diagram. The melting of the cocrystal is confirmed by the presence of a third peak in the DSC, endothermic, with a maximum at 53.66°C (ΔH = 46.8482 J/g) and perfectly comparable, both for temperature and for difference of enthalpy, to the melting peak of the first heating. This proves out that the system is thermally reversible and degradation or loss of any components do not occur. The glass transition is a proof that the cocrystal is not able to reform during the cooling phase with such a specific ramp, probably too fast for the two components (API and coformer) to re-organize in a crystalline structure, and needs higher temperature in order to make a phase transition towards a crystal phase. It is important to remind that nicotine is characterized by glass transition which occurs below -79°C, therefore it is a definitely difficult molecule to crystallize, probably for the presence of a highly mobile structure characterized by free rotating rings (pyridinic and pyrrolidinic) which generate high free volume in the solid phase.

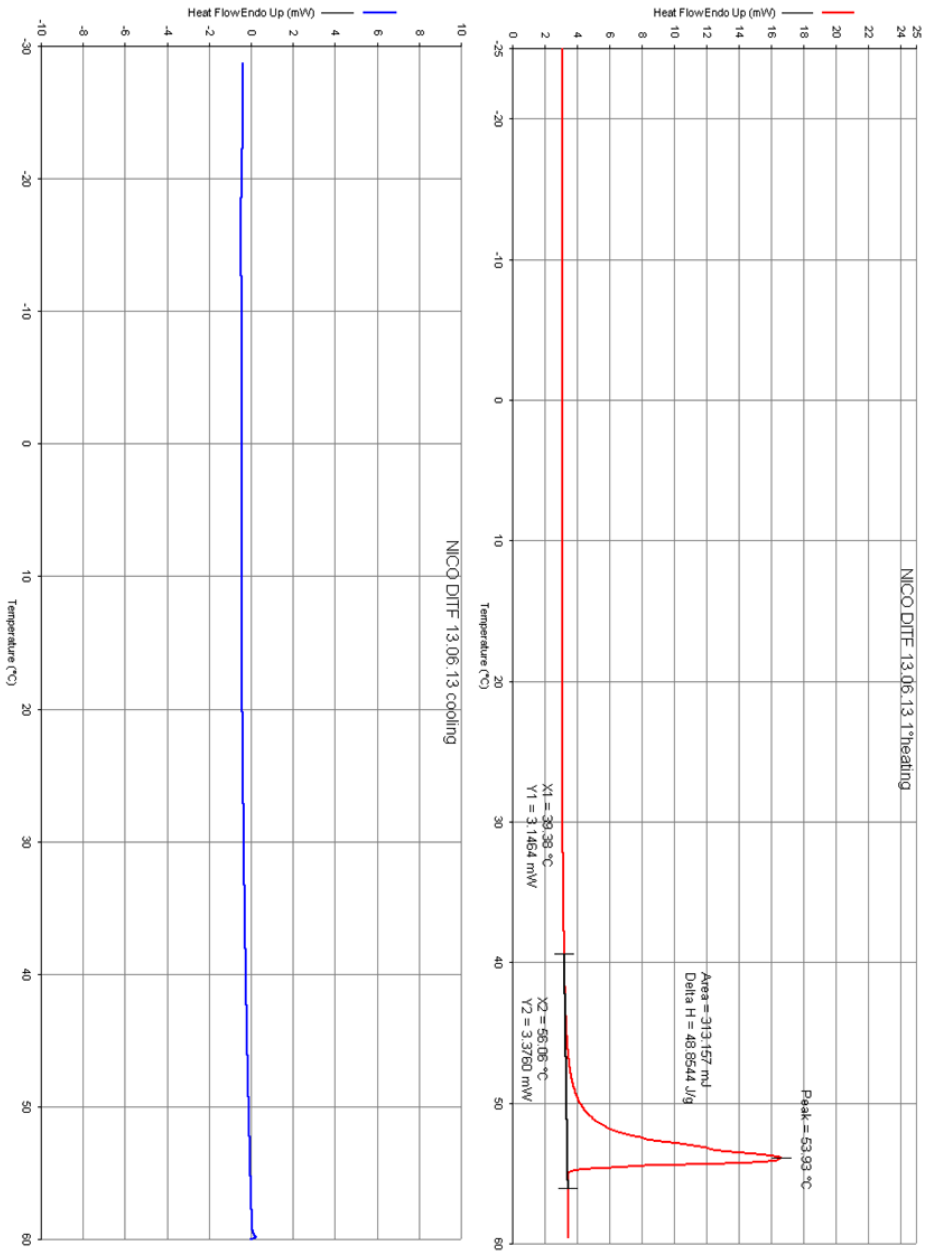

Fig. 18 DSC analysis on nicotine-DITF cocrystal. First heating is reported on the right, cooling on the left.

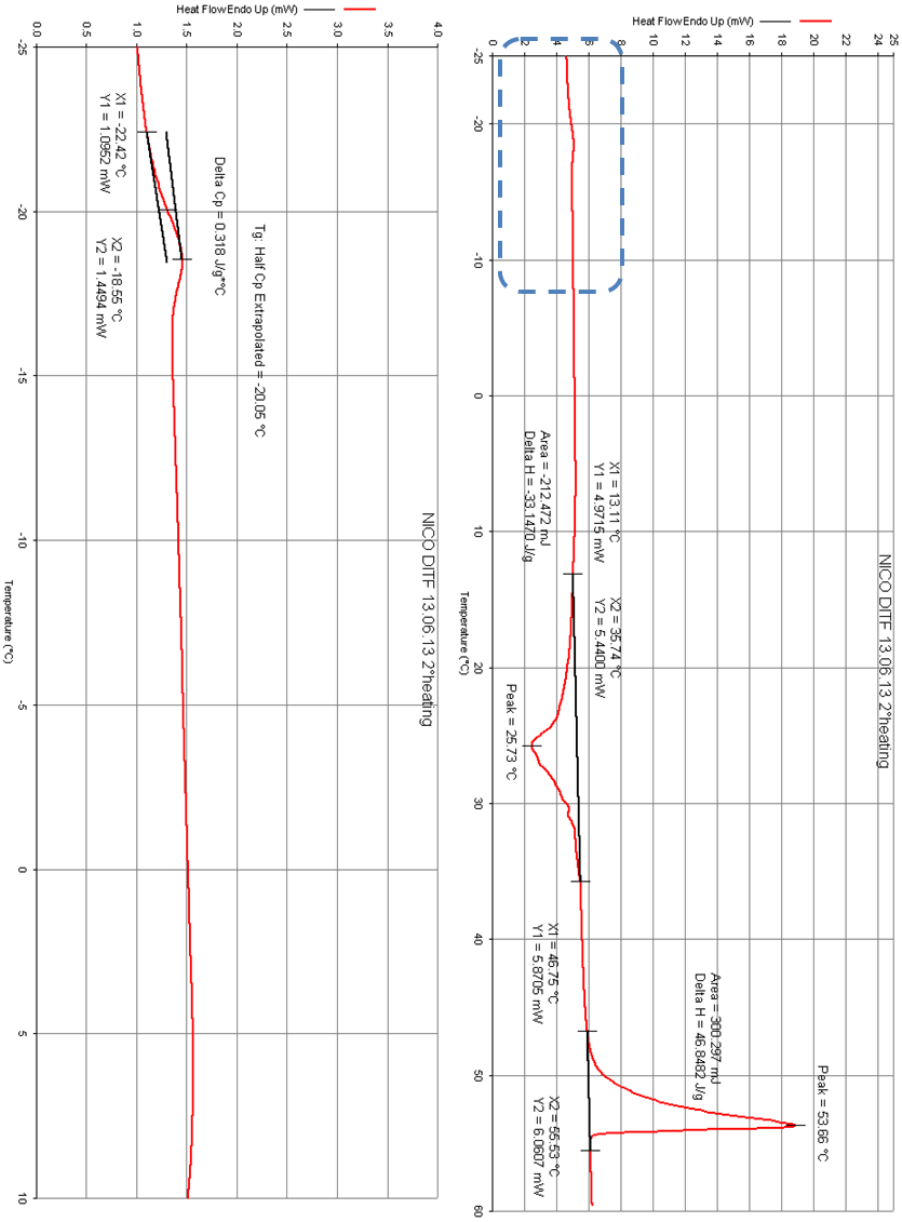

Fig. 19 DSC analysis on nicotine-DITF cocrystal, second heating. On the left is reported a zoom on the glass transition zone.

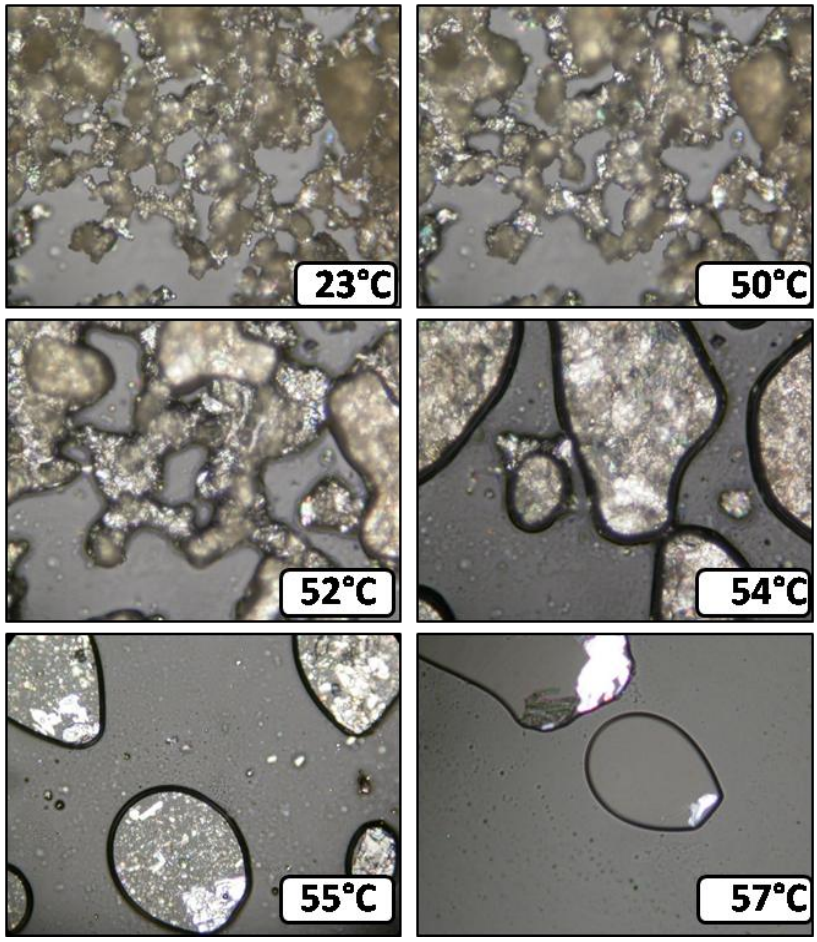

Fig. 20 First heating: HSM analysis on nicotine-DITF cocrystal starting from room temperature up to melting point temperature.

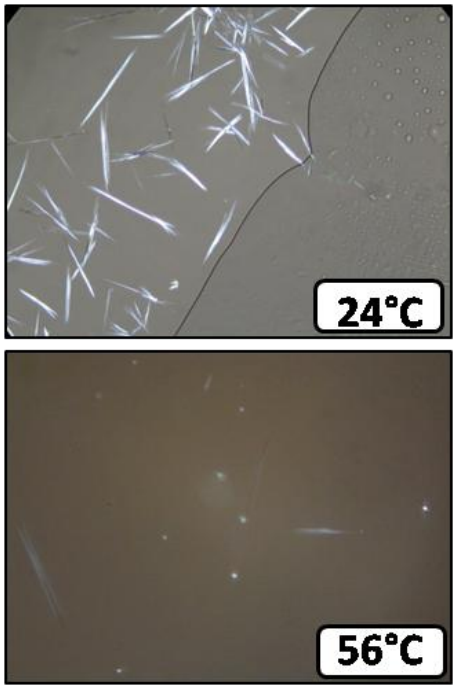

Fig. 21 Second heating: HSM analysis on nicotine-DITF cocrystal starting from room temperature (partial re-crystallization occurs at 24°C) up to melting point temperature (56°C).

3.1.2 Nicotine-DOB

Only DSC analysis was performed on a nicotine-DOB cocrystal sample following the typical first heating - cooling - second heating experiment. During the first heating an endothermic peak with a maximum at 68.11°C (ΔH = 34.0653 J/g) is visible and ascribable to melting of the cocrystal (fig. 22). The cooling run is characterized by a progressive decrease in heat flow from 80°C down to -20°C but no relevant peaks are present. During the second heating (fig. 23), it is noticeable the presence of a broad band ranging from -10°C to -5°C with a maximum at -8°C. This is a glass transition which is similar to what has been reported for nicotine-DITF cocrystal. Nicotine may be responsible of the glass transition in both cocrystals and its characteristic high mobility, due to pyridinic/pyrrolidinic rings free to rotate, may affect the system, avoiding the re-crystallization during the cooling phase.

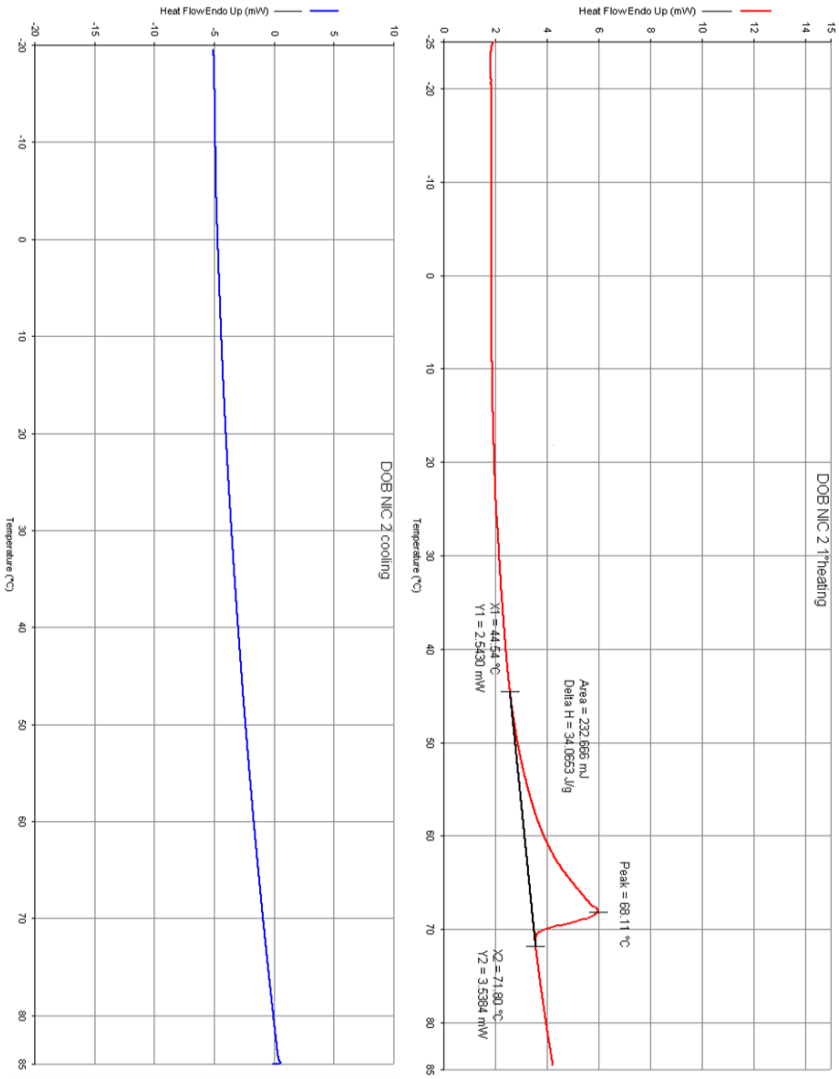

Fig. 22 DSC analysis on nicotine-DOB cocrystal, first heating is reported on the right, cooling on the left.

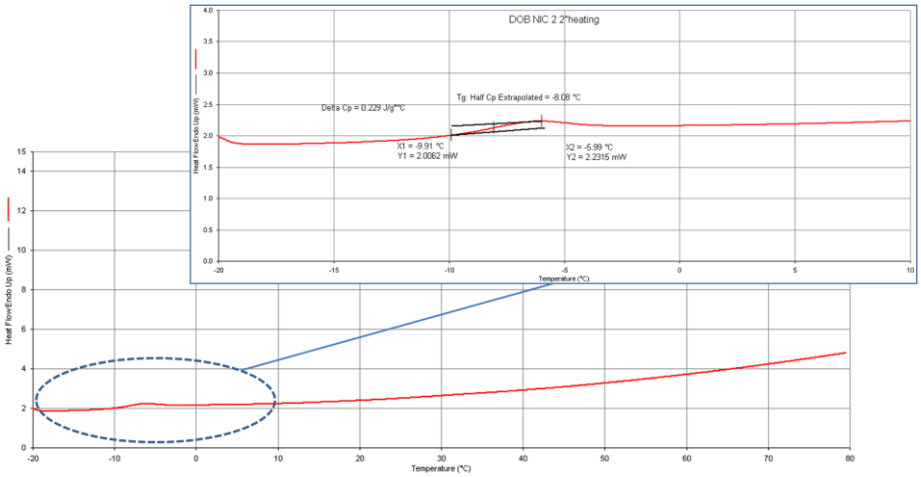

Fig. 23 DSC analysis on nicotine-DOB cocrystal, second heating is reported with a zoomed area.

3.1.3 Propofol-B1

Differential scanning calorimetry on propofol-B1 sample shows a neat endothermic peak during first heating run with a maximum at 97.96°C (ΔH = 90.5627 J/g) ascribable to the melting of the cocrystal (fig. 24). HSM pictures are in agreement with DSC data and are reported in fig. 25: starting from room temperature (23°C), a large amount of small crystals is visible and they eventually completely melt once 100°C is reached. During the cooling phase a unique neat peak with a minimum at 88.35°C (ΔH = -75.5774 J/g) is visible. This is an exothermic signal related to the re-crystallization of the cocrystal as it is confirmed by the pictures collected with HSM analysis where, at around 84°C, crystals start to form from the melt. Finally, as it is reported in fig. 26, second heating coincides with first heating run: a neat endothermic peak with a maximum at 97.47°C (ΔH = 73.6474 J/g) which stands for the fusion of the cocrystal. Enthalpy differences of the three phenomena are comparable and the melting point maximum temperatures in the first heating and second heating are identical, indicating the system is completely thermally reversible, no degradation occurs and the cocrystal can be obtained directly from cooling the melting.

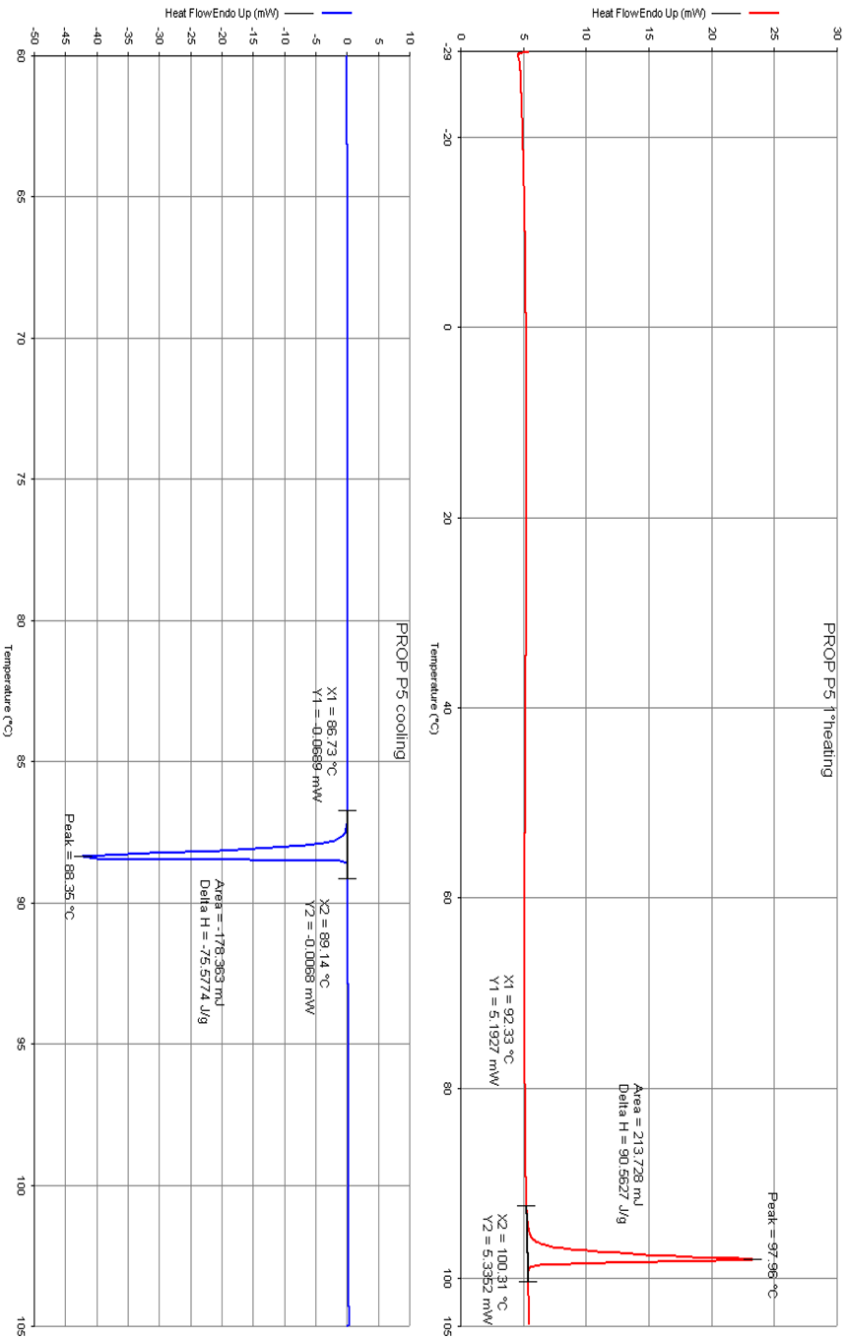

Fig. 24 DSC analysis on propofol-B1 cocrystal, first heating is reported on the right, cooling on the left.

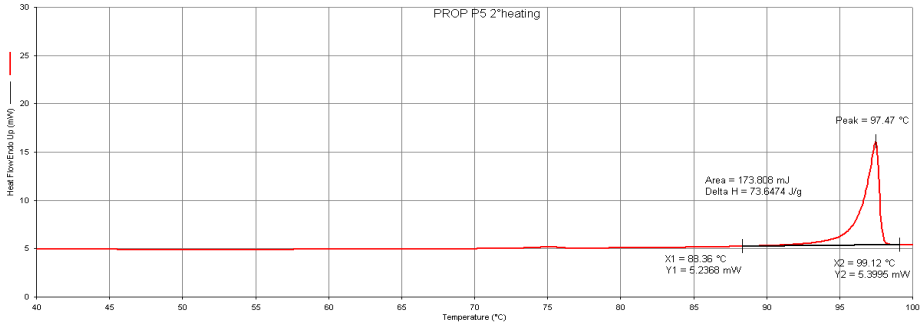

Fig. 25 DSC analysis on propofol-B1 cocrystal, only second heating is reported.

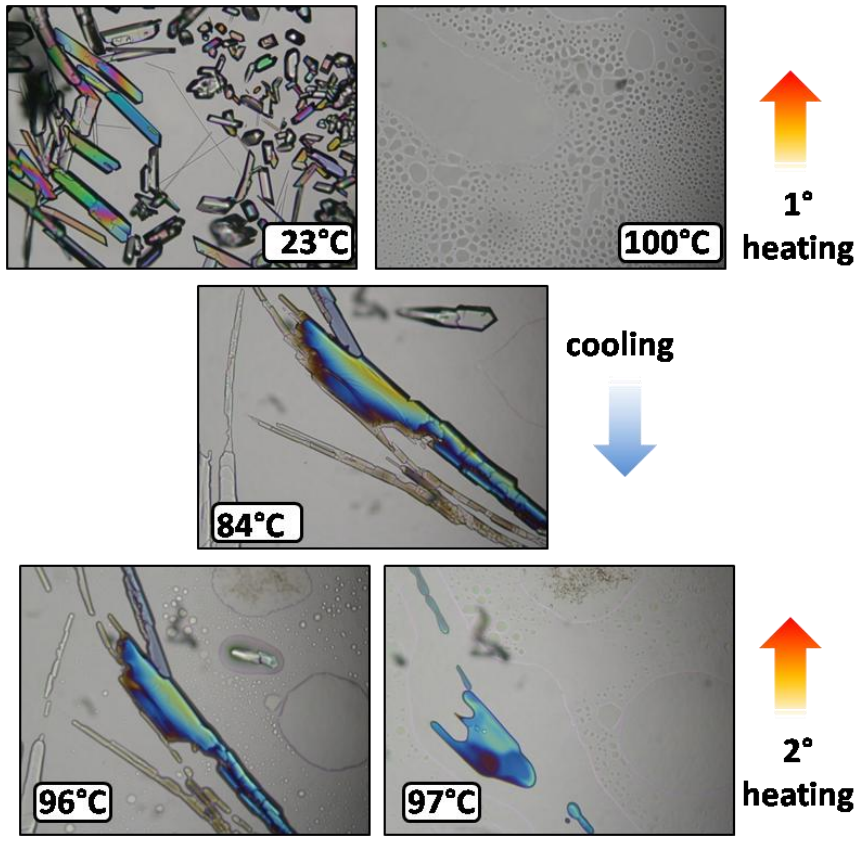

Fig. 26 HSM analysis on propofol-B1 cocrystal.

3.1.4 Propofol-PH1

Differential scanning calorimetry analysis was performed on propofol-PH1 sample and it shows an endothermic peak during first heating run with a maximum at 48.92°C (ΔH = 83.4603 J/g) related with the melting of the co-crystal. Two exothermic peaks are visible in the cooling curve reported in fig. 27 with minimum values at 29.77°C (ΔH = -43.4645 J/g) and -14.71°C (ΔH = -13.9487 J/g). Both represent re-crystallization, the first peak (at 29.77°C) stands for the re-crystallization of the cocrystal while the second, below 0°C, stands for the re-crystallization of a small excess of propofol. Cocrystallization experiments, in fact, had been intentionally performed with a slightly excess of API. The characteristic temperature of these transitions does not identically match the temperature at which these species melt and this can be easily explained referring to thermal hysteresis. During the second heating (fig. 28) run two endothermic peaks occur which are strictly comparable to those present in the cooling run. The endothermic peak with a maximum at 16.49°C (ΔH = 15.2920 J/g) is ascribable to the melting of the previously re-crystallized propofol and the enthalpy difference is strictly similar to the one that characterizes the correspondent peak, while the endothermic peak with a maximum at 48.67°C (ΔH = 47.6929 J/g) is ascribable to the melting of the cocrystal and it is comparable to the exothermic peak with a maximum at 29.77°C in the cooling run. The presence of an excess of API, with respect to the 2:1 molar ratio, in the cocrystal is proven by the presence of characteristic peaks. The cocrystal thermal behavior is completely reversible and reproducible, as it is demonstrated by various DSC analyses performed on different samples from different batches of propofol-PH1.

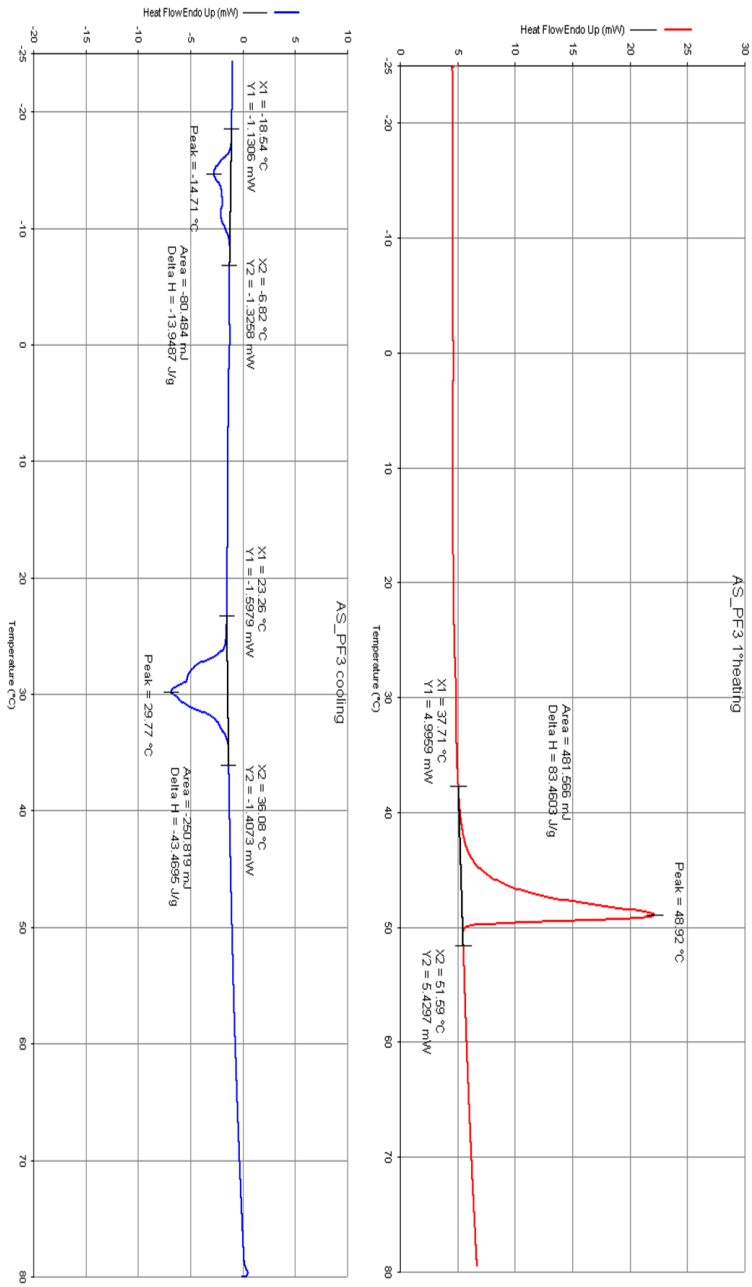

Fig. 27 DSC analysis on propofol-PH1 cocrystal, first heating on the right, cooling on the left.

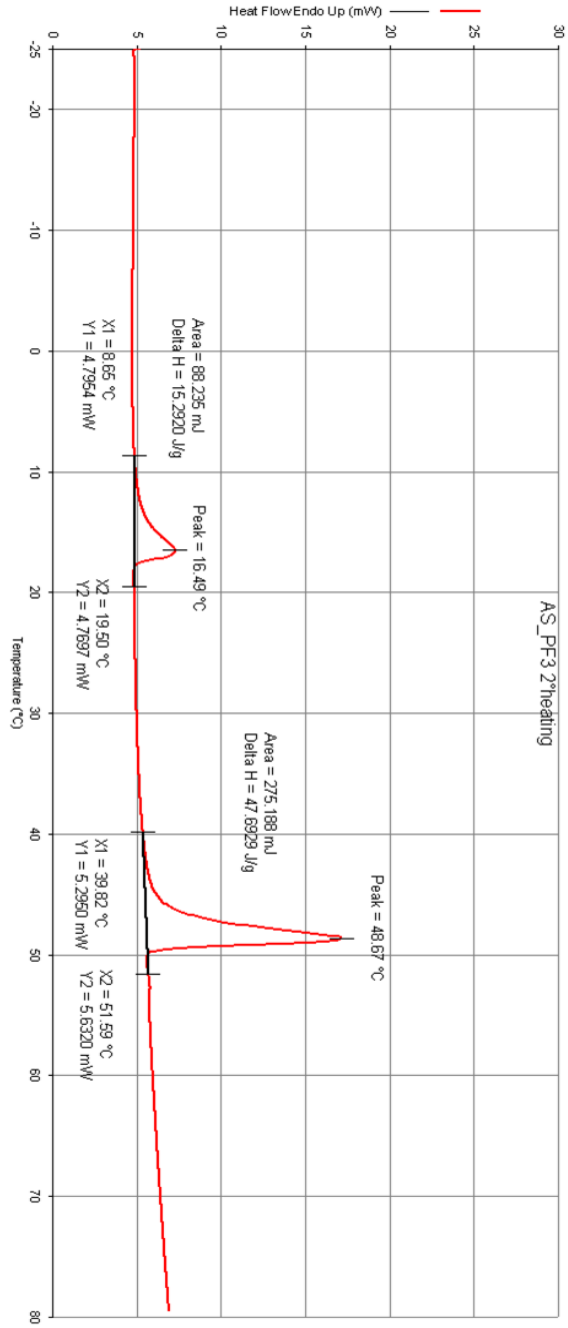

Fig. 28 DSC analysis on propofol-PH1 cocrystal, second heating.

3.1.5 EU-F1

Differential scanning calorimetry analysis was performed on EU-F1 sample demonstrating that 3 different phenomena happen during the first heating run. As reported in fig. 29, 2 endothermic peaks with maximum at 106.29°C (ΔH = 50.5909 J/g) and 109.87°C (ΔH = 35.5956 J/g) and 1 exothermic peak with minimum at 108.08°C are visible. In order to clearly understand what kind of phase transitions were happening we performed HSM analysis on EU-F1 sample and the pictures that have been collected are reported in fig. 31a. Starting from room temperature tiny crystals are clearly visible and stable up to 107°C where, holding the temperature for 5 minutes, only a portion of the solid melt. This is probably the melting of the cocrystal that corresponds to the first endothermic peak. The exothermic peak is ascribable to the precipitation of F1 and the second endothermic peak is related to the complete melting of the solid F1 (as visible from HSM analysis). The cooling run in the DSC analysis does not present any evident peak indicating that no particular transition occurs. Differently from DSC, HSM analysis shows a very slow and progressive re-crystallization that cover a wide range of temperature from 80°C down to room temperature. This phenomenon is essential to explain the endothermic peak visible in the second heating run of the DSC analysis. With a maximum at 109.19°C and ΔH = 52.3817 J/g, it is comparable to the second endothermic peak of the first heating run and it is evidently the melting of the coformer (F1). A look at the pictures taken during HSM analysis confirms the stability of the solid in the temperature window 90°-106°C, holding 5 minutes, and the fusion which starts at 107°C and goes to completion. It is presumable that in the cooling run of the DSC, re-crystallization of F1 occurred too slowly in a very wide range of temperature, resulting in an extremely weak and undetectable heat flow. This particular binary system can be described using a two phase diagram for a non-congruent system as the one reported in fig. 31b. Starting from the cocrystal molar ratio (in the figure, a generic A-S system, where A is the coformer and S the drug) and increasing temperature (moving towards the red arrow) it is possible to cross the underneath cocrystal curve and observe its melting. As temperature increase, the coformer precipitates until the coformer curve is crossed, at that point the coformer melts[98].

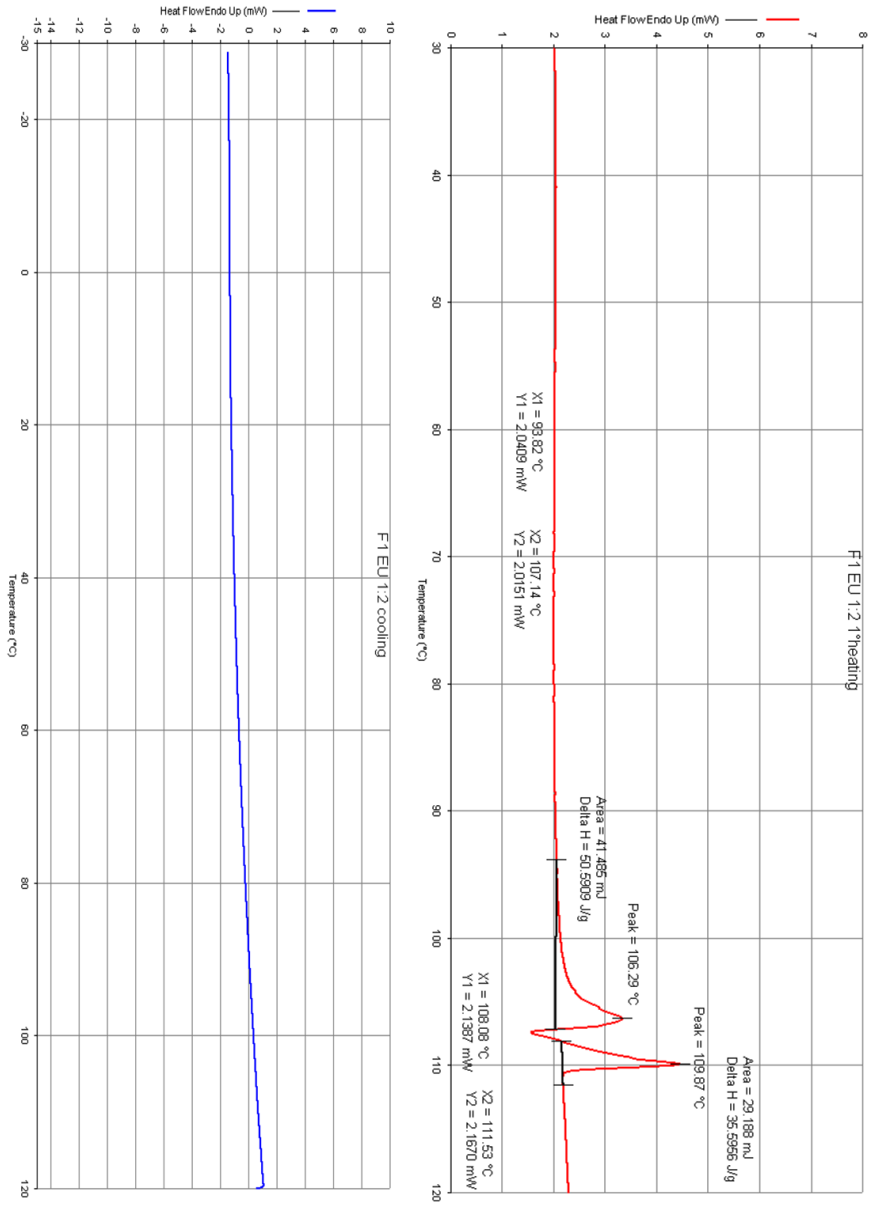

Fig. 29 DSC analysis on EU-F1 cocrystal, first heating on the right, cooling on the left.

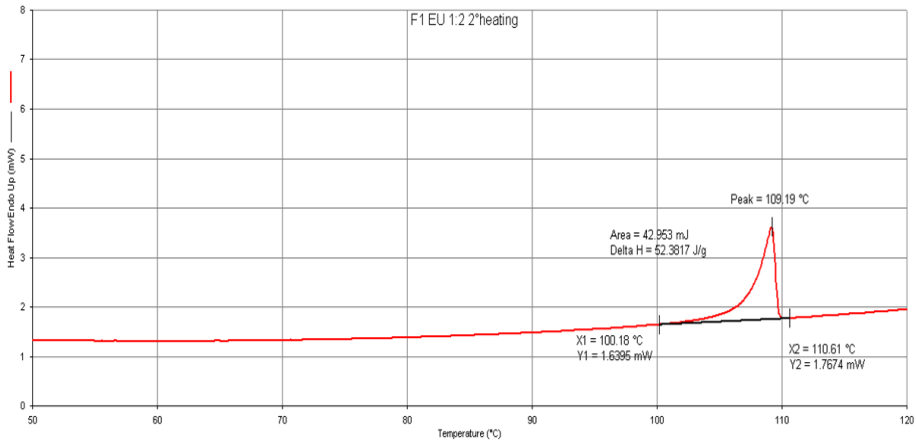

Fig. 30 DSC analysis on EU-F1 cocrystal, second heating.

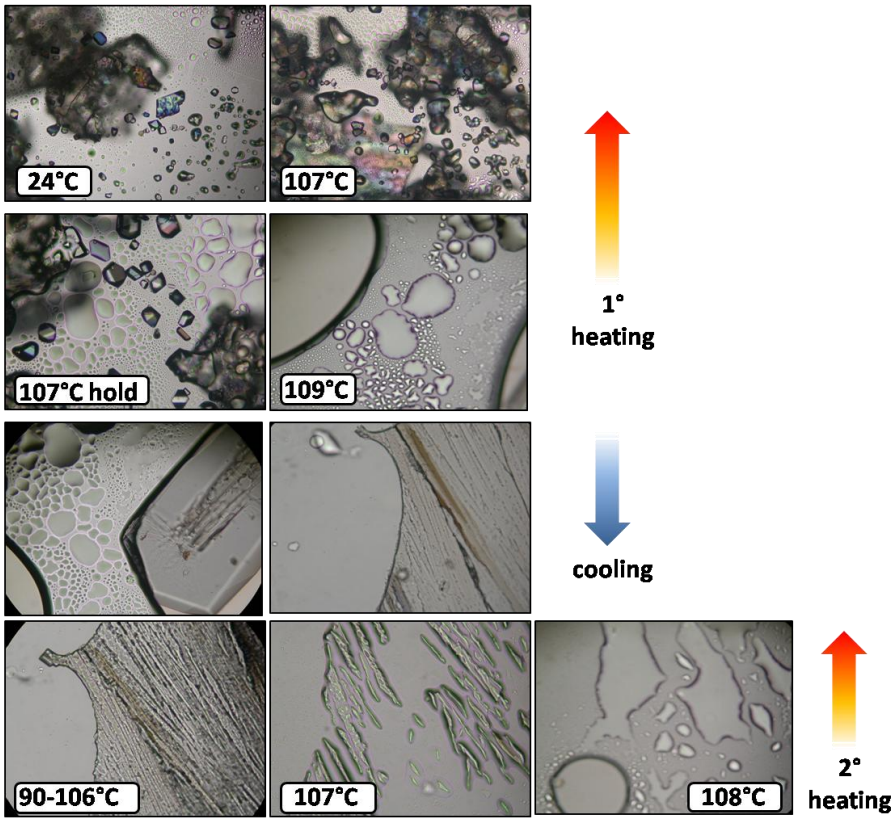

Fig. 31a HSM analysis on EU-F1 sample.

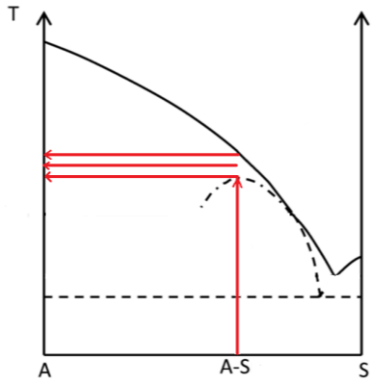

Fig. 31b Proposed 2 phase diagram for a generic non-congruent system A-S.

3.2 Solubility properties and phase diagrams

A deep and precise evaluation of solubility properties was carried on for propofol-B1 cocrystal in water in the laboratories of the College of Pharmacy (Ann Arbor). Experimental efforts, consultation with prof. N. Rodriguez-Hornedo and later considerations allowed to define more precisely the behavior of the system and to draw a clear ternary phase diagram which contains all the information for a specific solid cocrystal dissolving in a liquid phase.

3.2.1 HPLC measurements of slurry experiments

Concentrations of propofol and B1 in water were determined through HPLC technique and reported in table 4. We chose chromatographic method in order to separate API and coformer and to easily detect them with UV-vis spectrophotometer. Propofol has a maximum of absorbance at λ = 220 nm and B1 at λ = 241 nm and this implies some difficulties in analyzing both API and coformer in solution without a previous separation.

Concentration values collected in this way are of primary importance in evaluating critical points of the ternary phase diagram. *Slu4 and Slu5* concentrations, for example, stand for the solubility limit of, respectively, B1 in water and B1 in pure propofol. A clear and reasoned comparison of *Slu1, Slu2* and

Slu3 results can point out interesting considerations about the system. Both of them are water based solution containing an amount of cocrystal over its saturation concentration. In the specific case of *Slu2* an excess of B1 has been added and for *Slu3,* an excess of propofol. At first glance, *Slu1* does not contain propofol and B1 in solution in the same molar ratio as the solid co-crystal (2:1): propofol concentration is 1000 times lower than expected. These data are effectively strange and are just a hint of the complexity of the whole system. *Slu2* reports a higher concentration of B1, accordingly to the what expected when the slurry was prepared adding solid B1 and *Slu3* reports the same concentration of B1 as the standard slurry experiment *Slu1.* All the concentration data of propofol in *Slu1, Slu2, Slu3* are lower than expected, significantly not different, thus equivalent. It is therefore reasonable to accept propofol concentration values as constant, differing only for small inconsistent amount, probably due to the instrument detection limit and strongly affected by experimental errors. This specific concentration of the API seems to be the intrinsic solubility limit of the drug in water.

Table 4

	Propofol conc. (M)	**B1 conc. (M)**	**K_{sp}**
Slu1	$(6.0 \pm 0.1)\cdot10^{-5}$	$(1.03 \pm 0.01)\cdot10^{-2}$	$(37.08 \pm 1.60)\cdot10^{-12}$
	$(5.8 \pm 0.1)\cdot10^{-5}$	$(1.00 \pm 0.01)\cdot10^{-2}$	$(33.64 \pm 1.50)\cdot10^{-12}$
Slu2	$(5.47 \pm 0.06)\cdot10^{-5}$	$(2.42 \pm 0.02)\cdot10^{-2}$	$(72.40 \pm 2.19)\cdot10^{-12}$
	$(4.61 \pm 0.19)\cdot10^{-5}$	$(2.57 \pm 0.02)\cdot10^{-2}$	$(54.62 \pm 4.93)\cdot10^{-12}$
Slu3	$(3.94 \pm 0.02)\cdot10^{-5}$	$(1.09 \pm 0.01)\cdot10^{-2}$	$(16.92 \pm 0.33)\cdot10^{-12}$
Slu4	-	$(2.80 \pm 0.01)\cdot10^{-2}$	-
Slu5	-	$(6.60 \pm 0.01)\cdot10^{-2}$	-

3.2.2 Phase diagrams

In the case of propofol and B1 in H_2O, there are 4 components (cocrystal, API, coformer, solvent) 3 of which mutually independent (API, coformer and solvent). Considering a system in isothermal and isobaric conditions, it is possible to ignore 2 degrees of freedom, so external parameters lower to zero.

Gibbs rule of phases for the analyzed system results, therefore:

$$f_T = 3 - p$$

It is noticeable how variance (f_T) simply relies on the number of phases of the system, so that every characteristic point of the diagram has a specific variance. Eutectic points (C, E), for instance, are distinguished for a variance value of 0; this means there are no intensive variables that can be changed independently without disturbing the phases in equilibrium at the eutectic point. Focusing on the curve that connects points B-C, the curve that connects points C-E and the curve that connects points D-E, they are all characterized by variance values of 1, hence the system is forced to rely on a curve with only one degree of freedom. Eventually, Zones 4 and 7 possess two degrees of freedom and are geometrically represented as surfaces. Stoichiometric line for the 2:1 cocrystal is reported as a green dotted line which links point F to the solvent vertex.

Table 5

Variance f_T	Phases	Description
2	1	Zone 4: pure propofol (API) as a homogeneous liquid phase whose composition varies in the area. Zone 7: pure water (solvent) as a homogeneous liquid phase whose composition varies in the area.
1	2	Zone 1: pure propofol in equilibrium with liquid (water containing API whose composition changes along the B-C curve). Zone 2: pure solid cocrystal in equilibrium with liquid

		(water containing API and coformer in a variable composition that changes along the C-Ecurve). Zone 3: pure B1 (coformer) in equilibrium with liquid (water containing coformer whose composition changes along the D-E curve). Zone 8: pure solid cocrystal in equilibrium with liquid propofol (API) containing B1 and water.
0	3	Zone 5: pure solid cocrystal and pure propofol (API) are in equilibrium with a fixed liquid composition (eutectic point C). Zone 6: pure solid cocrystal and pure solid B1 in equilibrium with a fixed liquid composition (eutectic point E).

Table 6 Molar fractions at a specific point of the ternary phase diagram.

Point	Propofol	B1	water
A	0.957	-	4.3E-02
B	3.1E-06	-	0.9999969
C	1.1E-06	1.801E-04	0.9998169
D	-	5.612E-04	0.9994445
E	0.9E-06	4.541E-04	0.9995450
F	0.667	0.333	-
G	0.988	1.2E-02	-

Aliquots were taken at different times, starting from 15 seconds after the setup of the experiment up to 28 hours later, from a slurry containing co-crystal propofol-B1 in water. Experimental analysis showed an anomalous behavior: while propofol concentration remained the same over time, B1

concentration increased over 100 times with respect to the starting concentration, reaching a *plateau* after 28 hours. It is evident that the predicted 2:1 ratio is not respected unless we admit something unusual took place. The peculiarity of this system lies in the presence of a liquid drug which strongly affect the system's behavior: not only is of primary importance to properly consider the equilibria established between drug and coformer with respect to the solvent in the analyzed system, but also to deal with the equilibrium that implicates the liquid drug and the coformer.

Table 7 Variation of concentration over time. Time is reported after the preparation of the slurry experiments.

Slurry duration	B1 conc. (M)	Propofol conc. (M)
15 s	2.46E-05	3.47E-05
60 s	2.64E-05	No data
3 min	5.14E-05	No data
10 min	2.54E-04	3.46E-05
30 min	7.67E-04	3.97E-05
3 h 30 min	1.92E-03	2.86E-05
6 h	2.18E-03	3.16E-05
12 h	2.37E-03	3.37E-05
28 h	2.54E-03	3.63E-05

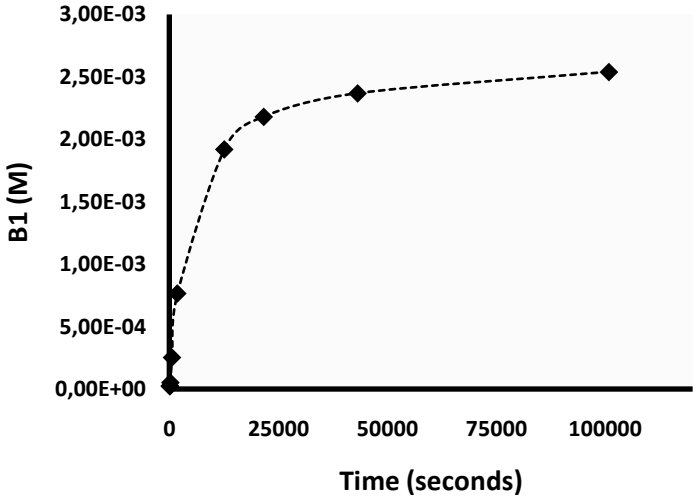

Fig. 32 Plot of the variation of concentration overtime of B1 in water.

The equilibrium reactions that shall be taken into account when dealing with liquid-solid-solvent systems are much more complicated with respect to a classic solid-solid-solvent system and are summarized in fig. 33. The most important difference is the presence of a second solubility constant which rules the equilibrium between solid coformer and liquid API and that is not present when the API is a solid compound in experimental conditions. Moreover, it is of paramount importance to consider the reciprocal solubility of API and solvent and their miscibility in order to notice and evaluate the formation of different liquid phases in equilibrium. There is not any previous ternary phase diagram report in literature for a cocrystal whose components are solid and liquid and this represents a definitely strong tool to schematize the coexistence of the different phases at equilibrium.

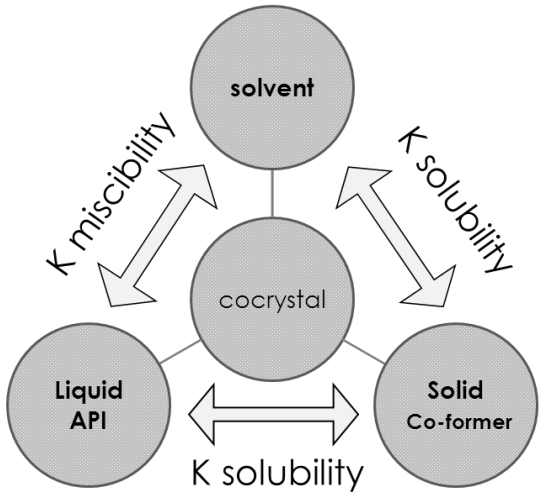

Fig. 33 Diagram of the components and reciprocal equilibria implied in the system.

In the specific case of study, B1 is highly soluble in propofol while has clear poor solubility in water as well as propofol. The anomalous behavior, previously reported, might be ascribed to the progressive separation of propofol from water solution, leading to the formation of a third phase in equilibrium with the others: pure solid cocrystal, in equilibrium with pure propofol, in equilibrium with a fixed liquid composition whose composition is fixed at eutectic point C.

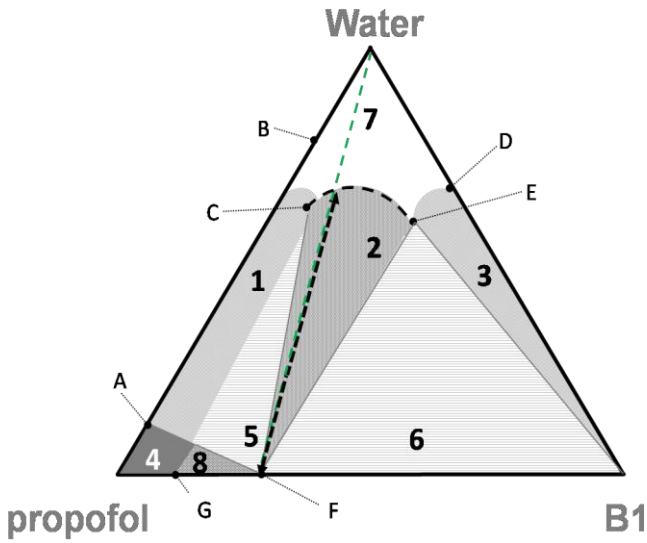

Fig. 34 Fictional ternary phase diagram reporting a congruently dissolving system: cocrystal propofol-B1 in water.

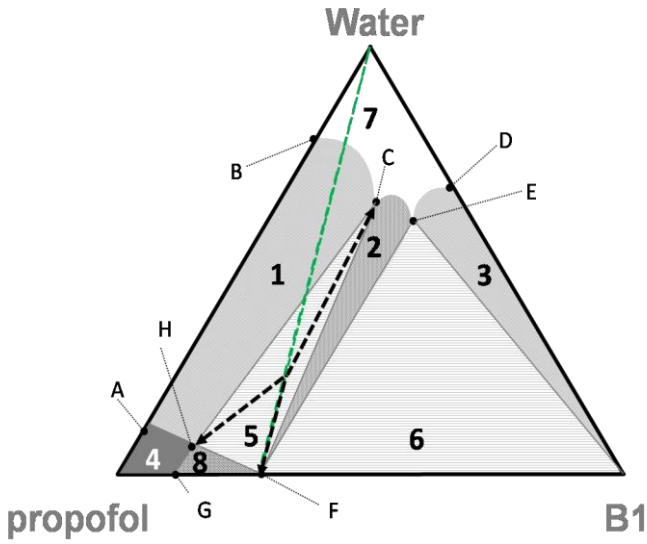

Fig. 35 Ternary phase diagram reporting a non-congruently dissolving system: cocrystal propofol-B1 in water.

Identifying and correctly distinguishing congruent dissolution from non-congruent dissolution is of primary importance. For congruently dissolving systems (fig. 34), addition of solvent to the solid cocrystal, which means moving towards the F-Water green dashed line, shifts to zone n. 2, which is

characterized by presence of 2 phases: solid cocrystal (point F) in equilibrium with a liquid phase whose composition varies along the C-E curve. For non-congruently dissolving systems (fig. 35), addition of solvent to the solid cocrystal shifts to zone n. 5 instead of zone n. 2; obvious implications are the presence of 3 different phases: solid cocrystal (point F) in equilibrium with liquid phase, whose composition is fixed at eutectic composition (point C), in equilibrium with liquid API containing coformer and water (point H). Direct experimental consequence of this behavior is expressed by detection of a higher concentration of B1 in the slurry as the system never crosses the stable solubility curve C-E, therefore it drifts apart from the F-Water green dashed line towards the eutectic point C, as shown by the black dotted arrow. The main issue that affects non-congruent systems is the impossibility to obtain the cocrystal from evaporation of the solvent in which the system is not congruent: starting from the solvent vertex and moving towards point F along the green dotted line (which means adding solid cocrystal to the solvent), the first zone to cross is zone n. 1 where the components of the cocrystal separate and it is evident that zone n. 2, where solid cocrystal is stable, will never be crossed in this specific system.

Eutectic points can be reached and therefore discovered preparing the slurries and altering the standard equilibrium condition in order to move to a different zone in the ternary phase diagram. *Slu*1 experiment is located within zone n. 5 (as reported in fig. 35) and molar concentrations of propofol and B1 (reported in table 6) define the eutectic point C. Adding B1 to the slurry as it was done in *Slu*2 experiment means moving toward the B1 vertex of the triangle (see fig. 36): starting from zone n. 5 it is possible to reach zone n. 6. This is confirmed by presence of B1 phase along with cocrystal phase in powder diffraction pattern of the solid phase filtered from the slurry and the resulting molar concentration are ascribable to eutectic point E. *Slu*3 represents a movement toward propofol vertex (see fig. 36), starting from the zone n. 5. In that case it was not possible to reach zone n. 1 simply adding a small amount of propofol to the slurry, hence the system still reach equilibrium at eutectic point C and this has been confirmed by molar concentration values that are comparable to that of *Slu*1. In order to overcome zone n. 5 and reach zone n. 1 it is necessary to add a huge amount of propofol capable of solubilizing the whole cocrystal powders.

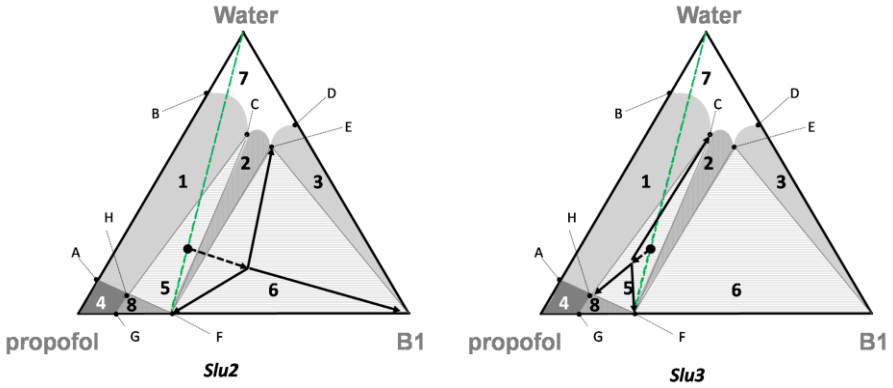

Fig. 36 Ternary phase diagrams of propofol-B1 (out of scale).

The system under study strongly differs from typical solid-solid-solvent ternary phase diagrams, not only for the fact that it is a non-congruently dissolving system but also because it is characterized by extremely low solvent solubility. For this reason the graphs in fig. 35 and 36 are reported out of scale for having a clear and comprehensive plot in order to visually analyze all the phases of the diagram. Using ProSim Ternary plot software it was possible to effectively plot the proper diagram that is shown in fig. 38. Two zoomed areas are reported as well, in order to facilitate the visualization of the boards of the phases near the apices. Zone n. 7 is barely visible because both propofol and B1 are extremely poorly soluble in water. Only two major phases seem to rule the ternary phase diagram: the 2 zone with a variance value of zero and 3 phases in equilibrium. These are zone n. 5 and zone n. 6, respectively the zone characterized by pure solid cocrystal and pure propofol (API) which are in equilibrium with a fixed liquid composition (eutectic point C) and the zone characterized by pure solid cocrystal and pure solid B1 in equilibrium with a fixed liquid composition (eutectic point E). It is pretty understandable why adding B1 or propofol to the slurries containing cocrystal moves the system towards one zone or the other, making extremely difficult to cross other zones which are extremely thin, small and located at the very end of the edges of the diagram.

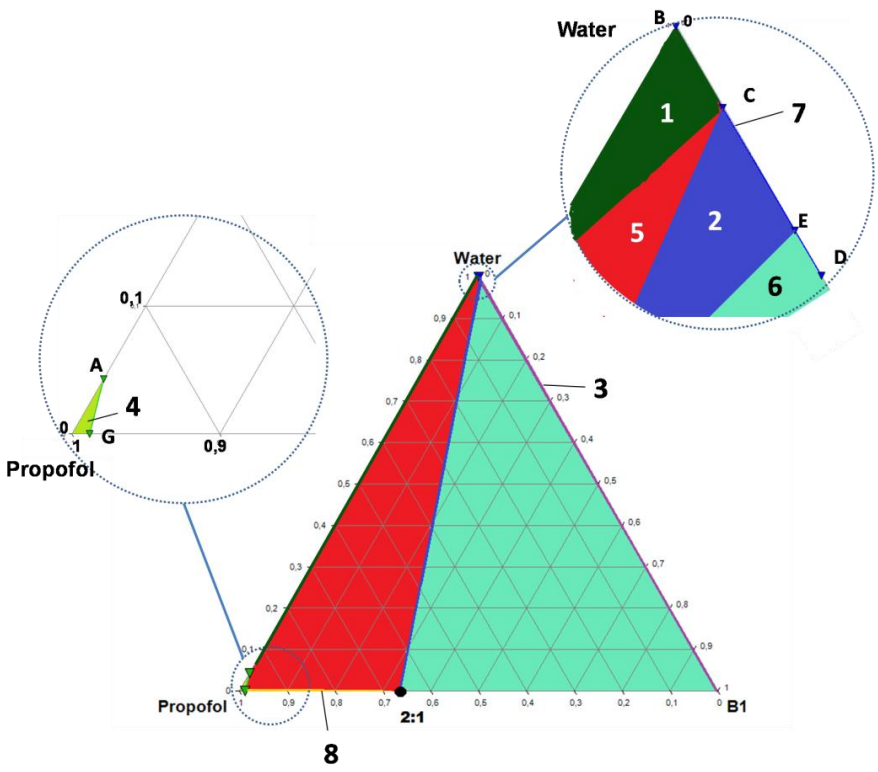

Fig. 38 Ternary phase diagrams of propofol-B1.

3.2.3 K_{sp} calculation and plot

Equilibrium of an API (A) and a coformer (B) which give a cocrystal, may be represented by the following reaction:

(1) $$A_aB_{b\,(s)} \rightleftharpoons aA_{(aq)} + bB_{(aq)}$$

This constant is analogous to the solubility constant of a salt, defined by the product of ions concentrations.

Consequently, the equilibrium constant for this reaction is given by the thermodynamic activity product of the cocrystal components:

(2) $$K_{eq} = \frac{a_A^a a_B^b}{a_{AB}}$$

The solubility constant, K_{sp}, is the equilibrium constant for a solid compound dissolving in aqueous solution and can be expressed, by approssimating activity to molar concentration, as follows:

(3) $$K_{sp} \simeq [A]^a [B]^b$$

In the specific case of a 2:1 (A:B) ratio cocrystals which dissolves in pure solvent, eq.3 can be written this way:

(4) $$K_{sp} = [A]^2 [B]$$

Considering the propofol-B1 cocrystal it is possible to evaluate K_{sp} if the system is at thermodynamic equilibrium. This condition is necessary and occurs when the system reach eutectic points. Constant solubility has been evaluated considering concentration of both propofol and B1 at eutectic point C in the ternary phase diagram.

There is a specific B1 concentration, called cocrystal transition concentration $[B]_{tr}$[5], at which cocrystal solubility equals propofol solubility. This point plays a key role in establishing the region of thermodynamic stability of cocrystal relative to the other components: here both liquid drug and solid cocrystal are in equilibrium with a solution containing drug and co-former [5][6] and the difference of Gibbs free energy of solid cocrystal and drug are equal to zero. $[B]_{tr}$ is the borderline between two regions with Gibbs free energy that differs from zero: the stability region of the solid cocrystal, beyond $[B]_{tr}$, and stability region of pure drug, below $[B]_{tr}$.

It is possible to reach the cocrystal transition concentration by moving along the green dotted line in fig. 39. This means that the cocrystal starts dissolving in water until the propofol intrinsic solubility is reached (move toward the blue line until it crosses the red horizontal line). At this point propofol separates as liquid phase (follow the green dotted line) until it reaches the intersection with the solubility curve of the cocrystal. At this point the system reaches thermodynamic equilibrium, thus, the eutectic point C. This behavior easily explain why the molar concentration of propofol and B1 are not as expected for a 2:1 ratio system. Eventually it is possible to assert that the cocrystal is more soluble than the API itself in water, although the results confirm that the value is not actually particularly relevant.

For a 2:1 ratio system the cocrystal solubility has been reported [4]:

$$Scc = \sqrt[3]{\frac{K_{sp}}{4}}$$

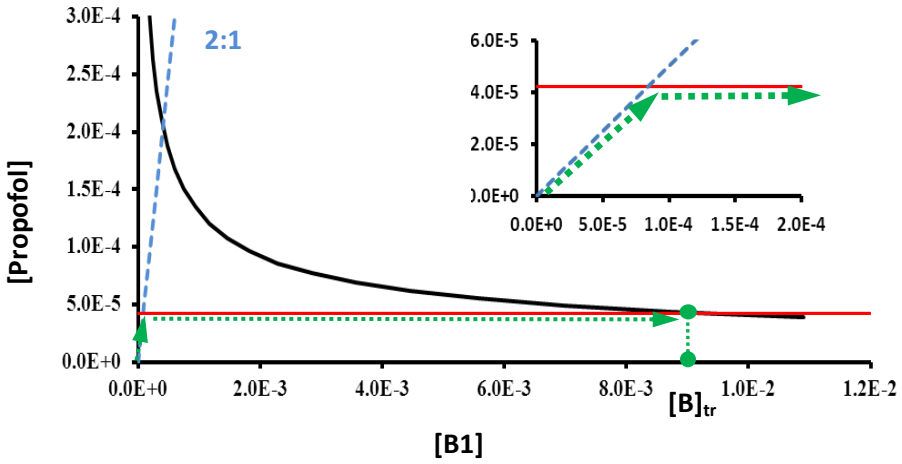

Fig. 39 Phase solubility diagram is represented by black curve, calculated using K_{sp} equation at eutectic point. Blue dashed line stands for the 2:1 ratio of the cocrystal while the red line shows propofol intrinsic solubility in water. Upper right image is a zoom of the low concentration zone of the diagram.

3.3 Crystallographic analysis

3.3.1 Propofol - B1 2:1 and Propofol - PH1 2:1 cocrystals

Intermolecular interactions between API molecule and coformer relies principally on the strong OH···N hydrogen bond between hydroxyl group of propofol and pyridinic nitrogen atom of 4,4'-bipyridine (fig.40). PH1 pyrazinic nitrogen atoms are valid hydrogen bond acceptors hence they interact with hydroxyl groups of propofol giving the same molecular synthon of propofol-B1 cocrystal (fig. 41). In table 8 are reported hydrogen bond distances for a precise comparison between the two structures. Considering propofol-B1 cocrystal, B1 is located in a special position: perfectly within the two pyridinic rings lies an inversion points. This feature is a reflection of the symmetry of the system thus, the two propofol molecules interacting with a B1 molecule are related by symmetry and the H-bonds they form are equal. Contrary to that, two PH1 molecules in propofol-PH1 cocrystal are independent and both appear in the asymmetric unit of the cocrystal, resulting in two distinct hydrogen bonds, not related by symmetry.

The trimeric units that form in both cocrystals are organized in a planar and sequential pattern thanks to CH···π interactions between propofol aromatic ring and B1 (distance C-H···centroid of the aromatic ring: 3.98 Å and 4.09 Å) and PH1 (distance C-H···centroid of the aromatic ring: 3.50 Å), as shown in fig. 42 and 43.

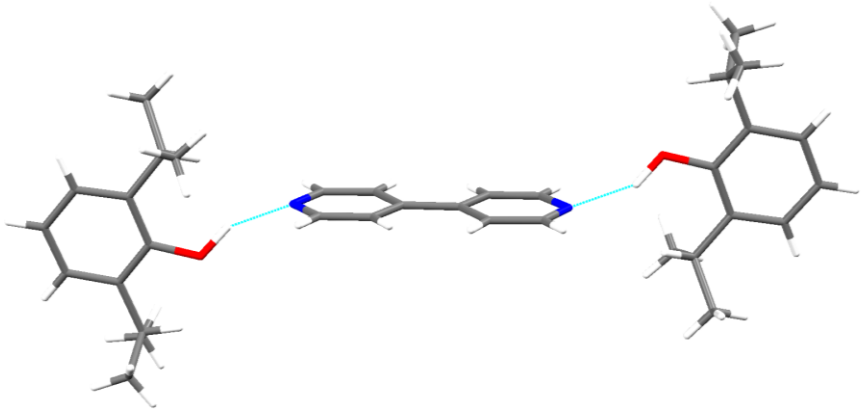

Fig. 40 Hydrogen bonds in propofol-B1 cocrystal.

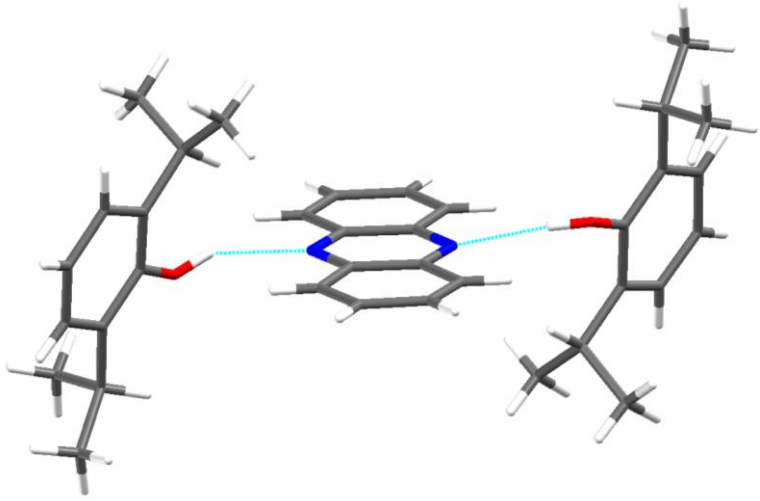

Fig. 41 Hydrogen bonds in propofol-PH1 cocrystal.

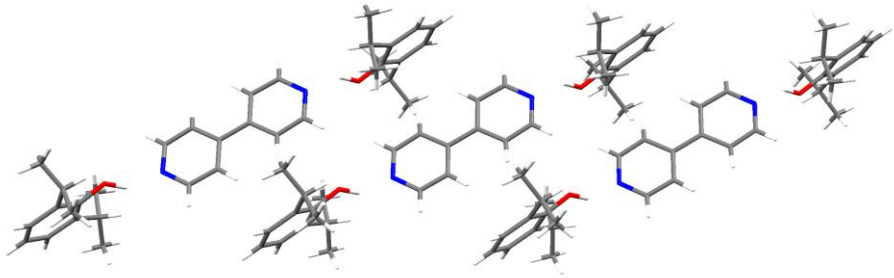

Fig. 42 Assembly of trimeric units in propofol-B1.

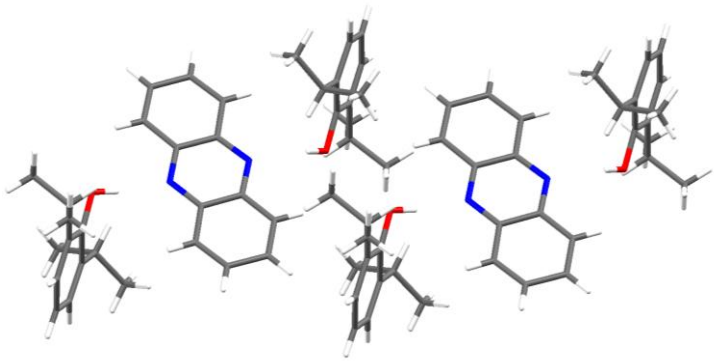

Fig. 43 Assembly of trimeric units in propofol-PH1.

Table 8 Hydrogen bonds geometries.

Cocrystal	D-H···A	H···A (Å)	D···A (Å)	D-H···A (°)
Prop-B1	O(1)- H(10)···N(1)	1.83	2.75	149.5
Prop-PH1	O(1)-H(1)···N(3)	1.98	2.79	169.3
	O(2)- H(2)···N(4)	2.04	2.78	150.0

Assembled trimeric units shown in fig. 42-43 are further organized in alternated strings (fig.44-45). The structural organization differs from one cocrystal respect to the other: in the case of propofol-B1 cocrystal, trimers lay on the same plane following a precise direction, expressed by arrows; sequences of trimers with reverse directions alternate one another repetitively following a herringbone style pattern of hydrogen bonds. Considering propofol-PH1 cocrystal, trimers always point in the same direction, as it is easily noticeable by the orientation of the PH1 molecule, and those located on different columns are also located on different planes twisted of 44.8°.

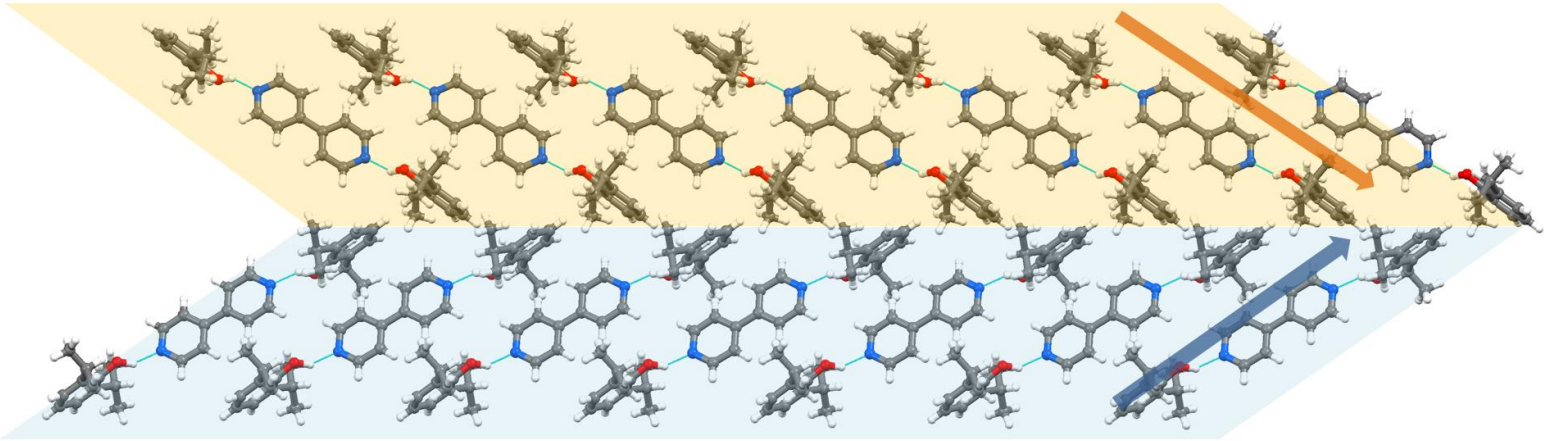

Fig. 44 Propofol-B1 cocrystal motif. Blue and orange masks reveal different orientations.

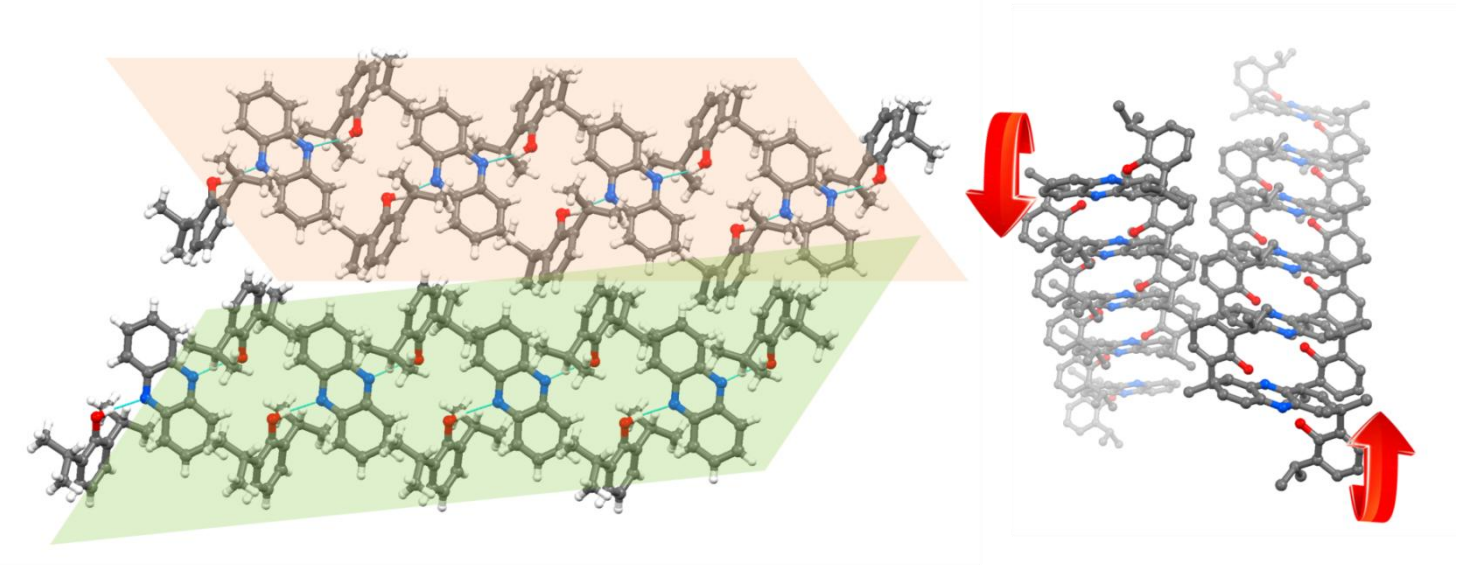

Fig. 45 Propofol-PH1 cocrystal motif. Green and pink masks reveal different orientations. Figure on the right reports the lateral view where is noticeable the singular motif with crossed layers.

3.3.2 Nicotine-DITF cocrystal 1:1

Halogen bond plays a key role in establishing solid intermolecular interactions between both nitrogen atoms of the nicotine (pyridinic and pyrrolidinic) and iodine atom of the coformer. DITF is a strong halogen bond donor thanks to the perfluorinated aromatic ring that is extremely electron poor, thus, iodine atoms present a really electron-deficient σ-hole. Iodine atoms are in *para* substitution and this favors a planar and linear arrangement. Linearity is stressed also by the presence of nicotine which interacts through halogen bonds with both nitrogen atoms (2.85 Å for $N_{pyridine}$···I, 3.04 Å for $N_{pyrrolidine}$···I) facing in opposite direction along the same plane (as shown in figure 46).

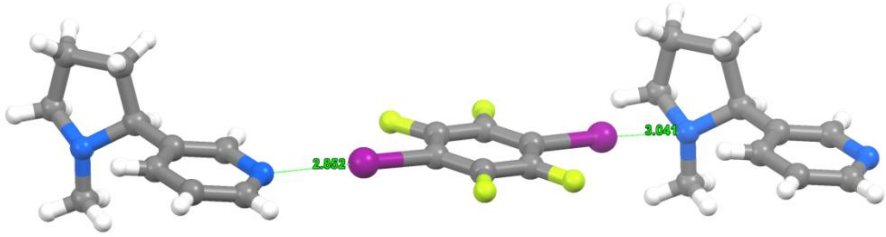

Fig. 46 Halogen bonding in the nicotine-DITF cocrystal. Distances are reported in Å.

Strings of nicotine and DITF which lay on the same plane are in contact with those laying on different planes through CH···F interactions ranging from 2.52 Å to 2.66 Å (distances C···F). The pyrrolidinic ring of nicotine is able to rotate around the C-C bond with the pyridinic ring in order to properly establish interactions through hydrogen atoms of the methyl group and hydrogen atoms bound to the carbon atoms of the ring. The interacting moiety is a tetramer, as shown in figure 47.

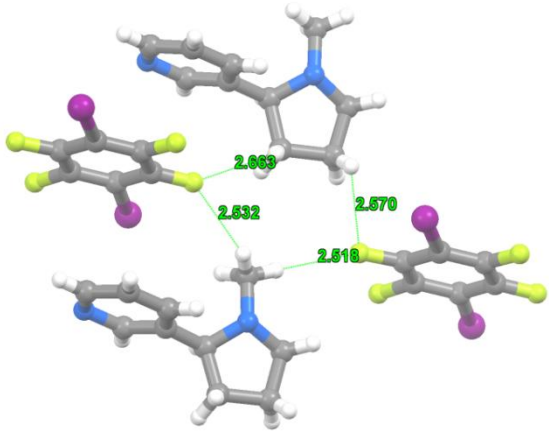

Fig. 47 Weak molecular interactions in the nicotine-DITF cocrystal. Distances are reported in Å.

Both nicotine and DITF have aromatic rings that interact through parallel displaced π-π stacking. DITF ring is extremely electron-poor and is capable of establishing valid offset stacking with the pyridinic ring of nicotine molecule. This kind of interactions tend to organize the overall system in alternated layers (fig. 49).

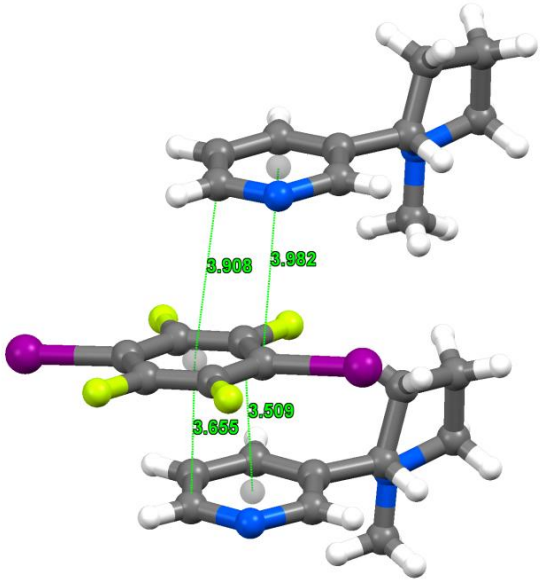

Fig. 48 Detail of parallel displaced π-π stacking between nicotine rings and DITF rings. Distances are reported in Å.

Characteristic arrangements of the molecules in the cocrystal are shown in fig. 49 and 50. Figure 49 reports the packed structure viewed along the *a* crystallographic axis: equidistant parallel planes are clearly noticeable as well as columns along which alternated nicotine and DITF molecules are located interacting through π-π stacking and CH···F interactions.

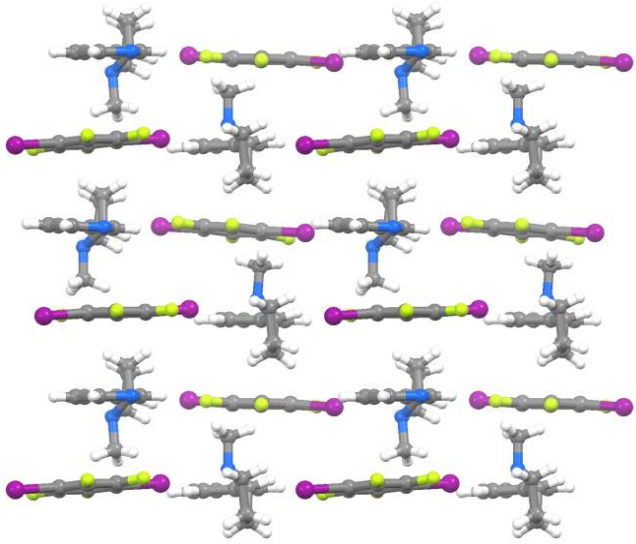

Fig. 49 Packing view along *a*-axis of the cocrystal nicotine-DITF.

The view along *c*-axis highlights the reciprocal disposition of the stacking planes. As previously said, nicotine and DITF molecules form characteristic strings interconnected through halogen bonds which lie on the same plane. Planes with different strings orientation are stacked together and rotated of 80° with respect to the other.

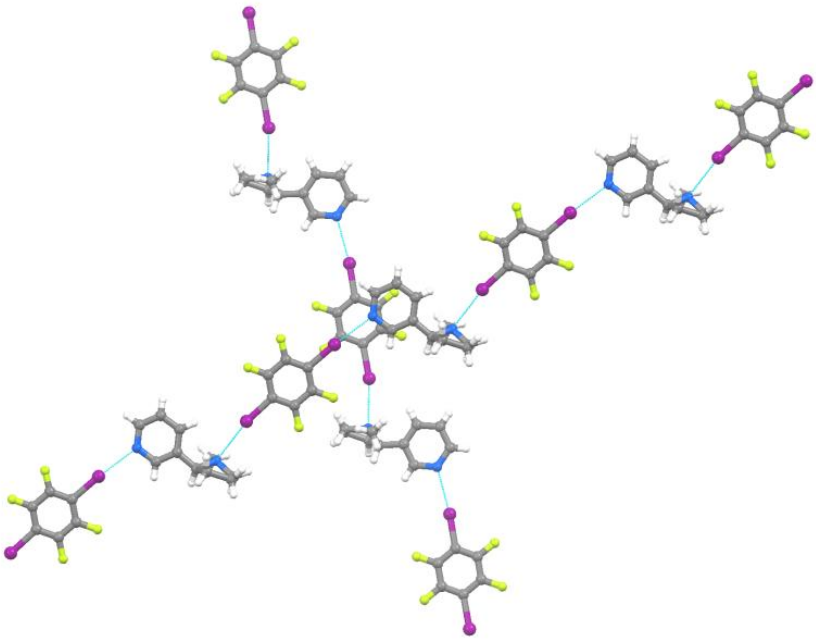

Fig. 50 Strings view along *c*-axis of the cocrystal nicotine-DITF.

3.3.3 Nicotine-DOB cocrystal 1:1

Intrigued by the results obtained with perfluorurated coformers, we performed cocrystallization trials with a strictly similar molecule: 4,4'-diiodooctafluorobiphenyl (DOB). Nicotine establishes strong halogen bond interactions which involve nitrogen atoms of both pyridinic ring and pyrrolidinic ring similarly to the nicotine-DITF cocrystal. The peculiarity of this structure is the arrangement of nicotine molecules and DOB molecules forming a sort of molecular ladder with DOB as the treads and nicotine molecules as the lateral handrails (fig. 51). One single molecule of nicotine interconnects two different molecules of coformer, generating an infinite pattern. The asymmetric unit of the cocrystal contains 4 independent molecules of DOB and 4 of nicotine leading to a total of 4 different $N_{pyridine}\cdots I$ intercations and 4 $N_{pyrrolidine}\cdots I$ interactions. Halogen bonds length for for $N_{pyridine}\cdots I$ are: 2.91 Å, 2.92 Å, 2.88 Å and 2.82 Å; while $N_{pyrrolidine}\cdots I$: 2.92 Å, 3.03 Å, 2.88 Å and 2.94 Å, resulting in equivalent stabilizing interactions. A major difference with respect to nicotine-DITF structure is the torsion of the two aro-

matic rings of the coformer with an angle of 57.87° between the planes where the two rings lay on. This conformation is typical of biphenyl rings[99] and, in perfluorurated systems, is due to F···F repulsion among fluorine atoms in *ortho* positions with respect to the twisted bond.

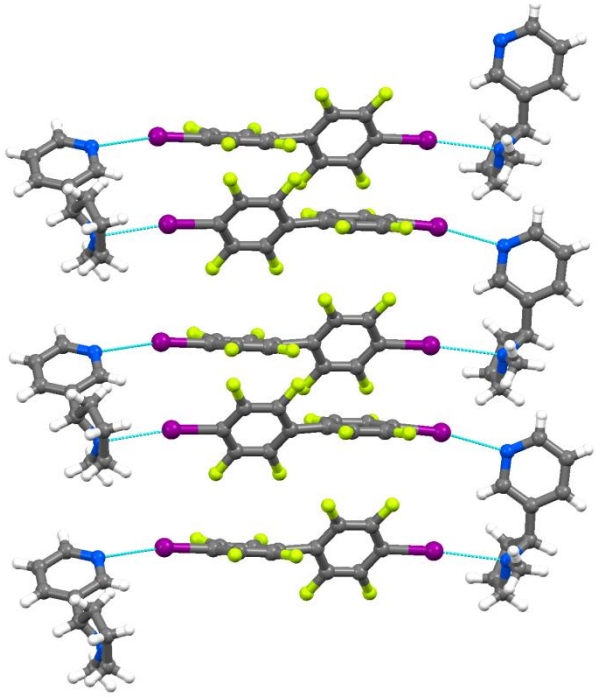

Fig. 51 Nicotine-DOB cocrystal structure motif.

A direct visual comparison of the cocrystal structure of nicotine-DITF and nicotine-DOB is shown in figure 52. Structures have been overlapped to facilitate the comparison and to emphasize differences. Nicotine molecule shows the pyrrolidinic ring completely twisted (180°) from one structure to the other. In the case of nicotine-DITF, nitrogen atoms point in opposite directions resulting in linear chains while in nicotine-DOB, nitrogen atoms face the same edge, leading to the peculiar ladder motif.

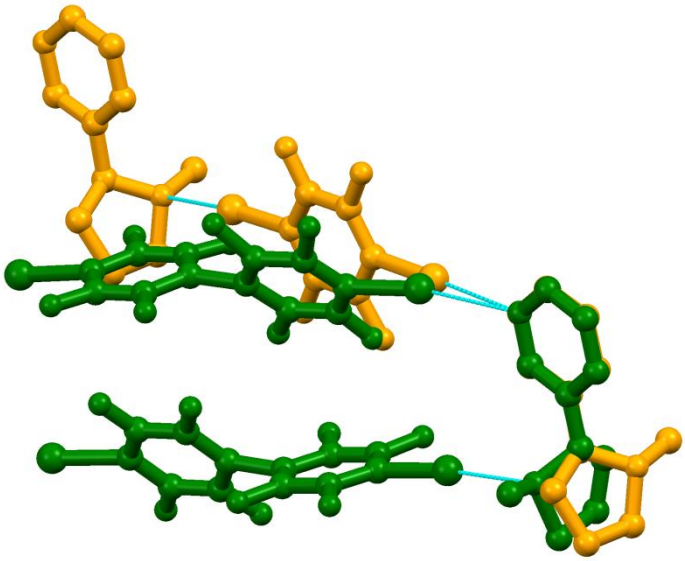

Fig. 52 Differences between nicotine-DITF (orange) and nicotine-DOB (green) structures. Hydrogen atoms have been omitted for clarity.

3.3.4 Nicotine - D1 cocrystal 1:1

Despite of the importance and the results of halogen bond, hydrogen bond turned out to be a solid and reliable interaction capable of playing the role of driving force in the formation of cocrystals. The coformer D1 is characterized by two hydroxyl groups, strong hydrogen bond donors which establish hydrogen bonds with both nitrogen atoms of the pyridine. The central benzene ring gives rigidity and acts as a pillar between one molecule of nicotine and another resulting in an infinite chain of slightly zigzagged hydrogen bonds (fig. 53). This characteristic trend can be compared to nicotine-DITF cocrystal typical trend (fig. 46) with the exception that the pyridinic rings of nicotine molecules (in nicotine-DITF) are coplanar with DITF molecules.

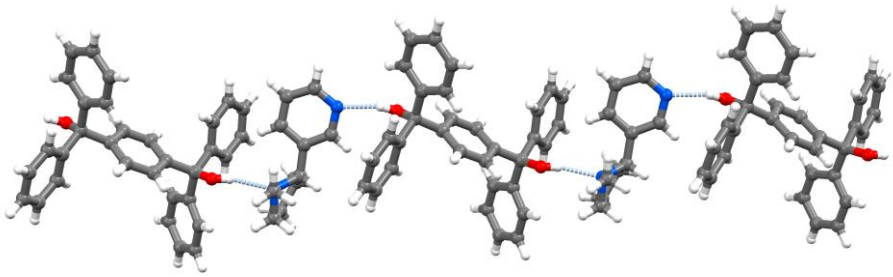

Fig. 53 Hydrogen bond chain in the nicotine-D1 cocrystal.

Whereas a structure containing nicotine in the same molar ratio (1:1) and 4,4'-*bis*(diphenylhydroxymethyl) hexadiyne is already deposited in the CSD with ref. code KERSAB, a structural comparison with nicotine-D1 cocrystal seems appropriate. Both 4,4'-*bis*(diphenylhydroxymethyl) coformers are rigid and linear and characterized by the presence of 4 phenyl rings and 2 hydroxyl groups; the latter are capable of establishing strong hydrogen bonds with nicotine whose geometries are reported in table 9.

KERSAB structure has been deposited in the CSD without hydroxyl hydrogen atoms and hydrogen atoms of methyl groups of nicotine are omitted as well. For this reason is not possible to correlate with great precision the specific geometries of the hydrogen bonds of the two structures. However, both nicotine-D1 and KERSAB hydrogen bonds D···A (Å)appear to be similar: the oxygen atom of the hydroxyl group which interacts with nitrogen atom of the pyridine is at a closer distance than the oxygen atom of the hydroxyl group which interacts with nitrogen atom of the pyrrolidinic ring for both cocrystals.

Table 9 Hydrogen bonds geometries.

Cocrystal	D-H···A	H···A (Å)	D···A (Å)	D-H···A (°)
Nicotine-D1	O-H···N_{py}	2.02	2.79	150.6
	O-H···N_{pyrrol}	2.16	2.93	152.8
KERSAB[100]	O-H···N_{py}	-	2.80	-
	O-H···N_{pyrrol}	-	2.88	-

One of the main difference between the 2 structures lays in the way nicotine molecules and coformer interact. In the case of KERSAB the main unit, generated by hydrogen bonding, is a tetramer made up of 2 nicotine molecules and 2 coformer molecules (fig. 54). This is totally different in respect to nicotine-D1 which is characterized by infinite chains of alternating nicotine and D1 molecules. Different arrangements are probably caused by spacers of different length which lead to specific conformation of the interacting molecules: the spacer in D1 molecule is 5.89 Å long while in KERSAB is 6.6 Å. Moreover, different nicotine conformations in the two cocrystals play a key role in determining the distinctive conformation of the molecules in the cocrystals as well. In the particular case of nicotine-D1, nicotine molecules appear always with the same spatial orientation. This is demonstrated by the fact that in the asymmetric unit there is only one independent nicotine molecule that generates the others by translation. Differently from this, KERSAB cocrystal shows two independent nicotine molecules in the asymmetric unit with two different spatial orientation, resulting in an overall diverse set of hydrogen bonds and a distinct structure.

Strings and tetramers mutually come together thanks to coformers establishing interactions (fig. 55). In nicotine-D1 cocrystal, hydrogen bonds involving C-$H_{aromatic}$···$O_{hydroxyl}$ groups form at 2.49 Å and 2.43 Å (H···A) distances, while in KERSAB cocrystal tetramers bond through C-$H_{aromatic}$···π interactions (3.74 Å and 3.67 Å C···C distance) which involve the *sp* carbon atom of the hexadyine and the hydrogen atom in *para* position of the phenyl ring of a different molecule of coformer.

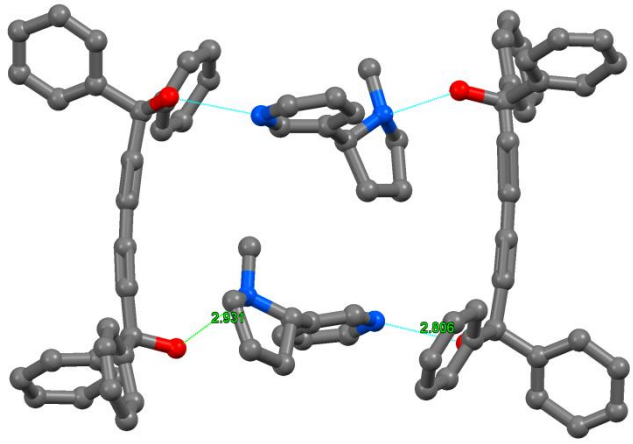

Fig. 54 Tetramers in KERSAB structure.

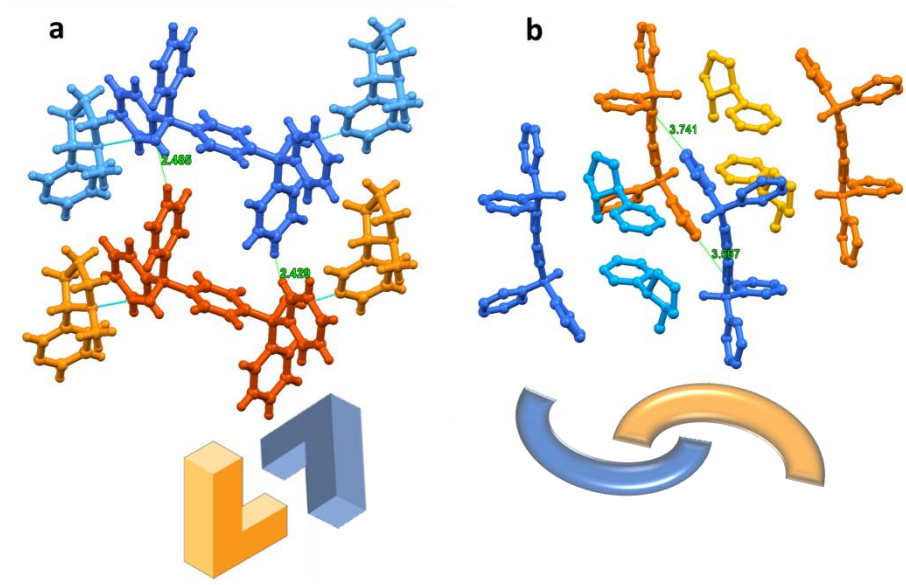

Fig. 55 Differences in units interaction between nicotine-D1 (fig.a) and KERSAB (fig. b) cocrystals.

3.3.5 Thymol-PH1 cocrystal 1:1

Thymol molecule is pretty similar to propofol for what concerns functional groups: both molecules are substituted benzene rings with one hydroxyl groups and alkyl groups. For this reason, thymol, is capable of forming quite strong hydrogen bond with proper acceptors. Phenazine has been chosen accurately and lead to cocrystal formation of two different types: two polymorphic forms (TH-PH1α and TH-PH1β) containing thymol and phenazine in 1:1 molar ratio form from different solution of different solvents. While polymorphism is a wide spread phenomenon, the number of reported polymorphic cocrystals is still very limited. It was once thought that cocrystals could be a means to prevent polymorphism but some recent examples of cocrystal polymorphism have been discovered and reported[101]. Similar to single component crystals, polymorphs of cocrystals can display significantly different properties.

Both TH-PH1α and TH-PH1β establish hydrogen bonds between hydroxyl groups of thymol and nitrogen atoms of phenazine with D···A distances of 2.84 Å and H···A distances of 2.03 Å (fig. 56 and fig. 57). A particular aspect that lumps together the two polymorphs is the participation of only one nitrogen atom of the coformer in the formation of hydrogen bonds with thymol molecules, resulting in 1:1 ratio. In both polymorphs the nitrogen atom of phenazine that does not interact through hydrogen bond with a hydroxyl group is engaged in a hydrogen bond with the methyl group of thymol at a distance of CH···A 3.76 Å and H···A 3.00 Å.

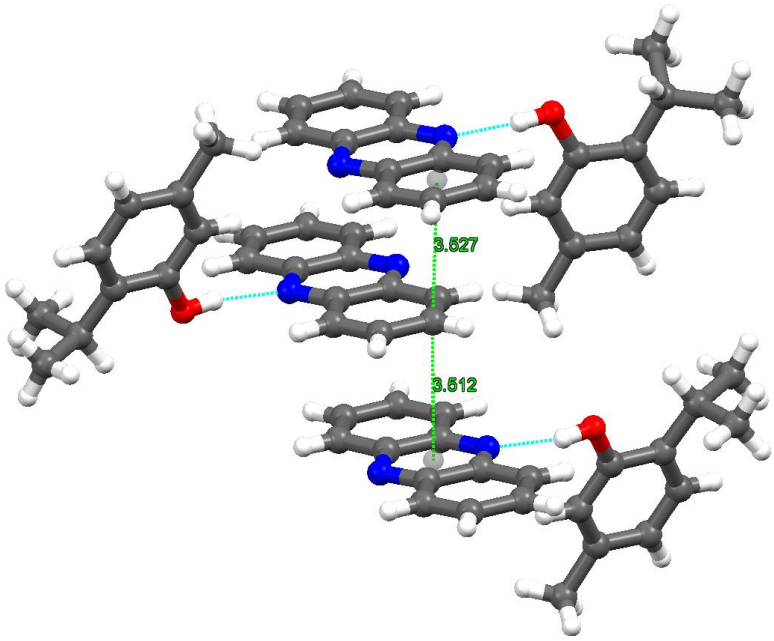

Fig. 56 TH-PH1α details of hydrogen bonding and stacking of PH1 molecules.

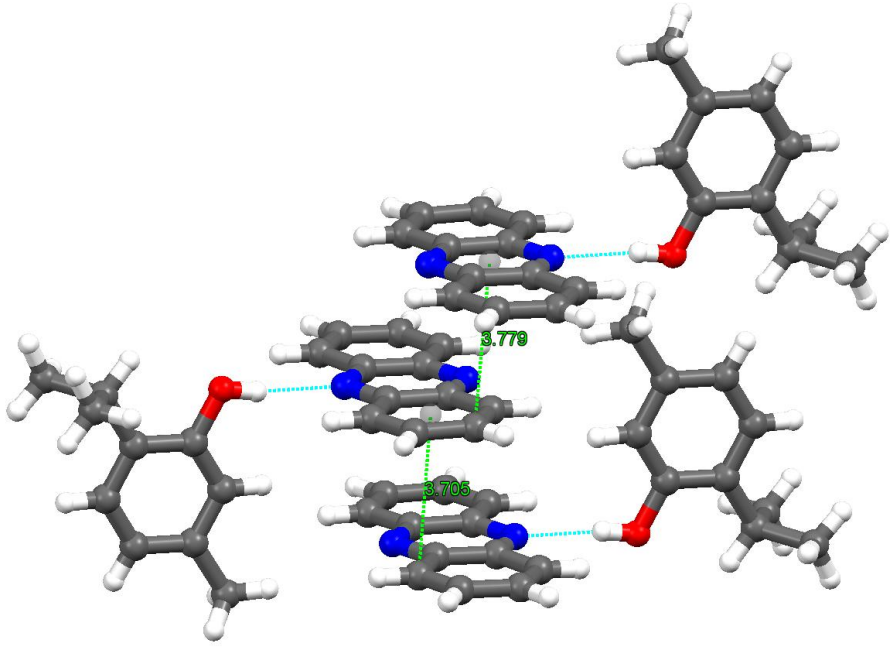

Fig. 57 TH-PH1β details of hydrogen bonding and stacking of PH1 molecules.

A striking role in the stabilization of a close packed structure is played by phenazine which stack in parallel displaced way at a distance of 3.53 Å and 3.51 Å for TH-PH1α and 3.70 Å and 3.78 Å for TH-PH1β. Distances are calculated considering the centroids of the aromatic ring of phenazine and the underlying orthogonal carbon atom of the phenazine ring located underneath. TH-PH1β phenazine molecules stack at a slightly wider distance respect with TH-PH1α phenazine molecules.

TH-PH1β is characterized by a different motif with respect to TH-PH1α structure (fig.58 and fig. 59). As it is shown in fig. 58, phenazine molecules that stack together arrange along columnar strings alternated with thymol molecules. Contrary to this, phenazine molecules in TH-PH1β structure are organized in 2 main sequential column formats, twisted by 150° one another.

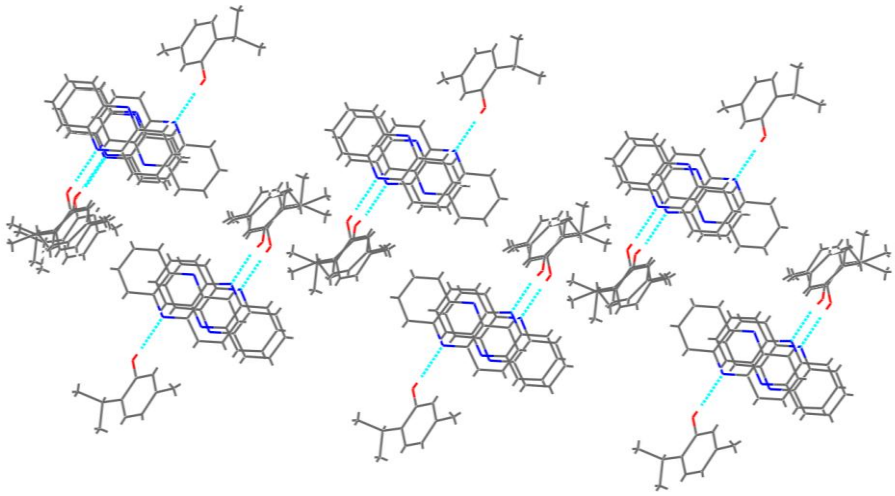

Fig. 58 Motif in TH-PH1α structure.

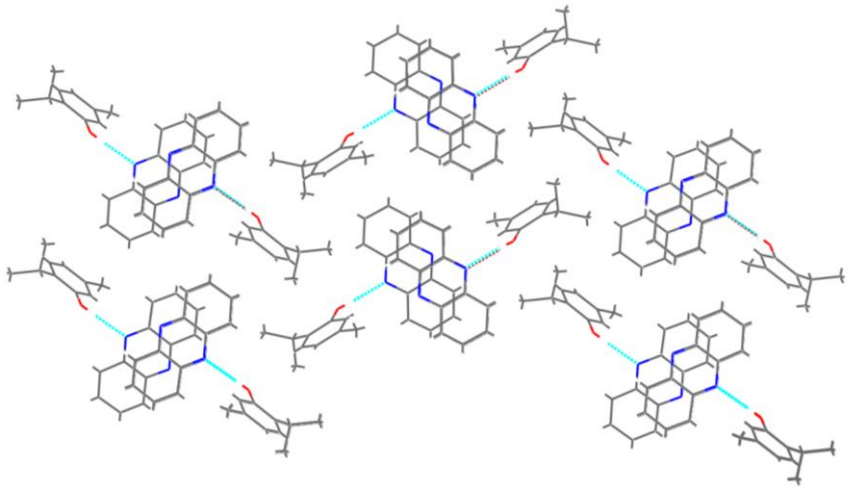

Fig. 59 Motif in TH-PH1β structure.

TH-PH1α cocrystal has been visually compared with propofol-PH1 cocrystal (fig. 60) in order to evaluate similarities in the structural unit based on hydrogen bond synthon. Two molecules of propofol bond one phenazine molecule (2:1 molar ratio) while just one molecule of thymol is involved in hydrogen bond with another molecule of phenazine. Furthermore, thymol molecule engages its methyl group in a CH···N hydrogen bond with the upper molecule of phenazine. This particular conformation twists the hydroxyl group leading to hydrogen bond with a lower than 180° angle (OH···N angle: 167.0°), very similar to 169.3° and 150.0° angles of the hydroxyl groups in the propofol-PH1 structures.

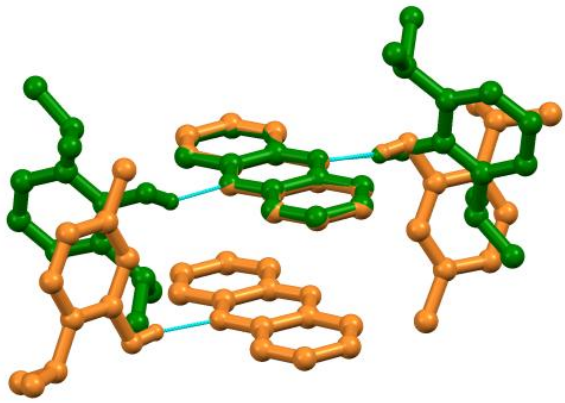

Fig. 60 Overlapping comparison between TH-PH1α (orange) and propofol-PH1 (green) structures.

3.3.6 Carv-PH1 cocrystal 2:1

Carvacrol molecule is a structural isomer of thymol and is characterized by exchanged methyl and isopropyl groups. Differently from what we have expected, considering both TH-PH1α and TH-PH1β cocrystals, a 2:1 molar ratio compound formed from solution. Two carvacrol molecules interact through hydrogen bond with both nitrogen atoms of one phenazine molecule at 2.26 Å (H···A) distance and 3.07 Å (D···A) distance with an angle of 170.1° (OH···N) (fig. 61 and 62). The two molecules of phenazine are related by an inversion point that lies exactly on the same plane of phenazine, centered in the middle of the central ring of the molecule.

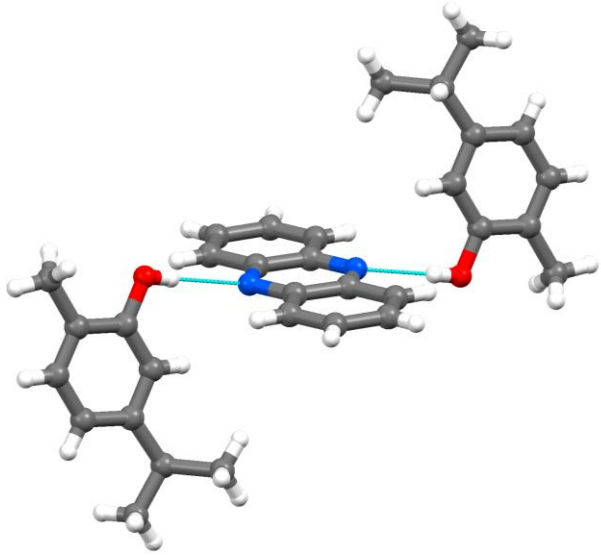

Fig. 61 Hydrogen bond interactions in carv-PH1.

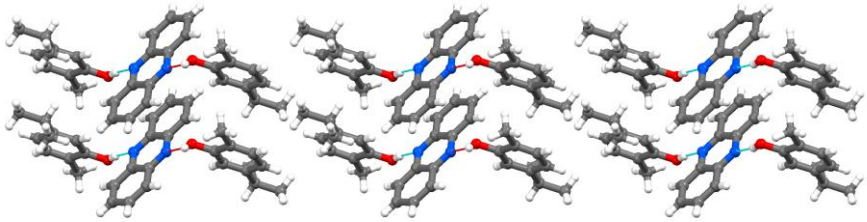

Fig. 62 Structural motif along *b*-axis of carv-PH1.

Phenazine molecules interacts through parallel displaced π-π stacking, in the same way of TH-PH1α and TH-PH1β, with 3.49 Å and 3.51 Å distances (calculated from the centroid of the aromatic ring of phenazine and the orthogonal carbon atom of the underlying phenazine molecule, as shown in fig. 63).

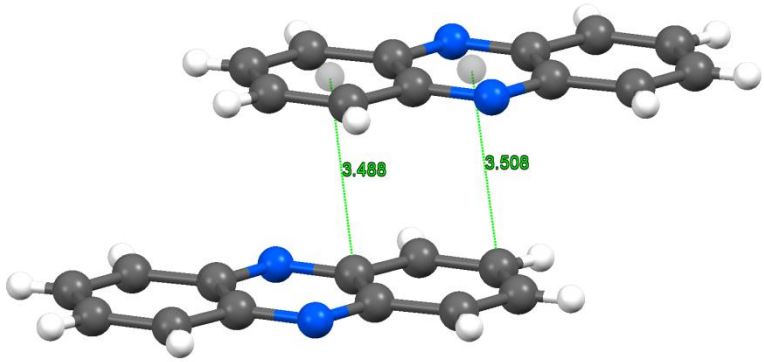

Fig. 63 π-π stacking of phenazine molecules in carv-PH1 cocrystal.

Similarities with propofol-PH1 cocrystal are evident if we consider that both are 2:1 molar ratio cocrystal with propofol molecules and carvacrol molecules related by symmetry operations (inversion points) that lie on the pyrazinic ring of phenazine. The main difference, shown in fig. 64, is that carvacrol molecules lie on the same plane and are perfectly orthogonal to the coformer while propofol molecules are slightly bent in two opposite direction, emerging from the plane.

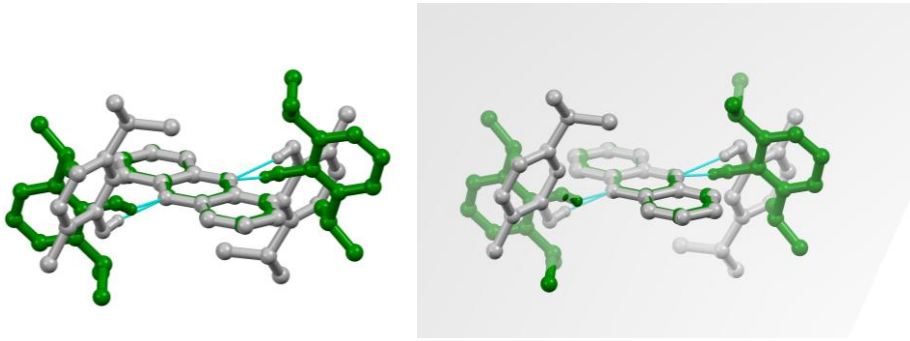

Fig. 64 Comparison between prop-PH1 and carv-PH1. Propofol-PH1 (green) and carv-PH1 (grey). On the right: carvacrol molecules belong to the plane reported in light grey.

3.3.7 Overall considerations on phenazine based cocrystals

Phenazine proved out to be a valid and effective partner for cocrystallization of our molecule of interest, leading to many interesting results. Propofol, thymol and carvacrol have been stabilized in a solid state formulation with higher melting points. It is important to highlight the strict correlation between molecular structure, functional groups and specific conformation, and the final cocrystal structure. All of these molecules share a substituted phenol ring with slightly different alkyl groups. Hydroxyl group plays a key role in establishing strong hydrogen bond interactions that decisively stabilize the overall structure. Not great differences occur between the cocrystals, for what concern hydrogen bonds (Table 10): prop-PH1 shows the shortest hydrogen bond distances and the most twisted angles, the two polymorphs (TH-PH1α and TH-PH1β) present the same distances and similar angles closer to 180°, and eventually, carv-PH1 hydrogen bond is the longest, thus the weakest but comparable with the others. Alkyl groups are sometimes engaged in CH···π interactions (TH-PH1α and TH-PH1β) or CH···N hydrogen bonds (prop-PH1) or does not participate effectively in the formation of stabilizing interactions (carv-PH1).

Table 10 Hydrogen bond details. Std deviations = 0.02

Cocrystal	H···A (Å)	D···A (Å)	D-H···A (°)
Prop-PH1	1.98 / 2.04	2.79 / 2.78	169.3 /150.0
TH-PH1α	2.03	2.84	167.0
TH-PH1β	2.03	2.84	170.8
Carv-PH1	2.16	3.07	170.1

Another important interaction is π-π stacking that occur between phenazine molecules in every cocrystal reported, except for prop-PH1. Stackings are of the parallel displaced type ranging from 3.50 Å (carv-PH1) to 3.74 Å (TH-PH1β), perfectly within the standard range for π-π stacking interactions (3.2-3.8 Å)[102] (table 11). The presence of a pyrazinic ring in phenazine, which is electron withdrawing, may increase the effectiveness of the displaced interaction. The central ring of phenazine, in fact, is strongly electron rich while the two lateral aromatic rings are electron deficient. This peculiarity favorably affects the parallel displaced geometry because electron rich rings tend to stack with electron poor ones.

Table 11 Phenazine molecules π-π stacking distances. Std deviations = 0.02

Cocrystal	π-π medium value (Å)
Prop-PH1	No stacking interactions
TH-PH1α	3.52
TH-PH1β	3.74
Carv-PH1	3.50

3.3.8 EU-F1 cocrystal 1:1

Eucalyptol and orcinol (F1) cocrystallize in 1:1 molar ratio interacting through hydrogen bonds (fig. 65) involving one hydroxyl group of F1 as the H-bond donor and the oxygen atom of EU as the acceptor (1.81 Å (H···A), 2.65 Å (D···A)). F1 molecules posses two hydroxyl groups in *meta* position with respect to the methyl group and are both able to give quite strong hydrogen bonds. Therefore, the hydroxyl group which is not engaged with the EU molecule, bonds to another hydroxyl group of a neighboring F1 molecule (2.77 Å (D···A)). These interactions lead to an endless chain based on hydrogen bonds and made up of F1 molecules. Every single molecular unit (F1 molecule) interacts with one EU molecule arranged on both sides of the chain, alternatively, resulting in a sort of chain with syndiotactic branches. Two different chains interacts each other through weak CH interactions thanks to the methyl group of the F1 molecules and -CH_2- and methyl groups of EU molecules. The overall arrangement is shown in fig. 66 where different chains are masked with two different colors.

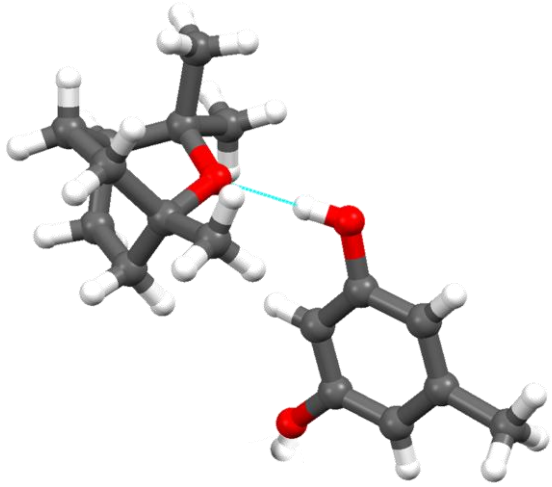

Fig. 65 Structural detail of EU-F1.

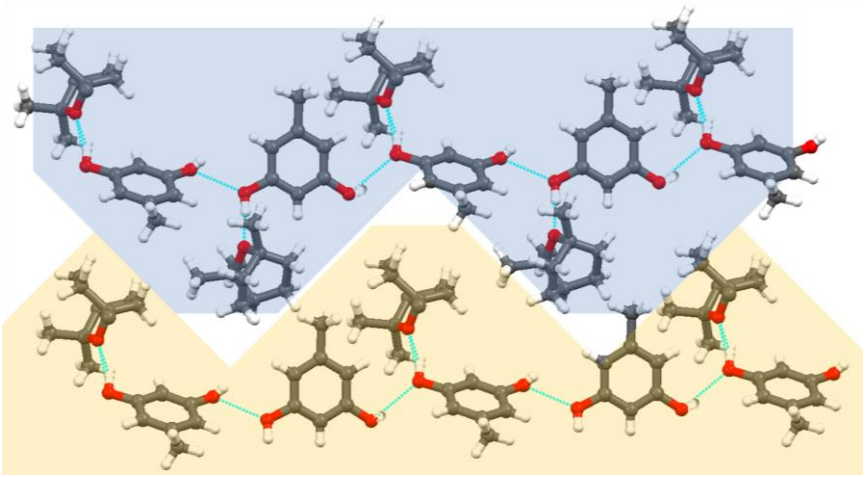

Fig. 66 Molecular arrangement in EU-F1cocrystal showing hydrogen bond patterns which form two alternated layers.

3.4 X-ray powder diffraction on cocrystals

Thymol and PH1 cocrystallize in two different polymorphs depending on the solvent used for the experiment: TH-PH1α and TH-PH1β. A new intriguing species formed via grinding as well and, because it is a powder sample, x-ray powder diffraction analysis turned out to be fundamental. First of the molar ratio of both thymol and PH1 in the new crystalline phase was checked. As reported in fig. 67 three different patterns are superimposed: the red pattern is the calculated from the thymol structure present in CSD (refcode: IPMEPL), the blue pattern is the experimental of the thymol-PH1 (1:1 molar ratio) grinding and the light-blue pattern is the experimental of the thymol-PH1 (2:1 molar ratio) grinding. It is noticeable that 2:1 pattern is characterized by many peaks superimposed with the calculated pattern of thymol, thus a relevant amount of crystalline thymol is present in this new 2:1 phase. Differently from that, 1:1 phase is unique and shares no peaks in common with the calculated pattern, proving that there is no excess of thymol.

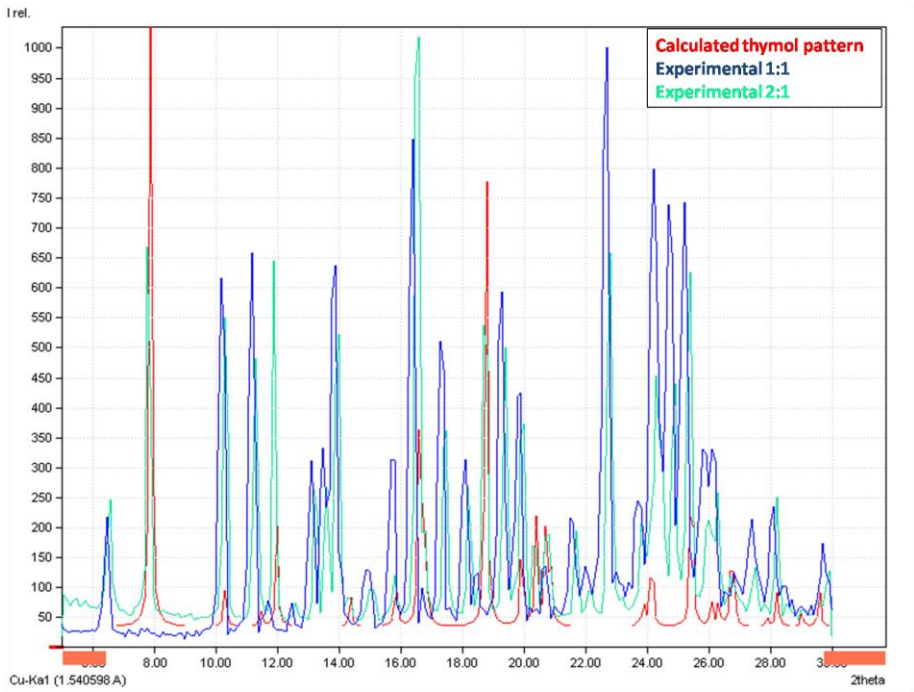

Fig. 67 Superimposition of thymol-PH1 patterns with different molar ratio and thymol pattern.

According to these findings, the experimental 1:1 pattern was matched with both TH-PH1α and TH-PH1β calculated patterns in order to identify any possible correlation. Surprisingly, thymol-PH1 (1:1 molar ratio) powder pattern perfectly matches the calculated pattern of TH-PH1β single crystal structure (as shown in fig. 68) and significantly differs from the calculated of TH-PH1α. This demonstrates that TH-PH1β polymorphic form can be also synthesized via grinding leading to a pure sample.

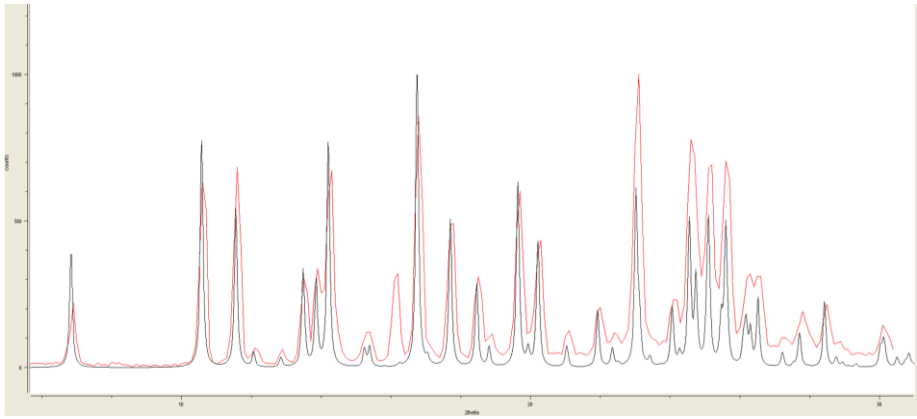

Fig. 68 Superimposition of experimental 1:1 pattern of thymol-PH1 (red pattern) and calculated pattern from TH-PH1β crystal structure (black pattern).

4. RESULTS and DISCUSSION: INCLUSION INTO MOFs

4.1 TGA and mass spectrometry analysis on PCN6mix

Mass spectroscopy turned out to be a fast and practical technique to analyze loaded samples and gave us interesting results. Both the mass spectra of PCN6mix loaded with propofol and nicotine show the characteristic peaks of the guest molecules (fig. 69): in the case of propofol 162.9 ($C_{11}H_{15}O$), 178.2 ($C_{12}H_{18}O$); in the case of nicotine 84.0 ($C_5H_{10}N$), 133.1 ($C_8H_9N_2$), 161.1 ($C_{10}H_{13}N_2$). MS data indicate the presence of both guests molecules within the crystalline samples employed for the analysis.

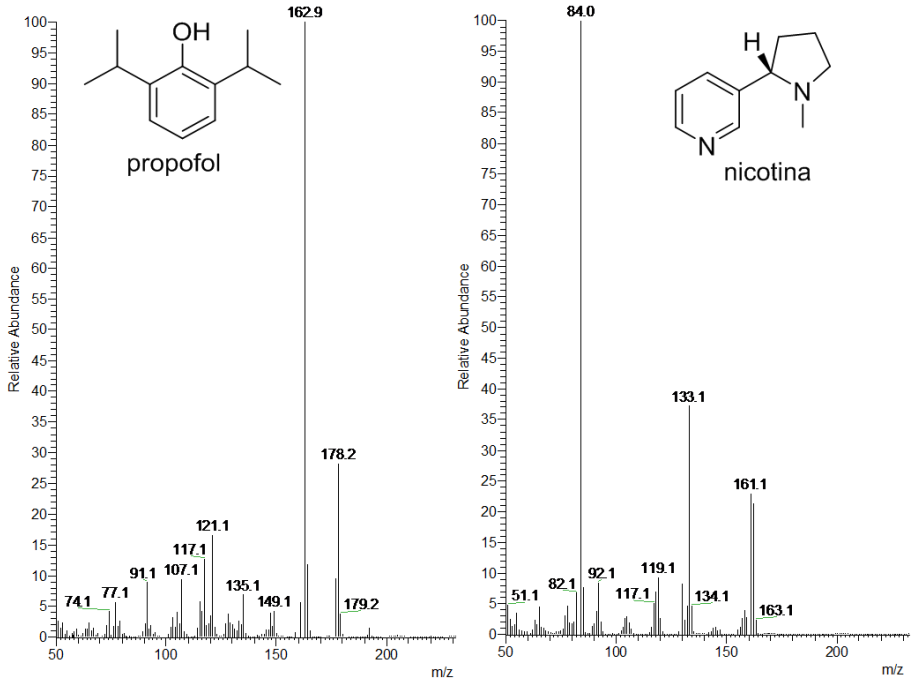

Fig. 69 DIP/EI mass spectra of PCN6mix@propofol and PCN6mix@nicotine.

In figure 70 are reported both the TGA curve for PCN6mix loaded with nicotine (red line) and the derivative of the curve (in blue dashed line). Two main weight loss are visible in the range within 220-250°C and 325-340°C. The first band (21% weight loss) can be ascribed to the guest that overflows and the second neat peak is the decarboxylation of the ligands of the MOF, which lead to the decomposition of the crystalline material. As well as MS, TGA confirms that inclusion of guests took place.

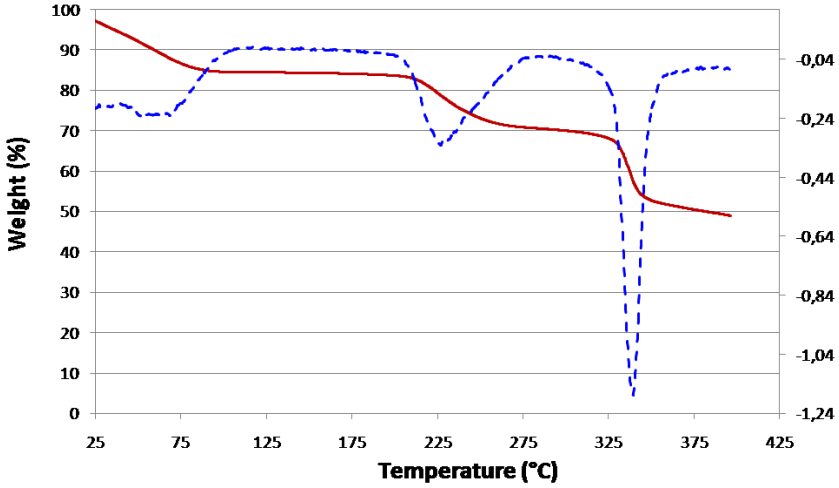

Fig. 70 TGA on PCN6mix@nicotine sample.

4.1 UV monitoring

Unfortunately no experimental evidence of the inclusion of either propofol or nicotine in H-KUST arouse. The experiments performed did not show interesting results: concentrations of the guests did not decrease over time demonstrating that, in DCM solution, the uptake of the guests in the MOF had not happened. What is important to stress is the fact that the experiments were not performed using pure guest compounds, hence the presence of a solvent may have affected the inclusion, competing with the guests molecules or retaining them in solution.

Intriguing results have been obtained using PCN6mix and nicotine in a DCM solution. In this case it is clearly visible in table 12 an exponential decrease in concentration, starting from t_0 to t_6 (after 11 days). After this period the concentration of nicotine seems to reach a *plateau* and remain constant. The overall decrease in concentration is around 240 times the starting concentration (from $4.19 \cdot 10^{-3}$ M to $1.74 \cdot 10^{-5}$ M).

Table 12 Concentration of nicotine in every aliquots with respective time of sample taking.

	Time (min)	Conc (M)
t_0	0	4.19E-03
t_1	10	4.10E-03
t_2	36	3.60E-03
t_3	49	3.40E-03
t_4	5495	5.39E-04
t_5	10975	7.37E-05
t_6	16055	1.74E-05

As shown in figure 71 we can assume that the system follows first-order kinetics. The initial decrease of nicotine is extremely abrupt and this might be due to the initial interactions of the guests with the metal sites which soon end up being all occupied and the inclusion keeps going slower and slower. The initial volume of nicotine was 3.365 µl and the final volume of nicotine can be calculated from the concentration at t_6 (0.014 µl). It is therefore possible to establish the amount of nicotine entrapped in the cavities, which is 3.365 µl - 0.014 µl = 3.351 µl. 99.58% of the nicotine entered the cavities of the MOF. It is barely impossible to establish with precision how many moles of nicotine are entrapped for each mole of the MOF, thus calculating how many nicotine molecules are entrapped in every cavity, because PCN6mix is a mixture of both interpenetrated (PCN6) and not interpenetrated (PCN6') species with different molar weights.

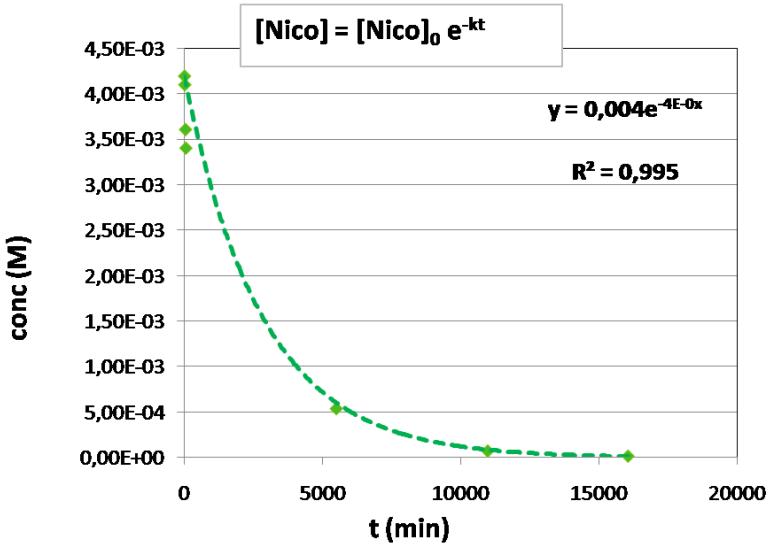

Fig. 71 Exponential plot showing the decrease of nicotine concentration over time for the experiment PCN6mix@nicotine in DCM.

4.2 SC-XRD analysis on PCN6mix

The crystals selected for x-ray diffraction at Elettra synchrotron came from the similar batches of PCN6mix. It was impossible to previously determine if the selected crystal was a PCN6' (cubic lattice) or a PCN6 (tetragonal lattice). However, both crystalline samples were collected and their data analyzed using iMosflm[103] for cell determination, integration and data reduction and Olex2 for structure resolution. In order to focus only on the electron density within the cavities of the MOF, the already known structure of the PCN6/PCN6' was taken from the .cif file from the CSD and kept fixed. Only the inner electron density was mapped using a mask tool in Olex2 and after tedious steps the resulting map appeared as shown in fig. 72. PCN6' containing nicotine slightly differs from its counterpart activated that never came in contact with the guest (*PCN6' activated*). The electron density map, reported in green, shows peculiar blobs in close proximity to copper atoms of the *paddle-wheel* cluster (as evidenced by circles in the figure), causing speculation that nicotine is coordinating it. In particular, the shape of the modeled electron density exactly follows the shape of the pyridinic ring of the guest. This particular type of coordination is already known in literature[104] and is reported in fig. 73. Two nicotine molecules coordinate, through

the pyridinic nitrogen atoms, the copper atoms (distance: 2.17 Å) of the cluster which is extremely similar to the one of PCN6/PCN6' framework having, instead of carboxylate ligands, tetramethacrylate ligands.

For what concern PCN6 loaded with nicotine the results are even clearer and more interesting. As reported in fig. 72, the electron density blobs look equivalent to PCN6@nicotine. A specific zone near the copper cluster has been zoomed in order to clearly evidence out the electron density that has the exactly shape of a nicotine molecule. The difficulty in solving the structure of the molecules of the guest is primary due to the disorder of the molecules inside the cavities. Nicotine molecules are located in the inner cages of the MOF keeping precise positions only in proximity of the clusters, thanks to coordination. The rest of the cavity is filled with a random number of nicotine, water molecules could be present too in some cavities and their orientation is disordered. All of these reasons negatively contribute to the improvement of the resolution of the system. In addition, nicotine rings are able to rotate, thus, even the "fixed" molecules that coordinate the clusters are characterized by mobile pyrrolidinic rings that are impossible to be precisely solved and difficult to be mapped.

Eventually, the volume of the cavities of both PCN6 and PCN6' were compared to the molecular volume of nicotine molecules, considering a packing coefficient equal to 0.6 (60%), which is a realistic value for a liquid-like packed system. It is therefore possible to approximately evaluate the number of nicotine molecules present in the cages. PCN6' cavities may host 70 nicotine molecules with a predicted number of electrons equal to 6000, strictly similar to the experimental value: 7000. PCN6 cavities may host up to 30 nicotine molecules with a predicted number of electrons equal to 2700, and the experimental value is 2000. Also the activated PCN6', that had never entered in contact with nicotine, presents 5000 electrons inside its cavities, ascribable to entrapped molecule of solvent (DCM).

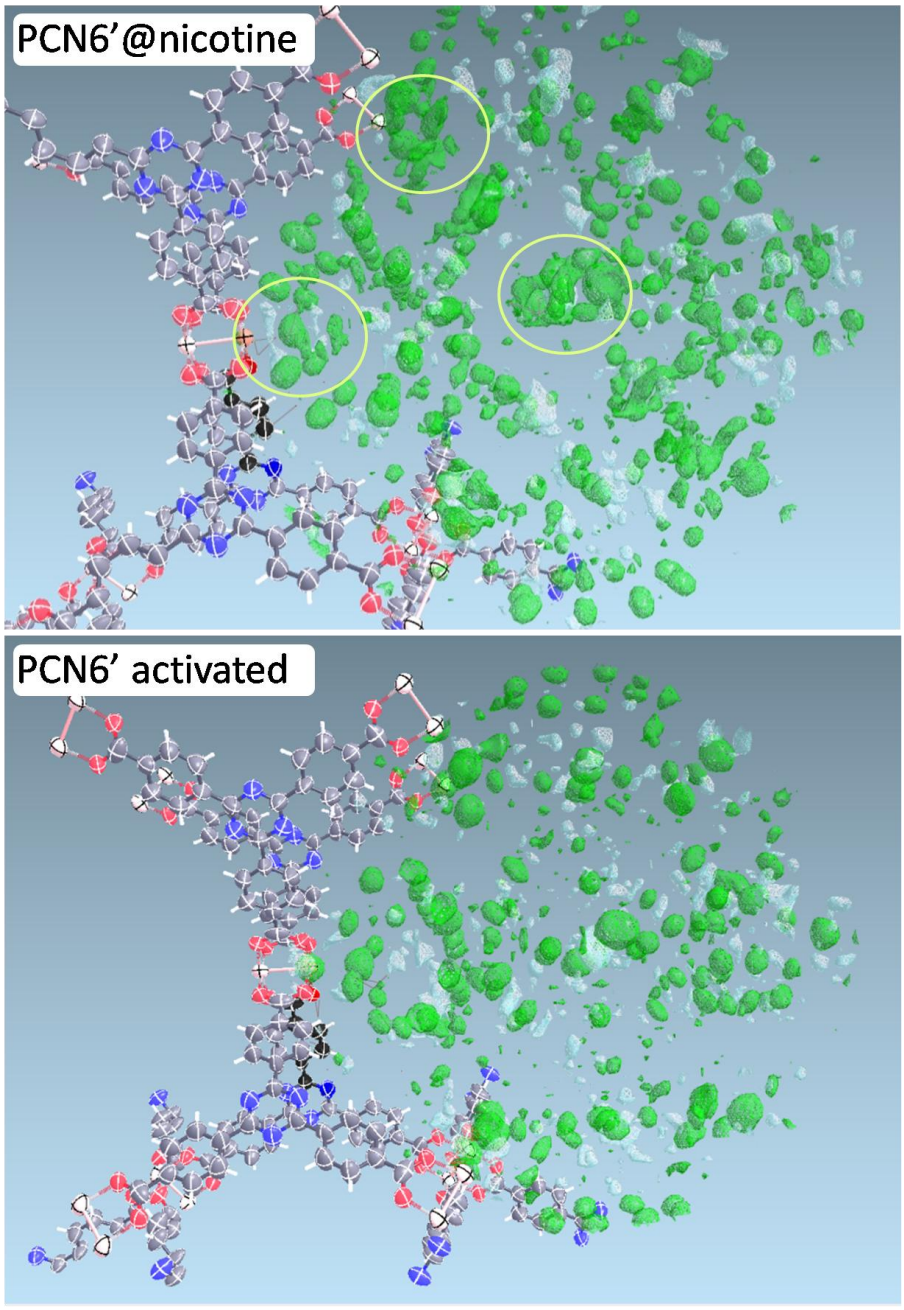

Fig. 72a Electronic density mapped inside the cavities of PCN6' containing nicotine and just activated.

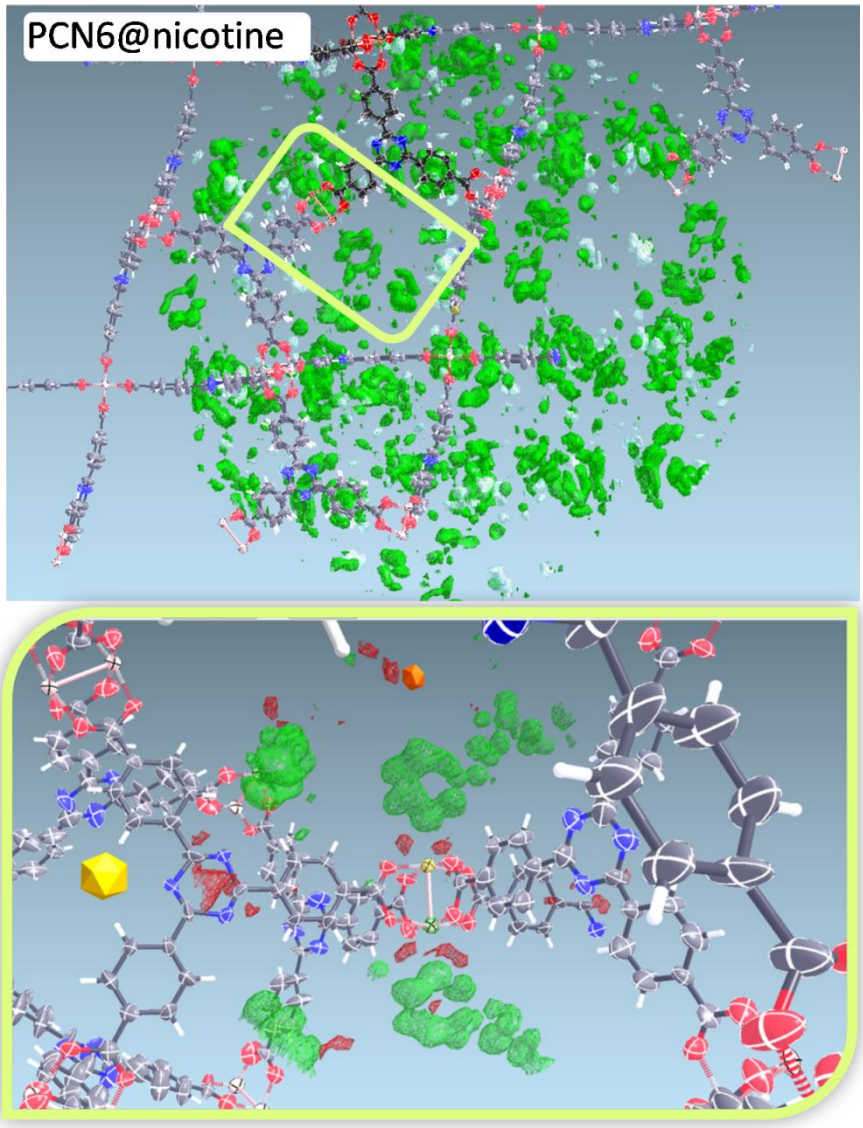

Fig. 72b Electronic density mapped inside the cavities of PCN6 containing nicotine. Zone within the yellow shape has been zoomed.

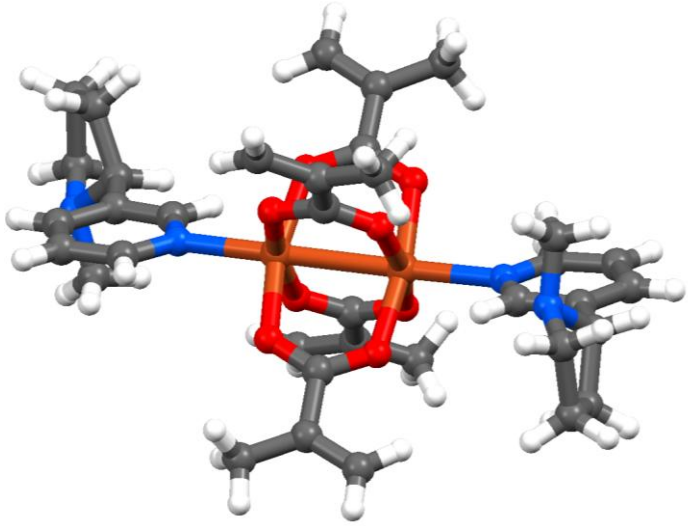

Fig. 73 Structure of tetramethacrylate Cu(II) *paddle-wheel* coordinated by two nicotine molecule, refcode on CSD: SURSEE.

The voids function on Mercury (CCDC)[105] allows any empty spaces (voids) in crystal structures that are big enough to contain a spherical "probe" of a given radius to be found. *Calculate voids using Contact Surface* is a specific option that maps the volume that can be occupied by the full probe (including its radius) and thus gives an estimate of the volume that could be filled by solvent or guest molecules. As reported in fig. 74, voids were calculated for both PCN6 filled with water molecules and PCN6 filled with nicotine molecules. What strikes most is the amount of room available in the MOF containing water and that can be filled with larger molecules as happened with nicotine. There is undoubtedly plenty of space in the cavities of the MOF.

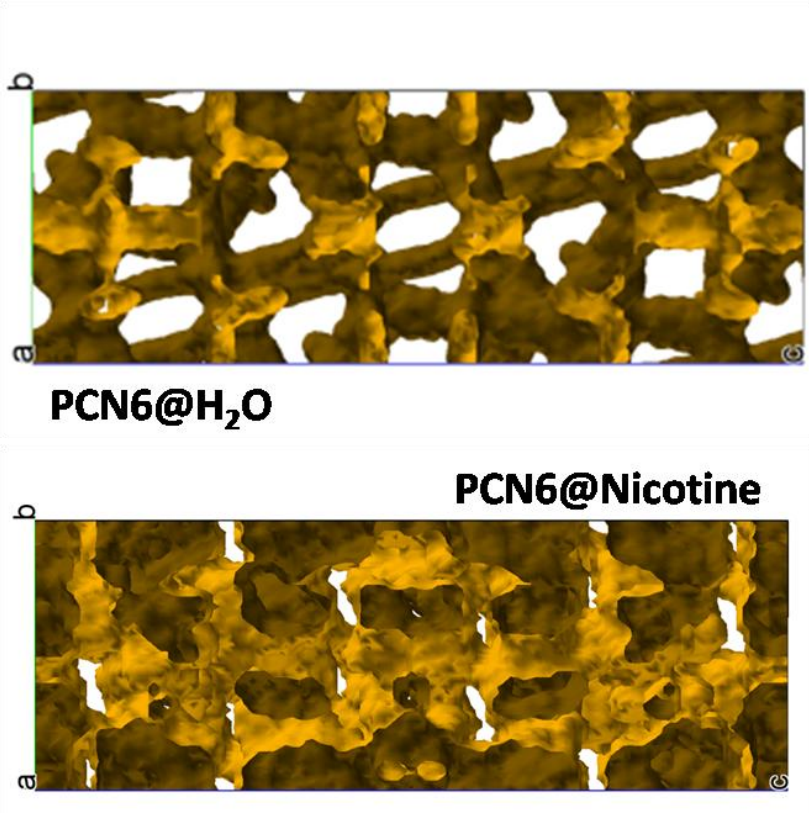

Fig. 74 Voids for PCN6 containing water and nicotine.

5. SUMMARY and CONCLUSIONS

The main purpose of the research project has been achieved with some interesting findings. New cocrystals forms of volatile APIs and nutraceutical compounds have been synthesized and their structures have been described. One of the key results is the thermal stability of these new crystalline formulations which is improved with respect to the original molecular formula. The pharmaceutical target melting point value of 100°C, where an API can be considered effectively stable, was reached by nicotine (with nicotine-D1 cocrystal), EU-F1 cocrystal and almost reached by propofol-B1 and thymol (TH-PH1α and TH-PH1β cocrystals). This is a striking result particularly if we consider that phenazine is not toxic, cheap and proved out to be a efficient partner for cocrystallization. Furthermore, ternary phase diagram and solubility measurements have been built and studied for just one cocrystal system (propofol-B1 in water) proving that they both could be rational and powerful tools to define the properties of complex systems composed by solid and liquid components. On the whole, the strategy of cocrystallization turned out to be a practical and novel method to stabilize compounds. Further studies might focus on the description of ternary phase diagrams of other cocrystals and in employing biocompatible coformers and in improving dissolution rate, thermal stability and effectiveness of the primary ingredient. Computational studies may produce intriguing results and lead to a more schematic approach for what concerns molecular interaction and calculation of the energy of the cocrystal.

On the other hand, stabilization inside the cavities of metal organic frameworks gave interesting results as well but proved out to be more difficult and sometimes tricky. In the specific case of PCN6'/PCN6, which is the only efficient MOF, a control of the crystal phase during the synthesis was impossible, thus it is dramatically difficult to estimate the amount of both species in the solid product. Although entrapment evidences are clear and confirmed by many different experimental findings, the overall method is not trustworthy and affected by randomness in the initial phase. Further efforts may be put into detecting a more reliable and reproducible metal organic framework which may guarantee promising results in the stabilization of a large variety of small molecules.

6. APPENDIX

6.1 Cocrystallization experiments

Abbreviations:

- se = solvent evaporation
- gr = grinding
- as = antisolvent
- dm = direct mixing
- cof = coformer
- synth = synthesis
- MR = molar ratio
- ETAC = ethyl acetate, MeOH = methanol, DMF = dimethylformamide, DCM = dichloromethane, ac = acetone, THF = tetrahydrofuran, EtOH = ethanol, Et_2O = diethyl ether.
- Coformers: B1 = 4,4'-bipyridine, F1 = orcinol, DITF = 1,4-diiodotetrafluorobenzene, DOB = 4,4'-diiodooctafluorobiphenyl, PH1 = phenazine, D1 = 4,4'-*bis*(diphenylhydroxymethyl)benzene, TBD = 1,5,7-triazabicyclo[4.4.0]dec-5-ene.

All molar ratio are reported as follows: *API/nutraceutical : coformer*.

Table 13 Propofol cocrystallization trials.

Cof	Synth	Solvent	MR	Results
2,2'-pyridil	dm, se	DCM, MeOH	2:1, 1:1	liquid
carvacrol	se	ac	1:1	liquid
2,2'-bipyridine	se	ac, MeOH, THF, MeOH	1:1, 2:1	liquid + cof
2,2'-bipyridine	as	DCM + DMF	1:1, 2:1	liquid + cof
B1	se	ac, MeOH	2:1	**cocrystal**
PH1	dm, se	DCM, ETAC, MeOH	2:1	**cocrystal**
1,2-di(4-pyridil)ethylene	dm, se	DCM	1:1, 2:1	liquid + cof
2,6- dihydroxy pyridine	dm, se	DCM, ac	1:1, 2:1	liquid + cof
2,6- diamino pyridine	se	ac	1:1	liquid + cof
4-methylaminobenzoic acid	se	EtOH	1:1	liquid + cof
5-amino isophthalic acid	se	MeOH	1:1	cof hydrate
homophthalic acid	se	ac	1:1	cof
4-dimethylaminobenzoic acid	se	EtOH	1:1	liquid + cof
mandelic acid	dm	-	1:1	liquid + cof
terephthalic acid	dm	-	1:1	liquid + cof

2-mercaptobenzoic acid	dm	-	1.1	liquid + cof
4-aminobenzamide	se	ac	1.1	liquid + cof
Isonicotinamide	se	ac	1.1	liquid + cof
isatine	se	ac	1:1	liquid + cof
3-hydroxy-4-aminobenzoic ac.	se	ac	1:1	liquid + cof
2,6-diacetylpyridine	se	ac	1:1	liquid + cof
2,6-dichloropyridine	se	ac	1:1	liquid + cof
di-(2-pyridil)-keton	se	ac	1:2	liquid + cof
hydroquinone	se	ac	1:1	liquid + cof
SALOPH	se	ac	1:1	liquid + cof
1,4-diamino anthraquinone	se	ac	1:1	liquid + cof
α-pyridoin	se	ac	1:1	liquid + cof
2-benzoyl-pyridin	se	ac	1:1	liquid + cof
1H-1,2,3-triazol[4,5-b]-pyridine	se	ac, MeoH	1:1	liquid + cof
4-aminophenol	dm, se	ac	1:1	liquid
guanidine	se	MeOH, EtOH, H_2O	1:1	liquid
α-(4-pyridyl)benzhydrol	se	ac	1:1	liquid
Malchite green	dm, se	ac	1:1	liquid
TBD	se	MeOH	1:1, 2:1	cof
Resorcinol	dm, se	ETAC	1:1, 2:1, 1:2	liquid + cof
F1	dm, se	ETAC	1:1, 2:1, 1:2	liquid + cof
m-cresol	dm, se	ETAC	1:1, 2:1, 1:2	liquid + cof

Table 14 Nicotine cocrystallization trials.

Cof	Synth	Solvent	MR	Results
3-amino-4-hydroxybenzoic acid	se	ac	1:2	liquid + cof
4-amino-3-hydroxybenzoic acid	se	ac	1:2	liquid + cof
4-aminobenzoic acid	se	ac	1:2	liquid + cof
3-(4-aminophenil) propionic acid	se	MeOH	1:1	liquid + cof
4-(4-amino) butirric acid	se	MeOH	2:1, 1:1	liquid + cof
4-Iodo-phenol	se	DCM, Et_2O	1:2	liquid + cof
4-ammino-py	se	MeOH	1:1	liquid + cof
4-methyl amino benzoic acid	se	EtOH	1:1	liquid + cof
5-amino isophthalic acid	se	MeOH	1:1	cof hydrate
homophthalic acid	se	ETAC	1:1	liquid + cof
4-aminobenzamide	se	ac	1:1	liquid + cof
2-cyclohexen-1-ol	se	THF	1:1, 1:2	2 liquids

D (-)-α-phenylglycine	dm	-	1:1	liquid + cof
L-valine	dm	-	1:1	liquid + cof
mandelic acid	dm	-	1:1	liquid + cof
terephthalic acid	dm, se	MeOH + NaOH	1:1	liquid + cof
isonicotinic acid	dm	-	1:1	liquid + cof
isatin	se	ac	1:1	liquid + cof
2,6- diamino pyridine	se	ac	1:1	liquid + cof
1,4-diamino anthraquinone	se	ac	1:1	liquid + cof
4-aminophenol	dm	-	1:1	liquid
DITF	dm, se	THF	1:1	**cocrystal**
hydroquinone	dm	-	1:1	liquid + cof
resorcinol	dm	-	2:1	liquid + cof
DOB	se	THF	1:1	**cocrystal**
I_2	dm, se	ac	1:1	liquid
D1	se	DCM	1:1, 2:1	liquid
D1	se	THF	1:1	**cocrystal**
1,4-dibromotetrafluorobenzene	se	DCM, MeOH	1:1, 2:1	liquid
1,4-dibromobenzene	se	DCM, MeOH	1:1, 2:1	liquid
4,4'-dibromooctafluorobiphenyl	se	DCM, MeOH	1:1, 2:1	liquid
4,4'-dibromobiphenyl	se	DCM, MeOH	1:1, 2:1	liquid
2,6- dihydroxy pyridine	gr	-	1:1	liquid
4,4'-bis(diphenylhydroxymethyl)biphenyl	se	DCM, THF	1:1, 2:1	liquid

Table 15 Thymol cocrystallization trials.

Cof	Synth	Solvent	MR	Results
propofol	dm	-	1:1	liquid
carvacrol	se	ac	2:1	liquid + cof
2,2'-bipyridine	se	ac, MeOH	2:1	liquid + cof
B1	se	ac, MeOH	2:1	liquid + cof
PH1	se	ETAC	1:1	**cocr. TH-PH1α**
PH1	gr, se	MeOH, ac, THF	1:1	**cocr. TH-PH1β**
2-oxoglutaric acid	gr	-	2:1	cof + thymol
gallic acid	gr	-	2:1	powder
nicotinamide	gr	-	2:1	liquid
isonicotinic acid hydrazide	gr	-	1:1, 2:1	cof

Table 16 Eucalyptol cocrystallization trials.

Cof	Synth	Solvent	MR	Results
propofol	dm	-	1:1	liquid
5 amino isophthalic acid	se	MeOH	2:1	liquid + cof
3,5- piridin dicarboxilic acid	se	ac, MeOH	2:1	liquid + cof
4-aminophenol	se	ac	2:1	liquid + cof
SALOPH	se	ac	1:1	liquid + cof
1,4-diamino anthraquinone	se	ac	1:1	liquid + cof
guanidine	se	ac, H_2O	1:1, 2:1	liquid + cof
resorcinol	se	ETAC	1:1, 2:1	cof
F1	se	ETAC, ac	1:1	**cocrystal**
2,6- dihydroxy pyridine	gr	-	1:1	liquid
D1	se	DCM, THF	1:1, 2:1	cof

Table 17 Carvacrol cocrystallization trials.

Cof	Synth	Solvent	MR	Results
Propofol	dm	-	1:1	liquid
B1	se	ac	2:1	liquid + cof
2,2'-bipyridine	se	ac	2:1	liquid + cof
eugenol	dm	-	1:1	liquid
Cinnamaldehyde	dm	-	1:1	liquid
2-oxoglutaric acid	dm	-	2:1	liquid
isonicotinic acid hydrazide	dm	-	1:1, 1:2	liquid
PH1	dm, se	DCM, ac ,THF, $CHCl_3$, ETAC	1:1	**cocrystal**
guanine	dm	-	1:1	liquid
Urea	dm, se	MeOH, Acetonitrile	1:1	liquid

6.2 Crystal Data

Table 18 Crystal data and structure refinement for **carvacrol-PH1**.

Empirical formula	$(C_{10}O_1H_{14})_2(C_{12}N_2H_8)$
Formula weight	480.64
Temperature	293.15 K
Wavelength	0.71073 Å
Crystal system	Triclinic
Space group	P-1
Unit cell dimensions:	
a = 4.830(10)Å	α = 86.00(2)°
b = 9.850(10)Å	β = 89.41(4)°
c = 16.18(2)Å	γ = 77.52(3)°
Volume	750 (2) $Å^3$
Z	1
Density (calculated)	1.064 Mg/m^3
Absorption coefficient	0.066 mm^{-1}
F(000)	258
Reflections collected	6866
Independent reflections	3515 [R(int) = 0.0464]
Data / restraints / parameters	3515 / 0 / 167
Goodness-of-fit on F^2	1.047
Final R indices [I>2sigma(I)]	R1 = 0.0896, wR2 = 0.2412
R indices (all data)	R1 = 0.1173, wR2 = 0.2666

Table 19 Crystal data and structure refinement for **Nicotine-D1**.

Empirical formula	$(C_{10}N_2H_{14})(C_{32}O_2H_{26})$
Formula weight	604.76
Temperature	100(2) K
Wavelength	0.700 Å
Crystal system	Triclinic
Space group	P1
Unit cell dimensions:	
a = 8.225(2) Å	α = 86.84°
b = 8.962(2) Å	β = 87.91°
c = 11.967(2) Å	γ = 68.29°
Volume	818.2 $Å^3$
Z	1
Density (calculated)	1.227 Mg/m^3
Absorption coefficient	0.073 mm^{-1}
F(000)	322
Reflections collected	n/a
Independent reflections	8676 [R(int) = n/a]
Data / restraints / parameters	8676 / 3 / 418
Goodness-of-fit on F^2	1.141
Final R indices [I>2sigma(I)]	R1 = 0.0435, wR2 = 0.1167
R indices (all data)	R1 = 0.0436, wR2 = 0.1169

Table 20 Crystal data and structure refinement for **Nicotine-DITF**.

Empirical formula	$(C_{10}N_2H_{14})(C_6I_2F_4)$
Formula weight	564.9
Temperature	293(2) K
Wavelength	0.71073 Å
Crystal system	Monoclinic
Space group	$P2_1$
Unit cell dimensions:	
a = 10.65(2) Å	α = 90°
b = 12.12(2) Å	β = 91.35(3)°
c = 14.71(3) Å	γ = 90°
Volume	1898(6) $Å^3$
Z	4
Density (calculated)	1.974 Mg/m^3
F(000)	1064
Reflections collected	12857
Independent reflections	5436 [R(int) = 0.0985]
Data / restraints / parameters	5436 / 1 / 167
Goodness-of-fit on F^2	0.792
Final R indices [I>2sigma(I)]	R1 = 0.0700, wR2 = 0.1498
R indices (all data)	R1 = 0.1541, wR2 = 0.2023

Table 21 Crystal data and structure refinement for **Nicotine-DOB**.

Empirical formula	$(C_{10}N_2H_{14})(C_{12}I_4F_8)$
Formula weight	712.15
Temperature	100(2) K
Wavelength	0.700 Å
Crystal system	Monoclinic
Space group	$P2_1$
Unit cell dimensions:	
a = 8.7730(18) Å	α = 90°
b = 28.988(6) Å	β = 90.63(3)°
c = 18.092(4) Å	γ = 90°
Volume	4600.7(16) $Å^3$
Z	8
Density (calculated)	2.056 Mg/m^3
F(000)	2704
Reflections collected	13498
Independent reflections	8799 [R(int) = 0.1443]
Data / restraints / parameters	8799 / 1177 / 1085
Goodness-of-fit on F^2	1.035
Final R indices [I>2sigma(I)]	R1 = 0.1309, wR2 = 0.3276
R indices (all data)	R1 = 0.2070, wR2 = 0.3708

Table 22 Crystal data and structure refinement for **Propofol-B1**.

Empirical formula	$(C_{12}O_1H_{16})_2(C_{10}N_2H_8)$
Formula weight	512.71
Temperature	293.15 K
Wavelength	0.71073 Å
Crystal system	Monoclinic
Space group	P 21/c
Unit cell dimensions:	
a = 9.6090(14) Å	α = 90°
b = 9.8792(14) Å	β = 103.981(3)°
c = 17.184(2) Å	γ = 90°
Volume	1583.0(4) $Å^3$
Z	2
Density (calculated)	1.076 Mg/m^3
F(000)	556
Reflections collected	9070
Independent reflections	2010 [R(int) = 0.0283]
Data / restraints / parameters	2010 / 0 / 180
Goodness-of-fit on F^2	1.052
Final R indices [I>2sigma(I)]	R1 = 0.0890, wR2 = 0.2778
R indices (all data)	R1 = 0.1251, wR2 = 0.3245

Table 23 Crystal data and structure refinement for **Propofol-PH1**.

Empirical formula	$(C_{12}O_1H_{16})_2(C_{12}N_2H_8)$
Formula weight	536.72
Temperature	293(2) K
Wavelength	0.700 Å
Crystal system	Monoclinic
Space group	C 2/c
Unit cell dimensions:	
a = 18.189(4) Å	α = 90°
b = 7.4960(15) Å	β = 108.67(3)°
c = 23.606(5) Å	γ = 90°
Volume	3049.2(12) $Å^3$
Z	4
Density (calculated)	1.169 Mg/m^3
F(000)	1160
Reflections collected	13349
Independent reflections	7810 [R(int) = 0.0329]
Data / restraints / parameters	7810 / 1 / 371
Goodness-of-fit on F^2	0.979
Final R indices [I>2sigma(I)]	R1 = 0.0482, wR2 = 0.1429
R indices (all data)	R1 = 0.0649, wR2 = 0.1563

Table 24 Crystal data and structure refinement for **EU-F1**.

Empirical formula	$(C_{10}O_1H_{18})(C_7O_2H_8)$
Formula weight	279
Temperature	293(2) K
Wavelength	0.71073 Å
Crystal system	monoclinic
Space group	C c
Unit cell dimensions:	
a = 10.870 (2) Å	α = 90°
b = 11.132 (2) Å	β = 108.56°
c = 13.886 (2) Å	γ = 90°
Volume	1592.8 $Å^3$
Z	4
Density (calculated)	1.152 Mg/m^3
F(000)	600
Reflections collected	12361
Independent reflections	9426 [R(int) = 0.0258]
Data / restraints / parameters	9426 / 0 / 298
Goodness-of-fit on F^2	1.097
Final R indices [I>2sigma(I)]	R1 = 0.1172, wR2 = 0.3514
R indices (all data)	R1 = 0.1456, wR2 = 0.3935

Table 25 Crystal data and structure refinement for **TH-PH1α**.

Empirical formula	$(C_{10}O_1H_{14})(C_{12}N_2H_8)$
Formula weight	330.41
Temperature	293.15 K
Wavelength	0.71073 Å
Crystal system	Triclinic
Space group	P-1
Unit cell dimensions:	
a = 11.231(3) Å	α = 65.785(4)°
b = 12.699(3) Å	β = 72.696(4)°
c = 15.241(4) Å	γ = 76.010(4)°
Volume	1874.7(8) $Å^3$
Z	4
Density (calculated)	1.171 Mg/m^3
F(000)	704
Reflections collected	12537
Independent reflections	3715 [R(int) = 0.0632]
Data / restraints / parameters	3715 / 0 / 459
Goodness-of-fit on F^2	1.019
Final R indices [I>2sigma(I)]	R1 = 0.0572, wR2 = 0.1386
R indices (all data)	R1 = 0.1344, wR2 = 0.1748

Table 26 Crystal data and structure refinement for **TH-PH1β**.

Empirical formula	$(C_{10}O_1H_{14})(C_{12}N_2H_8)$
Formula weight	330.41
Temperature	296.15 K
Wavelength	0.71073 Å
Crystal system	Triclinic
Space group	P-1
Unit cell dimensions:	
a = 7.8166(14) Å	α = 90°
b = 8.9913(16) Å	β = 95.028(3)°
c = 26.744(5) Å	γ = 90°
Volume	1872.4(6) $Å^3$
Z	4
Density (calculated)	1.172 Mg/m^3
F(000)	704
Reflections collected	15573
Independent reflections	4644 [R(int) = 0.0536]
Data / restraints / parameters	4644 / 0 / 459
Goodness-of-fit on F^2	0.916
Final R indices [I>2sigma(I)]	R1 = 0.0508, wR2 = 0.1154
R indices (all data)	R1 = 0.1057, wR2 = 0.1436

7. REFERENCES

[1] A. I. Kitaigorodsky, *Mixed Crystals*; Springer-Verlag: Berlin, **1984**; p V.

[2] O. Almarsson, M. Zaworotko, *Chem. Commun.,* **2004**, 1889–1896.

[3] G. R. Desiraju, *CrystEngComm.,***2003**, 5, 466–467.

[4] A. D. Bond, *CrystEngComm.*, **2007**, 9, 833–834.

[5] D. S. Reddy, D. C. Craig, G. R. Desiraju, *J. Am. Chem. Soc.*, **1996**, 118, 4090-4093.

[6] G.R. Desiraju, T. Steiner, *The Weak Hydrogen Bond in StructuralChemistry and Biology*, Oxford Un. Press

Inc., United States, **1999**, p.507.

[7] P. Metrangolo, G. Resnati, Chem. Eur. J., **2001**, 7, 2511-2519.

[8] K. Rissanen, *CrystEngComm*, **2008**, 10, 1107-1113.

[9] C. A. Hunter, J. K. M. Sanders, *J. Am. Chem. Soc.*,**1990**,112 (14): 5525–5534.

[10]M. C. Etter, *Acc. Chem. Res.,* **1990**, Vol. 23, No. 4.

[11]T.R. Shattock, K.K. Arora, P. Vishweshwar, M.J. Zaworotko, *Cryst. Growth Des.*, **2008**, 8, 4533-4545.

[12]J.A. Bis, P. Vishweshwar, D. Weyna, M.J. Zaworotko, *Mol. Pharmaceutics*, **2007**, 4, 401- 416.

[13] P. Politzer, J. S. Murray, M. C. Concha, *J. Mol. Model*., **2008**, 14, 659-665.

[14] R. F. Stewart, *Chem. Phys. Lett*., **1979**, 65, 335-342.

[15] G. Naray-Szabo, G. G. Ferenczy, *Chem. Rev.,* **1995**, 95, 829-847.

[16] T. Brinck, J. S. Murray, P. Politzer, *Int. J. Quantum Chem.*, **1992**, 44, 57-64.

[17] A. C. Legon, *Angew. Chem.,***1999**, 38, 2686-2714.

[18] Z. Shields, J. S. Murray, P. Politzer, *Int. J. Quantum Chem.,* DOI: 10.1002/qua.22787.

[19] E. Corradi, S. V. Meille, M. T. Messina, P. Metrangolo, G. Resnati*, Angew. Chem.*, **2000**, 39, 1782-86.

[20]K.-S. Huang, D. Britton, M. C. Etter, S. R. Byrn, *J. Mater. Chem.*, **1997**, 7, 713-720.

[21]B. R. Bhogala, S. Basavoju, A. Nangia, *CrystEngComm*, **2005**, 7, 551-562.

[22]S. L. Childs, G. P. Stahly, A. Park, *Molecular Pharmaceutics*, **2007**, 4, 3, 323-338.

[23]P. H. Stahl, M. Nakano, *Handbook of Pharmaceutical Salts: Properties, Selection and Use*. Wiley-VCH: New York, **2002**.

[24]S. M. Berge, L. D. Bighley, D. C. Monkhouse, *J. Pharma. Sci.*, **1977**, 66, 1-19.

[25] Ö. Almarsson, M. J. Zaworotko, *Chem. Commun.*, **2004**, 1889-1896.

[26]G. Springuel, T. Leyssens,*Cryst. Growth Des*., **2012**, 12, 3374.

[27] M. T. Kirchner, D. Das, R. Boese, *Crystal Growth & Des.*, **2008**, vol.8, no.3, 763-765.

[28] M. T. Kirchner, D. Blaser, R. Boese, *Chem. Eur. J.*, **2010**, 16, 2131 – 2146.

[29] R. Boese, D. Blaser, G. Jansen, *J. Am. Chem. Soc.*, **2009**,131, 2104-2106.

[30] M. T. Kirchner, R. Boese, W. E. Billups, L. R. Norman, *J. Am. Chem. Soc.*, **2004**, 126, 9407-9412.

[31] C. B. Aakeröy, T. K. Wijethunga, J. Benton, J. Desper, *Chem. Commun.*, **2015**, 51, 2425.

[32]H. Furukawa, K. E. Cordova, M. O'Keeffe, O. M. Yaghi, *Science*, **2013**, 341.

[33] M. Zhang, M. Bosch, T. Gentle III, H.-C. Zhou, *CrystEngComm*, **2014**, 16, 4069.

[34] T. A. Makal, J.-R. Li, W. Lu, H.-C. Zhou, *Chem. Soc. Rev.*, **2012**, 41, 7761-7779.

[35] M. P. Suh, H. J. Park, T. K. Prasad, D.-W. Lim, *Chem. Rev.*, **2011**, 112, 782-835.

[36] E. D. Bloch, W. L. Queen, R. Krishna, J. M. Zadrozny, C. M. Brown, J. R. Long, *Science*, **2012**, 335, 1606-1610.

[37] T. M. McDonald, W. R. Lee, J. A. Mason, B. M. Wiers, C. S. Hong, J. R. Long, *J. Am. Chem. Soc.*, **2012**, 134, 7056-7065.

[38] K. Sumida, D. L. Rogow, J. A. Mason, T. M. McDonald, E. D. Bloch, Z. R. Herm, T.-H. Bae, J. R. Long, *Chem. Rev.*, **2011**, 112, 724-781.

[39] L. Ma, C. Abney, W. Lin, *Chem. Soc. Rev.*, **2009**, 38, 1248-1256.

[40] M. Yoon, R. Srirambalaji, K. Kim, *Chem. Rev.*, **2011**, 112, 1196-1231.

[41] M. D. Allendorf, C. A. Bauer, R. K. Bhakta, R. J. T. Houk, *Chem. Soc. Rev.*, **2009**, 38, 1330-1352.

[42] M. Eddaodui, J. Kim, N. Rosi, D. Vodak, J. Wachter, M. O'Keeffe, O. M. Yaghi, *Science*, **2002**, 295, 469-472.

[43] O. M. Yaghi, M. O'Keeffe, N. W. Ockwig, H. K. Chae, M. Eddaoudi, J. Kim, *Nature*, **2003**, 423, 705-714.

[44] D. Zhao, D. J. Timmons, D. Yuan, H.-C. Zhou, *Acc. Chem. Res.*, **2010**, 44, 123-133.

[45] F. A. Almeida Paz, J. Klinowski, S. M. F. Vilela, J. P. C. Tome, J. A. S. Cavaleiro, J. Rocha, *Chem. Soc. Rev.*, **2012**, 41, 1088-1110.

[46]J. An, S. J. Geib and N. L. Rosi, *J. Am. Chem. Soc.*, **2009**, 131, 8376–8377.

[47]P. Horcajada, T. Chalati, C. Serre, B. Gillet, C. Sebrie, T. Baati, F. Eubank, D. Heurtaux, P. Clayette, C. Kreuz, J.-S. Chang, Y. K. Hwang, V. Marsaud, P.-N. Bories, L. Cynober, S. Gil, G. Férey, P. Couvreur, R. Gref, *Nat. Mater.,* **2010**, 9, 172.

[48]D. Cunha,M. B.Yahia,S. Hall,S. R. Miller,H.Chevreau,E. Elkaïm,G.Maurin,P.Horcajada,C.Serre,*Chem. Mater.*, **2013**, 25, 2767-2776.

[49]Y. Inokuma, S. Yoshioka, J. Ariyoshi, T. Arai, Y. Hitor, K. Takada, S. Matsunaga, K. Rissanen, M. Fujita, *Nature*, **2013**, 495, 461-466.

[50]S. L. James, C. J. Adams, C. Bolm, D. Braga, P. Collier, T. Friscíc, F. Grepioni, K. D. M. Harris, G. Hyett, W. Jones, A. Krebs, J. Mack, L. Maini, a. G. Orpen, I. P. Parkin, W. C. Shearouse, J. W. Steed and D. C. Waddell, *Chem. Soc.Rev.*, **2012**, 41, 413.

[51]G.-W. Wang, *Chem. Soc.Rev.*, **2013**, 42, 7668.

[52]E. Boldyreva, *Chem. Soc.Rev.*, **2013**, 42, 7719-7738.

[53] D. Balarew, *Z. Anorg. Allg. Chem*., **1924**, 136, 216–220.

[54] V. V. Boldyrev, *Russ. Chem. Rev.*, **2006**, 75(3), 177–189.

[55]E. Avvakumov, M. Senna and N. Kosova, *Soft Mechanochemical Synthesis: A Basis for New Chemical Technologies, Kluwer Academic*, Boston, **2001**.

[56]D. Braga, S. L. Giafredda, F. Grepioni, M. R. Chierotti, R. Gobetto, G. Palladino and M. Polito, *CrystEngComm*, **2007**, 9, 879–881

[57] D. T. Haynie DT. *Biological Thermodynamics*. Cambridge, UK: Cambridge University Press, **2008**.

[58] P. J. Haines, M. Reading, F. W. Wilburn. *Differential thermal analysis and differential scanning calorimetry.* In M. E. Brown, editor. (ed): *Handbook of Thermal Analysis and Calorimetry*, vol. 1 The Netherlands: Elsevier Science BV; **1998**; 279–361.

[59] R. L. Danley, *Thermochim. Acta*, **2002**; 395:201–208.

[60] Li et al. **2008**, Chiarella et al. 2007, Marchand et al. **2004**, Coquerel 2014.

[61] G. Coquerel, *Chem. Soc. Rev*., **2014**, 43, 2286

[62] A. Ainouz, J-R. Authelin, P. Billot, H. Lieberman, *Intern. Journ. Of Pharm*., **2009**, 374, 82-89.

[63] R. Thakuria, A. Delori, W. Jones, M. P. Lipert, L. Roy, N. Rodriguez-Hornedo, *International Journal of Pharmaceutics*, **2013**, 453, 101-125.

[64] A. Jayasankar, L. S. Reddy, S. J. Bethune, N. Rodriguez-Hornedo, *Crystal Growth & Des.*, **2009**, 9 (2), 889-897.

[65] D. J. Good, N. Rodriguez-Hornedo, *Crystal Growth & Des.*, **2009**, 9 (5), 2252-2264.

[66]T. Y. Euliano ; J. S. Gravenstein (2004), *"A brief pharmacology related to anesthesia*". Essential anesthesia: from science to practice. Cambridge, UK: Cambridge University Press., **2009**, p. 173. ISBN 0-521-53600-6.

[67] "*WHO Model List of Essential Medicines*", World Health Organization, **2013**. p. 6.

[68]T. A. Perfetti, A. Rodgman,BeiträgezurTabakforschung International, **2011**, Vol. 24, No.5.

[69] I. Ujváry*Nicotinoid Insecticides and the Nicotinic Acetylcholine Receptor*, Tokyo: Springer-Verlag. **1999**,pp. 29–69.

[70]H. Wan, A. G. Holmen, Y. Wang, W. Lindberg, M. Englund, M. B. Nagard, R. A. Thompson, *Rapid Commun. Mass Spectrom.*, **2003**, 17, 2639–2648.

[71] R. B. Barlow, J. A. K. Howard, O. Johnson, *ActaCrystallogr.,Sect.C*, **1986**, 42, 853.
H. S. Kim, G. A. Jeffrey, *ActaCrstallogr., Sect. B*, **1971**, 27, 1123.

[72] H. S. Kim, G. A. Jeffrey, *ActaCrstallogr., Sect. B*, **1971**, 27, 1123.

[73] G. Smith, U. D. Wermuth, *ActaCrystallogr.,Sect.E*, **2014**, 70, 430.

[74]K. Fukawa, S. Harada, N. Kasai, M. Toda, K. Mori, F. Toda, *Bull.Chem.Soc.Jpn*. **1989**, 62, 2714.

[75]M.Massaro, E. Scoditti, M. A. Carluccio, R. De Caterina, *Cardiovasc. Ther.***2010**, 28, 13−19.
M. Pandey, R. K. Verma, S. A. Saraf, *Asian, J. Pharm. Clin. Res.,***2010**, 3, 11−15.

[76] W. X. Du, C.E. Olsen, R J. Avena-Bustillos, T.H. McHugh, C. E. Levin, M. Friedman, *J. Agric. Food Chem.*, **2008,** 56 (9): 3082–3088.

[77] A. Ultee, E. J. Smid, *Int. J. Food Microbiol*., **2001**, 64 (3), 378.

[78] S. D. Cox, J. L. Markham, *J. Appl. Microbiol.*, **2007**, 103 (4), 930-936.

[79] K. Palaniappan, R. A. Holley, *International J. of Food Microbiology*, **2010**, 140 (2-3), 164-168.

[80] G. Zarrini, Z. Bahari-Delgosha, K. Mollazadeh-Moghaddam, A. R. Shahverdi, *Pharmaceutical biology,* **2010**, 48 (6), 633-636.

[81] E. Zhou et al., *Fitoterapia*., **2014**, 96, 131-137.

[82] J. A. Klocke, M. V. Darlington, M. F. Balandrin, *Journal of Chem. Ecology*, **1987**, 13(12), 2131.
V. Sfara, E. N. Erba, R. A. Alzogaray, *Journal of Medicinal Entomology*, **2009**, 46(3), 511-515.

[83]F. Guo, W. S. Guo, F. Toda, *CrystEngComm*, **2003**,5, 45-47.

[84]D. Braga; F. Grepioni; L. Maini; P. P. Mazzeo; K. Rubini, *Thermochimica Acta*, **2010**, 507-508, 1-8.

[85] US4064127, 20/12/**1977**, Eli Lilly And Company, Trifluoromethyldibenzo[a,c]phenazines as immune regulants.

[86] WO1998027969 A2, 24/12/**1997**, J. Brien, G.Marks, K. Nakatsu, D. Vukomanovic, D. Zoutman, Antimicrobial phenazine compounds.

[87] WO2008089283 A1, 16/1/**2008**, J. B. Tunac, Phenazine compounds and use thereof in autoimmune and inflammatory diseases.

[88]S. Chakraborty, L. Rajput, G. R. Desiraju, *Cryst. Growth Des.*, **2014**, 14 (5), pp 2571-2577.
M. Gdaniec and T. Polonski, ActaCryst. **2007**, E 63, 707-709.
V. R. Thalladi, T. Smolka, R. Boese and R. Sustmann, CrystEngComm, **2000**, 2, 96-101.
V. R. Vangala, P. S. Chow, R. B. H. Tan, *Cryst. Growth Des.*, **2012**, 12 (12), pp 5925-5938.

[89]T. W. Lee, J. P. K. Lau, L. Szeto, *Acta Cryst.***2003**, E 59, 942-944.
S. B. Liu, C. Xu, T. Duan, Q. Chen, Q. F. Zhang, *ActaCryst.***2011**. E 67, 2033.
S. Tothadi, *CrystEngComm*, **2014**,16, 7587-7597.

[90]P. Metrangolo, F. Meyer, T. Pilati, G. Resnati, G. Terraneo, *Angew. Chem., Int. Ed.***2008**, 47, 6114–27.
C. B. Aakeroy, T. K. Wijethunga, M. A. Haj, J. Desper, C. Moore, *Cryst.Eng.Comm.,***2014**, 16, 7218.

[91]K. Fukawa, S. Harada, N. Kasai, M. Toda, K. Mori, F. Toda, *Bull.Chem.Soc.Jpn*. **1989**, 62, 2714.
L. Johnson, L. Nassimbeni, E. Weber, K. Skobridis, *J. Chem. Soc.*, **1992**, 2131-2136.
L. R. Nassimbeni, H. Su, E. Weber, K. Skobridis, *Crystal Growth & Des.*, **2004**, 4(1), 85-88.
A. Jacobs, L. R. Nassimbeni, N. Silwana, N. B. Báthoria, E. Weberb, *Cryst.Eng.Comm.*, **2011**,13, 7014-18.

[92] A. Mukherjee, P. Grobelny, T. S. Thakur, G. R. Desiraju, *Cryst. Growth Des.*, **2011**, 11, 2637–2653.

[93] C. B. Aakeroy, T. K. Wijethunga, M. A. Haj, J. Desper, C. Moore, *Cryst.Eng.Comm.,***2014**, 16, 7218.

[94] Shelz97, *Program for structure refinement*, G. Sheldrick, University of Goettingen, Germany, 1997.

[95] O. V. Dolomanov, L. J. Bourhis, R. J. Gildea, J. A. K. Howard and H. Puschmann *J. Appl. Cryst.,* **2009,** 42, 339-341.

[96] K.-S. Lin, A. K. Adhikari, C.-N. Ku, C.-L. Chiang, H. Kuo, Int. *J. of Hydrogen En*., 37 (18), **2012**, 13865-13871.

[97] S. Ma, D. Sun, M. Ambrogio, J. A. Fillinger, S. Parkin, and H.-C. Zhou, *J. Am. Chem. Soc.,* 129(7), **2007**, 1859

[98] G. Coquerel, *Chem. Soc. Rev.*, **2014**, 43, 2286-2300.

[99] M. P. Johansson, J. Olsen, *J. Chem. Theory Comput.*, **2008**, 4(9), 1460.

[100] K. Fukawa, S. Harada, N. Kasai, M. Toda, K. Mori, F. Toda, *Bull.Chem.Soc.Jpn*. **1989**, 62, 2714.

[101] S. Aitipamula, P. S. Chow, R. B. H. Tan, *CrystEngComm*, **2014**, 16, 3451-3465.

[102] D. C. Sherrill, *et al, J. Phys. Chem. A.*, **2004**, 108, 10200.

[103] T. G. G. Battye, L. Kontogiannis, O. Johnson, H. R. Powell, A. G. W. Leslie, *Acta Crystallogr D Biol Crystallogr.* **2011**; 67(Pt 4): 271–281.

[104] S. Jana, P. A. G. Cormack, A. R. Kennedy, D. C. Sherrington, *J. of Mat. Chem.*, **2009**, 19, 3427-3442.

[105] I. J. Bruno, J. C. Cole, P. R. Edgington, M. Kessler, C. F. Macrae, P. McCabe, J. Pearson and R. Taylor, *Acta Cryst.,* B58, 389-397, **2002.**